



UNIVERSITY OF ÉVORA

SCHOOL OF SCIENCES AND TECHNOLOGY

DEPARTMENT OF PHYSICS

**Design and Optimization of Building Integration
PV/T Systems (BIPV/T)**

Ricardo Jorge da Silva Pereira

Supervision: Laura Aelenei, Ph.D.

António Joyce, Ph.D.

Masters in Solar Energy Engineering

Dissertation

Évora, 2015



UNIVERSITY OF ÉVORA

SCHOOL OF SCIENCES AND TECHNOLOGY

DEPARTMENT OF PHYSICS

**Design and Optimization of Building Integration
PV/T Systems (BIPV/T)**

Ricardo Jorge da Silva Pereira

Supervision: Laura Aelenei, Ph.D.

António Joyce, Ph.D.

Masters in Solar Energy Engineering

Dissertation

Évora, 2015

“The Stone Age came to an end, not because we had a lack of stones”

Sheikh Yamani

RESUMO

Design e Optimizaç o de um Sistema PV/T Integrado em Edif cio (BIPV/T)

Neste trabalho   analisado, por via num rica e experimental, o comportamento t rmico e el ctrico de um sistema fotovoltaico/t rmico integrado em edif cio, recorrendo a material de mudan a de fase para regulariza o da diferen a de temperatura entre interior e exterior e para a estabiliza o da temperatura do m dulo fotovoltaico.

Foi realizado uma revis o da literatura sobre o tema. Um modelo de c lculo dos fen menos de transfer ncia de calor e massa foi desenvolvido, assim como da produ o de energia el ctrica, e implementado em software de c lculo Matlab/Simulink[®].

Paralelamente foram conduzidos ensaios experimentais a fim de analisar o comportamento t rmico do sistema e respectiva valida o do modelo num rico. De modo a melhorar a efici ncia total do sistema, foi aplicado um processo de optimiza o com o m todo dos algoritmos gen ticos.

Do estudo, conclui-se que o sistema pode alcan ar uma efici ncia m xima total de 64% na configura o de inverno e de 32% na configura o de ver o.

Palavras Chave: Edif cio integrado fotovoltaico/t rmico; Armazenamento de energia; Material mudan a de fase; Modelo t rmico; Algoritmo Gen tico.

ABSTRACT

This work presents a numerical and experimental analysis of the thermal and electrical performance of a building integrated photovoltaic/thermal system (BIPV/T), with the use of phase change material for stabilize the temperature difference between indoors and outdoors and a rapid stabilization of the PV modules' temperature.

A literature review was conducted on the topic. A calculation model was developed of the heat and mass transfer phenomena, as well as a model of a photovoltaic module, which were implemented in Matlab/Simulink®.

Experimental tests were performed to analyze the thermal performance of the system and the validation of the numerical model. To improve overall system efficiency, an optimization process with the method of genetic algorithms was applied.

From the study, it is concluded that the system can achieve a maximum total efficiency of 64% with winter configuration and 32% with summer configuration.

Keywords: building integrated photovoltaic/thermal; energy storage; phase-change material; thermal modelling; genetic algorithm.

ACKNOWLEDGEMENTS

I would like to express my sincere thanks to the various people and entities whose contributions have been of benefit to this work.

I would first like to thank Laura Aelenei, Ph.D., and Professor António Joyce, the scientific mentors of this work, for their permanent monitoring, availability, and critical and constructive spirit.

Thanks, too, to LNEG for giving me the opportunity to take part in this project.

And to my sister Marta Pereira for the scientific support she provided.

Thanks to Luisa for all her support.

Thanks to everyone who contributed in some way to this work. They are: Alvaro Ramalho, Ana Rute, António Rocha e Silva, Bruno Durão, Carlos Rodrigues, and José Ventura. I also would like to thank to Jean Burrows for the English revision of the manuscript.

I am grateful to FogãoSol for constructing the prototype.

I must also thank the Foundation for Science and Technology (FCT) for financial support in the form of research fellowship, under the FRAME project financed by FEDER funds through the Operational Program for Competitiveness Factors - COMPETE and national Funds through FCT - Foundation for Science and Technology under the project FCOMP-01-0124-FEDER-019471 (Ref PTDC/AURAQI-AQI/117782/2010).

TABLE OF CONTENTS

RESUMO.....	I
ABSTRACT.....	III
ACKNOWLEDGEMENTS.....	V
TABLE OF CONTENTS.....	VII
LIST OF FIGURES.....	XI
LIST OF TABLES.....	XV
NOMENCLATURE	XVII
CHAPTER 1. INTRODUCTION.....	1
1.1. INTRODUCTION.....	1
1.2. OBJECTIVES.....	3
1.3. OUTLINE	3
CHAPTER 2. BUILDING INTEGRATED PV/T SYSTEMS (BIPV/T) REVIEW	5
2.1. INTRODUCTION.....	5
2.2. INTEGRATION / APPLICATION.....	6
2.3. APPROACH	11
2.4. EFFICIENCY	13
CHAPTER 3. BASIC FUNDAMENTALS OF HEAT AND MASS TRANSFER.....	15
3.1. INTRODUCTION.....	15
3.2. HEAT TRANSFER.....	15
3.2.1. Conduction Heat Transfer.....	16
3.2.2. Convection Heat Transfer	18
3.2.3. Radiation Heat Transfer.....	21
3.3. THERMAL RESISTANCE.....	24
3.4. ENTHALPY TRANSPORT.....	25
3.5. THERMAL MASS	25
3.6. PHASE CHANGE ENERGY STORAGE.....	26

CHAPTER 4. HEAT TRANSFER NUMERICAL APPROACH.....	29
4.1. INTRODUCTION.....	29
4.1.1. Air velocity within the air cavity.....	30
4.1.2. PCM model approach.....	30
4.2. PROBLEM FORMULATION.....	32
4.2.1. Heat Transfer Coefficients.....	32
4.2.2. Thermal Model.....	36
4.2.3. Electrical Model for PV Module.....	38
4.3. SYSTEM PERFORMANCE.....	40
4.4. IMPLEMENTATION OF THE NUMERICAL MODEL IN MATLAB®.....	41
4.4.1. Heat Transfer in Simscape®.....	42
4.4.2. Constructing the Model.....	45
CHAPTER 5. EXPERIMENTAL EVALUATION.....	47
5.1. INTRODUCTION.....	47
5.2. DESIGN PROJECT.....	48
5.3. SYSTEM DESCRIPTION.....	49
5.4. EXPERIMENTAL SET-UP AND INSTRUMENTATION.....	51
5.4.1. Data Acquisition Logger.....	53
5.4.2. Temperature Sensors.....	54
5.4.3. Fluxmeter Sensors.....	56
5.4.4. Hotwire Anemometer.....	58
5.4.5. Thermal Images.....	58
5.5. MEASUREMENT CAMPAIGN AND EXPERIMENTAL RESULTS.....	59
5.5.1. Winter Campaign.....	59
5.5.2. Summer Campaign.....	65
5.5.3. Campaigns Comparison.....	70
5.6. VALIDATION OF THE NUMERICAL MODEL.....	72
5.6.1. Introduction.....	72
5.6.2. Validation.....	72
5.6.3. Air Velocity Within the Cavity.....	75
5.6.4. System Performance.....	75
CHAPTER 6. SYSTEM OPTIMIZATION.....	79
6.1. INTRODUCTION.....	79
6.2. OPTIMIZATION METHOD (GA).....	80
6.2.1. Elements of the Genetic Algorithm.....	81

6.3. APPLICATION OF THE METHOD.....	82
6.3.1. Software Application (Matlab)	85
6.4. OPTIMIZATION SCENARIOS	88
6.5. RESULTS.....	90
6.5.1. Winter	90
6.5.2. Summer	94
6.5.3. Overall	98
CHAPTER 7. CONCLUSION.....	101
7.1. DISCUSSION.....	101
7.2. FUTURE WORK.....	103
REFERENCES.....	105
APPENDICES.....	A-1
APPENDIX A.....	A-1
APPENDIX B	A-1
APPENDIX C.....	A-2
APPENDIX D.....	A-3

LIST OF FIGURES

Fig. 2.1. Review specific subjects.....	6
Fig. 2.2. Example of a scheme of a water based BIPV/T applied on a facade [17]	7
Fig. 2.3. Schematic of a BIPV/T applied on a façade – SOLAR XXI Building [30]	8
Fig. 2.4. Concept schematic for a BIPV/T system with transpired collector [31].	9
Fig. 2.5. Example of a scheme of an air-based BIPV/T with PCM, applied on a façade [37]	9
Fig. 2.6. Schematic of a BIPV/T applied on a roof [6]	10
Fig. 2.7. a) Schematic of a water based BIPV/T applied on a roof, b) Schematic of a water based PV/T [49]	11
Fig. 2.8. Example of a thermal network of a BIPV/T roof system [6].	12
Fig. 2.9. Example of a CFD simulation flow pattern (left). Example of a CFD simulation PV temperature (right) [28].	13
Fig. 2.10. Graphical summary of the efficiency obtained by the authors.....	14
Fig. 3.1. Heat transfer through a ventilated air cavity wall system [53]	16
Fig. 3.2. One-dimensional heat transfer by conduction [55]	17
Fig. 3.3. Boundary layer development in convection heat transfer [55]	18
Fig. 3.4. Radiation exchange: a) at a surface and (b) between a surface and large surroundings [55]	22
Fig. 3.5. Stages of a phase transition of a PCM.....	27
Fig. 4.1. System configuration.....	29
Fig. 4.2. (a) Phase transition curve for a PCM gypsum board from DSC test [63]. (b) Approximation of DSC curve [63]	31
Fig. 4.3. Model studied – Thermal network [37]	32
Fig. 4.4. PV equivalent circuit [73].....	39
Fig. 4.5. winter (left) and summer (right) configurations.....	40
Fig. 4.6. Simscape® Conductive Heat Transfer block.....	43
Fig. 4.7. Simscape® Convective Heat Transfer block	43
Fig. 4.8. Simscape® Radiative Heat Transfer block.....	43
Fig. 4.9. Custom Simscape® Convection Heat Transfer block	44
Fig. 4.10. Simscape® Thermal Mass block.....	44
Fig. 4.11. Simscape® Solar Cell block	45
Fig. 4.12. Simscape PV thermal layer block (a), PV electrical model block (b), First window interface (c).....	45

Fig. 5.13. PV module (a), Frame (b), PCM layer (c), Assembly (isometric) (d).....	48
Fig. 5.14. Assembly (back) (a), Section of semi-exploded view (b)	49
Fig. 5.1. Solar XXI building (top), Prototype installed on the Solar XXI main facade (bottom) [37].....	50
Fig. 5.2. Crosssection of BIPV-PC [35].....	50
Fig. 5.3. Cross section set-up and sensor positions [37]	52
Fig. 5.4. Sensors installed on inner PV layer (a), Sensors installed on inner PCM layer (b)	53
Fig. 5.5. Detail of the support structure for the three air temperature sensors	53
Fig. 5.6. Data Logger (a), Data Acquisition apparatus (b), Data logger acquisition software (c).....	54
Fig. 5.7. PT 100 sensor (a). PT 100 Self-adhesive sensor (b)	55
Fig. 5.8. PT 100 sensor (a), PT 100 Self-adhesive sensor (b)	55
Fig. 5.9. Hukseflux HFP01 fluxmeter (a). Hukseflux HFP01 fluxmeter installed at PV interior layer (b)	56
Fig. 5.10. Hukseflux SR11 pyranometer (a). SR11 pyranometer installed at PV exterior layer (b).....	57
Fig. 5.11. Hotwire anemometer logger (Testo 425) (a). Taking measurement with the hotwire anemometer (b).....	58
Fig. 5.12. Testo Fluke Ti25 thermal camera	59
Fig. 5.13. Exterior, interior temperature and solar radiation measurements February 2013 [35]...60	
Fig. 5.14. Temperature and irradiance values, 22 February 2013 [35].	60
Fig. 5.15. Cross section temperatures at different times, 22 February 2013 [35].....	61
Fig. 5.16. Heat flux through PCM surfaces 22 February 2013.....	62
Fig. 5.17. Temperature and irradiation values, 25 February 2013 [35]	63
Fig. 5.18. Cross section temperatures at different times, 25 February 2013 [35].....	64
Fig. 5.19. Heat flux through surfaces, 25 February 2013.....	64
Fig. 5.20. Exterior, interior temperature and solar radiation measurements, June and July 2013.....	65
Fig. 5.21. Temperature and irradiation values, 5 July 2013	66
Fig. 5.22. Cross section temperatures at different times, 5 July 2013	67
Fig. 5.23. Heat flux through surfaces 5 July 2013	67
Fig. 5.24. Temperature and irradiation values, 19 June 2013.....	68
Fig. 5.25. Cross section temperatures at different times, 19 June 2013	69
Fig. 5.26. Heat flux through surfaces 19 June 2013	69
Fig. 5.27. Four days' parameters: Radiation (top left), Exterior temperature (top right); Four days' data: Heat flux through PCM (bottom left), Air flow system (bottom right)	70
Fig. 5.28. Stratification within the air cavity	71

Fig. 5.29. 25 February (left); 5 July (right) [37].	72
Fig. 5.30. Simulated versus experimental values of heat flux through layers for 25 February 2013.	73
Fig. 5.31. Simulated versus experimental values of heat flux through layers for 5 July 2013	74
Fig. 5.32. Thermal images and photos at 12:00 on 5 July 2013	74
Fig. 5.33. Air velocity within cavity	75
Fig. 5.34. Thermal BIPV-PCM system efficiency. 25 February 2013 (left), 5 July 2013 (right)	76
Fig. 5.35. Electrical BIPV-PCM system efficiency	77
Fig. 6.1. Flowchart of a simple routine optimization through genetic algorithms [79]	83
Fig. 6.2. Functional diagram of the optimization toolbox	86
Fig. 6.3. Winter configuration for the optimization process	88
Fig. 6.4. Summer configuration for the optimization process	89
Fig. 6.5. Climatic conditions for the optimization process	90
Fig. 6.6. Maximum (Best) and mean Thermal efficiency for several generations of the winter optimization process.	91
Fig. 6.7. Electrical efficiency from the winter optimization process	92
Fig. 6.8. Optimization variables: winter optimization process results	93
Fig. 6.9. System temperatures obtained from the optimization process	94
Fig. 6.10. Maximum (Best) and mean Thermal efficiency for several generations of the summer optimization process.	95
Fig. 6.11. Electrical efficiency of the summer optimization process	96
Fig. 6.12. Optimization variables: summer optimization process results	96
Fig. 6.13. System temperatures obtained from the optimization process	97
Fig. 6.14. Total efficiency analysis	98
Fig. 6.15. Variables analysis	99

LIST OF TABLES

Table 3.1. Nusselt number relations depending on the nature of the flow	21
Table 5.1. Materials properties.	51
Table 5.2. Sensors identification and positions	52
Table 5.3. Sensitivity calibration constant	57
Table 5.4. Cross section temperatures at different times, 22 February 2013	62
Table 5.5. Cross section temperatures at different times, 25 February 2013	63
Table 5.6. Cross section temperatures at different hours, 5 June 2013	66
Table 5.7. Cross section temperatures at different times, 19 June 2013	68
Table 5.8. Dimensionless vertical maximum temperatures	71
Table 6.1. Differences between the GA and classical optimization methods.....	81
Table 6.2. Optimization parameters	84
Table 6.3. Variables range.....	84
Table 6.4. Thermal efficiency from winter optimization process	90
Table 6.5. Electrical efficiency of the winter optimization process	91
Table 6.6. Optimization variables: winter optimization process results	93
Table 6.7. Thermal efficiency of the summer optimization process	94
Table 6.8. Electrical efficiency of the summer optimization process	95
Table 6.9. Optimization variables: results from summer optimization process results.....	97

NOMENCLATURE

Notation	Description	Unit
Latin		
A	Area	$[m^2]$
A_{cr}	Cross-Sectional Area	$[m^2]$
A_g	Total gap cross-sectional area	$[m^2]$
A_v	Total vent area	$[m^2]$
C_1	PV thermal mass	$[J/K]$
C_2	Air thermal mass	$[J/K]$
C_3	PCM thermal mass	$[J/K]$
C_p	Specific heat	$[J/(kg.K)]$
$C_{p_{air}}$	Specific heat of the air	$[J/(kg.K)]$
$C_{p_{pv}}$	Specific heat of the PV	$[J/(kg.K)]$
C_{p_w}	Specific heat of the isolated brick or PCM	$[J/(kg.K)]$
D_1	Diode	-
D_h	Hydraulic diameter	$[m]$
E	Heat flux emitted by a real surface	$[W/m^2]$
E_b	Maximum flux of radiation that can be emitted by a body	$[W/m^2]$
$F_{R_{pv-pcm}}$	View factor between the PV and PCM panes	[]
G	Total incident solar irradiance on the plane of the collector per unit area	$[W/m^2]$
g	Gravitational acceleration	$[m/s^2]$
Gr	Grashof number	[]
h_c	Convective heat transfer coefficient	$[W/(m^2.K)]$
h_e	Exterior convective heat transfer coefficient per unit area	$[W/(m^2.K)]$
h_i	Interior convective heat transfer coefficient per unit area	$[W/(m^2.K)]$
h_{pvac}	Convective heat transfer coefficient for the PV/Air Cavity surface per unit area	$[W/(m^2.K)]$

h_r	Radiative heat transfer coefficient between PV and PCM surfaces	[W/(m ² .K)]
h_{wac}	Convective heat transfer coefficient for the Air Cavity/Wall surface per unit area	[W/(m ² .K)]
I	Output current	[A]
I_0	Diode reverse bias saturation current	[A]
I_d	Current at diode	[A]
I_p	Leakage current	[A]
I_s	Photo generated electric current	[A]
l	Characteristic length	[m]
L	Layer thickness	[m]
L_p	Latent heat for the temperature range	[J/kg]
L_t	Latent Heat	[J/kg]
M	Thermal mass	[kg]
m	Diode ideality factor	[]
\dot{m}	Air mass flow rate	[kg/s]
M_{air}	Air cavity thermal mass	[kg]
M_{pv}	PV thermal mass	[kg]
M_w	Wall thermal mass (Isolated Brick or PCM)	[kg]
Nu	Nusselt number	[]
P	Perimeter	[m]
Pr	Prandtl number	[]
q	Electron charge	[C]
Q	Thermal energy	[J]
q''_c	Heat flux by convection	[W/m ²]
q''_{rad}	Heat flux by radiation	[W/m ²]
q''_x	Heat flux by conduction	[W/m ²]
q_c	Heat rate by convection	[W]
q_e	Air cavity resultant heat flow	[W]
q_{int}	Heat rate through the wall	[W]
q_l	Latent heat flux when phase change occurs	[W]
q_{rad}	Heat rate by radiation	[W/m ²]
Q_s	Storage capacity	[J]
q_V	Air flow coming from air cavity to the interior room	[W]

q_x	Heat rate by conduction	[W]
R	Heating and cooling rate	[°/s]
Ra	Rayleigh number	[]
Re	Reynolds number	[]
R_p	Equivalent shunt resistance	[Ω]
R_{pv}	Thermal Resistance of the PV pane	[K/W]
R_s	Series resistance	[Ω]
$R_{t,cond}$	Thermal resistance for conduction	[K/W]
$R_{t,conv}$	Thermal resistance for convection	[K/W]
$R_{t,rad}$	Thermal resistance for radiation	[K/W]
R_w	Thermal Resistance of the Wall pane (Isolated Brick or PCM)	[K/W]
T	Temperature	[°C] or [K]
T_1	Temperature at which the freezing process starts	[°C] or [K]
T_2	Temperature at which the freezing process ends	[°C] or [K]
T_{ac}	Average air temperature for the control volume	[°C] or [K]
T_{dp}	Dew point temperature	[°C] or [K]
T_e	Exterior ambient temperature	[°C] or [K]
T_{epv}	PV exterior surface temperature of the control volume	[°C] or [K]
T_{ew}	Brick wall or PCM exterior surface temperature of the control volume	[°C] or [K]
T_i	Interior room temperature	[°C] or [K]
T_{in}	Air Cavity inlet temperature	[°C] or [K]
T_{ipv}	PV air cavity interior surface temperature of the control volume	[°C] or [K]
T_{iw}	Brick wall or PCM interior surface temperature of the control volume	[°C] or [K]
T_m	Mean air temperature in air cavity	[°C] or [K]
T_{mpv}	PV temperature at the middle of the module at the control volume	[°C] or [K]
T_{mw}	Brick wall or PCM temperature at the middle of the pane at the control volume	[°C] or [K]
T_{NOCT}	Nominal operating cell temperature	[°C] or [K]
T_{out}	Air Cavity outlet temperature	[°C] or [K]
T_{sky}	Sky temperature for radiative exchanges	[°C] or [K]
V	Output voltage	[V]

V_{ch}	Air speed in the channel	[m/s]
V_T	Thermal voltage of a solar cell	[V]
V_{wind}	Wind velocity	[m/s]
\overline{V}	Average velocity within air cavity	[m/s]

Greek

α	Solar absorptance	[]
β	Volumetric coefficient of expansion	[k ⁻¹]
β_c	Photovoltaic cell temperature coefficient	[k ⁻¹]
Δ	Difference or interval	-
ε_{pcm}	PCM long-wave emissivity	[]
ε_{pv}	PV long-wave emissivity	[]
η_0	Total system efficiency	[%]
η_e	Electrical efficiency	[%]
η_t	Thermal efficiency	[%]
η_{ts}	Summer thermal efficiency	[%]
η_{tw}	Winter thermal efficiency	[%]
κ	Thermal conductivity	[W/m.K]
μ	Dynamic viscosity	[N.s/m ²]
ν	Kinematic viscosity	[m ² /s]
ρ	Specific mass or Density	[kg/m ³]
Σ	Stefan-Boltzmann constant	[W/(m ² .K ⁴)]

Acronyms

<i>BIPV/T</i>	Building Integrated Photovoltaic/Thermal
<i>BIPV/T-PCM</i>	Building Integrated Photovoltaic/Thermal with PCM
<i>CFD</i>	Computational Fluid Dynamics
<i>GA</i>	Genetic Algorithm
<i>LNEG</i>	Laboratório Nacional de Energia e Geologia
<i>PCM</i>	Phase-change Material
<i>PV</i>	Photovoltaic
<i>PV/T</i>	Photovoltaic/Thermal
<i>UTC</i>	Un glazed Transpired Collector

Chapter 1. INTRODUCTION

1.1. INTRODUCTION

Increasing energy consumption, shrinking resources and rising energy costs have a significant impact on the standard of living for future generations. In these circumstances, the development of alternative, cost effective sources of energy for residential and non-residential buildings has to be a priority. In European Union, it is estimated that more than 40 % of energy is absorbed by the tertiary and residential sector, which is still expanding [1]. Currently, this energy consumption is mostly based on fossil fuels, which are the generators of emissions of greenhouse gases that have considerable environmental impacts. For this reason, reducing energy consumption, rather than saving costs, would contribute to a more balanced and sustainable environment. However, in practice the reduction in consumption levels should not be accompanied by a reduction in comfort levels, as this would lead (in technologically advanced societies) to a poorer quality of life. Thus, the energy savings should be governed by a new paradigm that promotes the rational use of energy, energy efficiency and the integration of renewable forms of energy. A study published by the Commission of the European Communities [2] has estimated savings of approximately 22% of

the present consumption in residential construction if energy efficiency measures are adopted for the energy used for heating, cooling, hot water and lighting. In this context, building designers are faced with the challenge of proposing new solutions that keep pace with growing modernization of societies in terms of urban design and environmental comfort, but that at the same time are environmentally balanced with respect to the resources they consume and harmful emissions they generate. Designing energy efficient and affordable solutions integrated in buildings and able to handle summer and winter climate challenges is a very ambitious goal. In addition, May 2010 saw the publication of the recast of the Energy Performance of Buildings Directive which sets Zero Energy performance targets for all new buildings [3].

The integration of PV systems into buildings is an imperative in this context. Solar energy collection and utilization systems that constitute an integral part of the building envelope or interior walls and floors save in installation and material costs. As is well known, only approximately 16% of the solar energy incident on PV is converted to electricity, the rest is absorbed and transformed into heat [4]. However, one major potential problem with PV integrated systems is overheating. Elevated operating temperatures reduce the solar energy conversion efficiency of monocrystalline technology photovoltaic modules.

This work is part of a full project “*FRAME-Prefabricated systems for low-energy buildings: design, modulation, prototyping and testing*” supported by Portuguese Foundation for Science and Technology (FCT) and coordinated by the National Laboratory for Energy and Geology (LNEG) with aims to develop a system that will address two important trends: one is improving indoor thermal comfort while at the same time reducing the building’s energy demands; the second is improving the efficiency of the photovoltaic system by limiting temperature rise inside the system. These two objectives can be achieved by ventilating the air gap behind the PV module and successfully recovering the heat released in the conversion process from the PV for indoor heating (BIPV/T), or by using PCM to regularize the indoor-outdoor temperature difference and the stabilization of the PV modules’ temperature (BIPV-PCM). The designing of such a system, however, is a very complex task that requires the scientific research (numerical and experimental) of the heat and mass transfer phenomena through the prefabricated module.

In order to fulfill successfully the main objectives of the project, numerical and experimental methodologies will be used. The objectives of this project will be developed over three specific tasks: **Task 1** will be dedicated to the numerical investigation of heat transfer occurring through the prefabricated module. The numerical heat transfer investigation through the module will be done using numerical modeling according to the complexity of the problem. The numerical approach will be used also for validation purposes and analysis of the system as a building component for future optimization. Follow the numerical study, an experimental study will be developed within **Task2**. Two prototypes will be constructed and tested. Task 1 and 2 concern

further intrinsic understanding and thermal behavior of the prefabricated facade module by way of experimental testing, backed up by computational simulations. In the last stage, under **Task 3**, the optimized model system will be analyzed with a building simulation tool with the purpose of assessing the energy savings of a typical building residential and non-residential (new and existing) integrating the prefabricated system on the building facade, in Portuguese climate.

1.2. OBJECTIVES

This work focuses on the first two tasks (**Task 1** and **Task 2**) of the project and it is set out to meet the objectives proposed below:

- Literature review on building integrated photovoltaic/thermal systems.
- Development of a model of the phenomena of heat and mass transfer, of this type of PV/T building integration, and evaluation of their results compared to those obtained experimentally. Find results of temperature field and heat fluxes through the whole system and in particular in the air cavity and PCM layer. Find and answer regarding the geometrical and physical features for which the system is likely to exhibit maximum performance.
- Experimental evaluation of the thermal behavior of building integration PV/T system, including the effects of ventilation on air cavity and phase-change material gypsum board behavior. The results will be further used to validate the numerical analysis.
- Optimization of the system for the maximum possible performance.

1.3. OUTLINE

The dissertation consists of seven chapters, with this introduction being the first of these chapters. **Chapter 1** starts with the description of the methodology employed in the work and ends with a brief outline of the thesis.

Chapter 2 presents a Building Integrated PV/T System review. The concept of building integrated PV/T is introduced and a brief review of the major works on this system is presented.

The thermal behavior and the ventilation conditions of this type of façade are characterized and the typologies most often adopted are identified.

Chapter 3 gives a detailed description of the three heat transfer modes, with particular emphasis on convection and on the dimensionless groups governing it. The same section also sets

out the concept of thermal mass and characterizes the properties of phase-change materials and modelling methods.

Chapter 4 The numerical approach is presented in the second section. It begins with problem formulation and system performance. This section also explains the software used for the simulations and for the design of the prototype.

Chapter 5 concerns the experimental work performed at the SOLAR XXI building of National Laboratory of Energy and Geology in Lisbon. This chapter continues with an interpretation of the experimental results. The validation of the numerical model is the last section off this chapter. The thermal behavior of this system is simulated and compared with experimental results.

Chapter 6 presents a system optimization with the genetic algorithms method. The optimization method is described and the optimization scenarios are presented. The optimization results follow the explanation how the method is applied.

Chapter 7 summarizes the main results of this work and indicates the direction for further research.

Chapter 2. BUILDING INTEGRATED PV/T SYSTEMS (BIPV/T) REVIEW

2.1. INTRODUCTION

The integration of photovoltaic modules in the building envelope is a promising technology for sustainable construction. They can replace conventional construction elements and generate energy and heat simultaneously. When electricity and useful heat is generated by a building integrated photovoltaic (BIPV) system [5] it is defined as a BIPV/thermal or BIPV/T.

In these building integrated photovoltaic (BIPV) systems, PV modules are installed as functional components of the building envelope. Because elevated temperatures are prejudicial to the performance of photovoltaic modules, a cooling fluid can be circulated to remove thermal energy from BIPV systems. Normally the fluid is water or air. These systems have several advantages. First, the multiplicity of functions can significantly reduce costs. Second, the electrical efficiency of the PV modules can be considerably improved. Finally, the proximity to the loads reduces transmission losses of electricity and heat [6].

Although there are several studies related to PV/T and BIPV systems, this review focuses on building integrated systems with simultaneous production of photovoltaic and thermal energy (BIPV/T).

There are several properties that define the BIPV / T systems. Fig. 2.1 summarizes the topics to be analyzed.

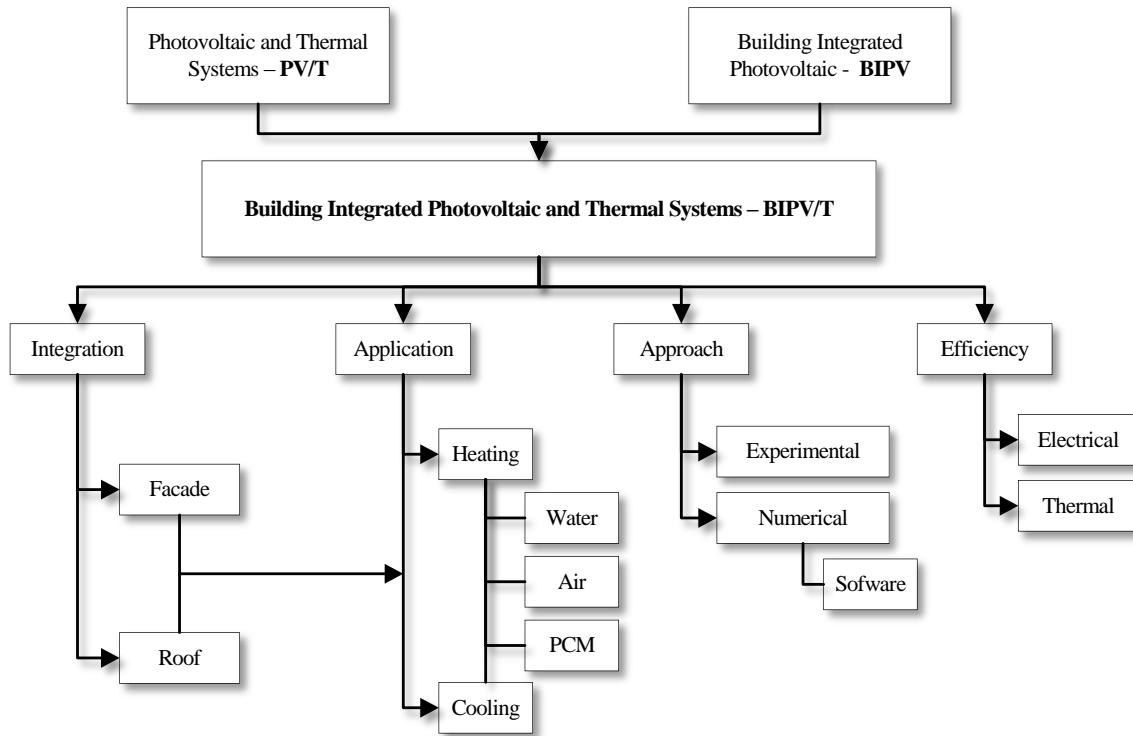


Fig. 2.1. Review specific subjects.

2.2. INTEGRATION / APPLICATION

BIPV/T systems are designed to replace the traditional building components totally or partially, thus ensuring a cross-functional role.

According to an NREL study [7], facade applications typically include a vertical curtain wall, inclined curtain wall, and stepped curtain wall; roof applications normally include inclined roofs and skylight monitors. IEA Task 41 [8] reports a quite complex approach to solutions for integrating PV as a different building envelope component (tilted roof, flat roof, skylight, facade cladding, facade glazing, external device). The same publication reports on two different approaches and definitions of PV integration: BAPV-Building Added Photovoltaic systems where photovoltaic modules are most commonly considered just as technical devices added to the building, and BIPV-Building Integrated Photovoltaic systems, where photovoltaic modules are

integrated in the building envelope as constructive systems and they may form part of the building facade, the roof, or both simultaneously.

The application of this kind of system depends on the building demands (space heating, DHW heating) or/and on strategies for enhancing module efficiency (cooling, ventilation). Another important issue associated with different applications is the fluid circulating under the PV module, which may be water or air. The choice of technique depends on the location and application, which dictates the usage of appropriate design criteria. For BIPV however, the fluid most commonly used for cooling, ventilation of the cavity under PV, and also for space heating (heat recovery) is air.

Facade

Most photovoltaic facades are built as curtain facades in front of thermally insulated buildings, with air ducts in between. This implies additional costs for the support structure and installation, while heat dissipation from the solar cells is often not optimal. To deal with these issues, authors like Krauter (1999) et al. [9], carried out one of the earliest laboratory studies with the integration of a thermal insulating layer into the PV facade, plus additional cooling by active ventilation or water flow. In relation to water as the working fluid, Chow et al. (2006-2009) [10–13] published several works on the application of PV modules on building facades with heat recovery that can serve as water pre-heating system. Chow (2010) [14] published a very useful review on photovoltaic/thermal hybrid solar technology. A wall-mounted hybrid photovoltaic/water-heating collector system was performed by Ji et al. (2003-2006) [15,16].

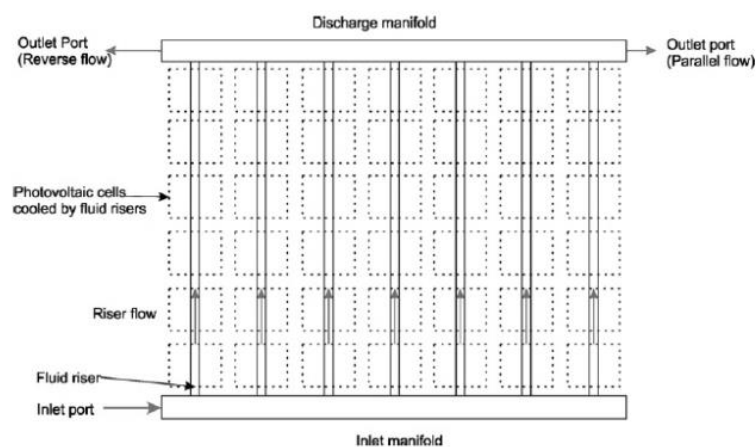


Fig. 2.2. Example of a scheme of a water based BIPV/T applied on a facade [17]

An investigation was carried out by Ghani et al. (2012) [17,18] to determine the effect of flow distribution on the photovoltaic yield of BIPV/T collectors of varying size. Ibrahim et al. (2014) [19] designed a BIPV/T system to produce both electricity and hot water. The hot water was produced with a spiral flow absorber at the back of the PV. Fig. 2.2 shows an example of a scheme of a water based BIPV/T applied on a facade.

Air seems to be the choice of working fluid for many authors. Ji et al. (2003-2006) [20–22] and Koyunbaba et al. (2011) [23] studied the application of photovoltaic modules on ventilated Trombe walls. Some studies are only numeric, such as Infield et al. (2003) [24], who studied the performance of ventilated facades, and Dehra (2008) [25], who developed a model for a forced ventilated PV solar wall. Other studies on BIPV/T are devoted to the model simulation of radiation and convection (laminar and turbulent), such as Muresan et al. (2006) [26]. Kim and Kim (2012) [27] compared three different of BIPV/T system configurations. The study analyzed the system performance as well as the building performance. Various researchers (Lin et al. (2011) [28]; Ho et al. (2012) [29]) have studied the energy performance and efficiency of actively air cooled PV modules integrated into facades. Fig. 2.3 shows an example of a BIPV/T system installed on the facade of the SOLAR XXI building. This example represents the air cavity heat recovery and cooling of the PV module.

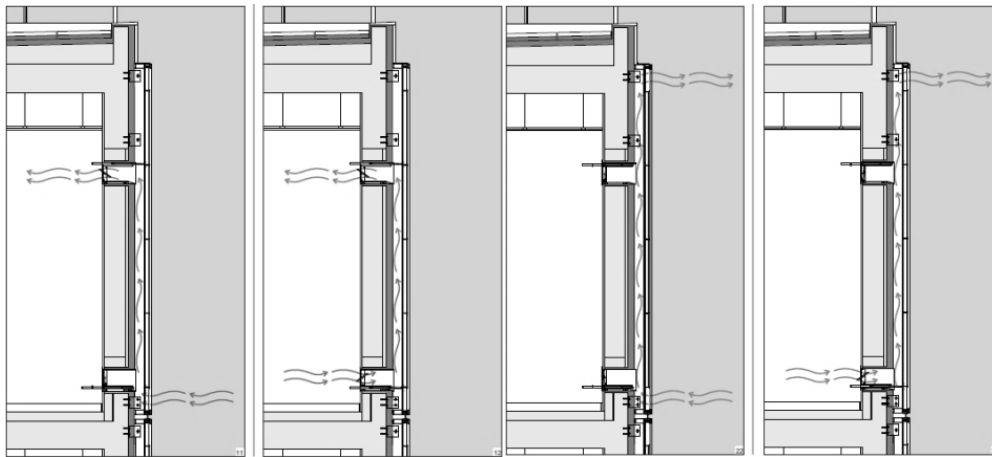


Fig. 2.3. Schematic of a BIPV/T applied on a façade – SOLAR XXI Building [30]

One of the strands of BIPV/T systems is a PV/T system integrated with a transpired solar collector. A full scale prototype was studied by Athienitis et al. (2010) [31] who proposed a highly efficient collector, an open-loop Unglazed Transpired Collector (UTC) which consists of dark porous cladding through which outdoor air is drawn and heated by absorbed solar radiation. The BIPV/T concept was applied to a full scale office building demonstration project, and the ratio of photovoltaic area coverage of the UTC could be selected based on the fresh air heating needs of

the building, the value of the electricity generated and the available building surfaces. Shukla et al. (2012) [32] published a useful review on the performance of transpired solar collectors. Fig. 2.4 shows a concept schematic for a BIPV/T system with transpired collector.

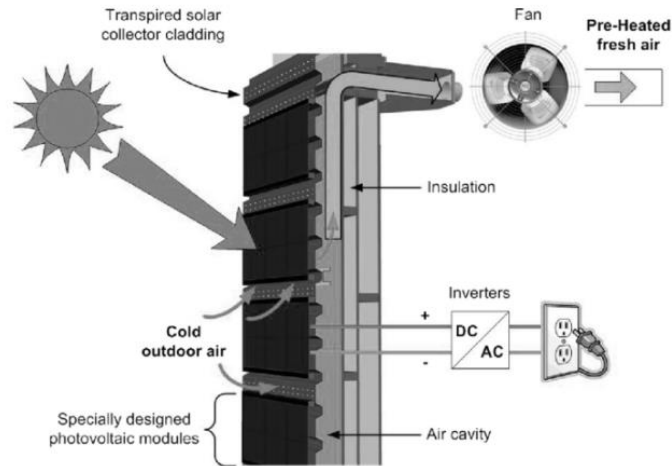


Fig. 2.4. Concept schematic for a BIPV/T system with transpired collector [31].

Innovative configurations were presented by Athienitis et al. 2005 [33] and later by Aelenei et al. (2013) [34–37], in which an experimental façade was built and studied, with the application of various configurations and materials.

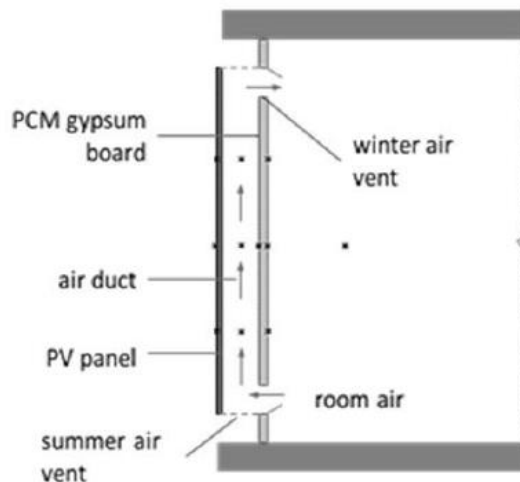


Fig. 2.5. Example of a scheme of an air-based BIPV/T with PCM, applied on a façade [37]

In the daytime, phase-change material was used to regulate the temperature peaks of the photovoltaic module. At night, the melted PCM solidifies and delivers heat that keeps the panel warm for a prolonged period of time. The purpose of the BIPV-PCM and the expected behavior is

to keep the outside wall temperature warm (over 20°C), to prevent heat loss through the wall [35]. Fig. 2.5 shows an example of a scheme of an air-based BIPV/T with PCM, applied on a facade.

Roof

After the facade, the roof is the next most studied location regarding the application of BIPV/T systems. The systems are quite similar to those used for facades; however, the fact that the roof is a tilted surface significantly improves the performance of PV as well as the absorption of energy by the system. The roof tilt angle assigns different flow characteristics to the air cavity.

Wang et al. (2006) [38] used four different roofs with air based BIPV/T systems to assess the impact of the BIPV on a building's heating and cooling loads, i.e. ventilated air-gap, non-ventilated air-gap, close-roof mounted, and conventional roof. Anderson et al. (2009) [39] published a study on the performance of a coolant based BIPV/T applied to a titled roof. A comparative study of four different configurations and the life cycle cost assessment of a ventilated BIPV/T system applied on a sloped roof was presented by Agrawal and Tiwari (2010) [40,41]. Corbin and Zhai (2010) [42] took advantage of a previous experimental work to investigate the roof mounted BIPV/T collector in order to determine the effect of the heat recovery on cell efficiency and the effectiveness of the device as a solar hot water heater.

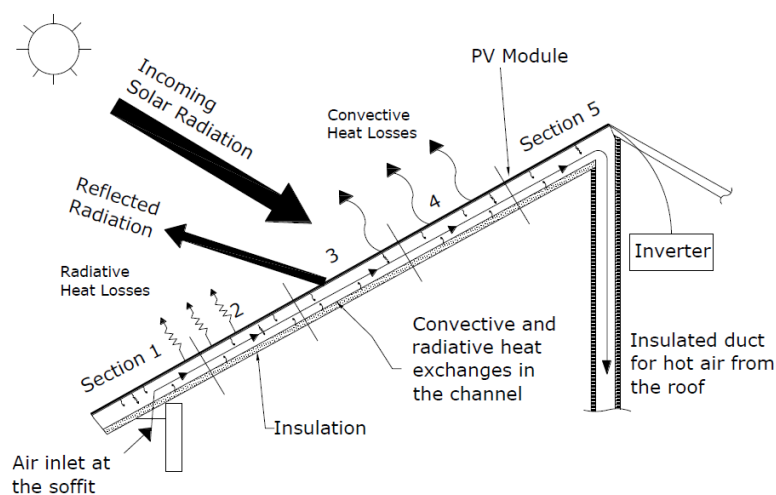


Fig. 2.6. Schematic of a BIPV/T applied on a roof [6]

Over the last few years, several customized mathematical models have been developed for these systems. Chen et al. (2010) [43], Candanedo et al. (2010) [6] and Pantic et al. (2010) [44] modeled and designed a forced ventilated BIPV/T system installed on the roof of a demonstration house. Shahsavari et al. (2011) [45] analyzed energy savings in buildings that use BIPV/T roof systems for interior room air heating. Vats et al. (2012) [46–48] performed an analysis of energy,

exergy and the packing factor of a semi-transparent ventilated BIPV/T system. Fig. 2.6 shows an example of a BIPV/T system installed on roof.

Yin et al. (2013) [49] designed and studied the performance of a completed system of a water based BIPV/T installed on a roof with interior room storage. The substrate of the panel was designed to be integrated into the building skin, allowing the panel to serve as both structural sheathing and waterproofing. This eliminates the material redundancies of current industry standard designs and the embodied carbon associated with those materials. The integration of the panel into the building skin also eliminates the waterproofing problems associated with the roof penetrations required to mount conventional panels on a sloped surface.

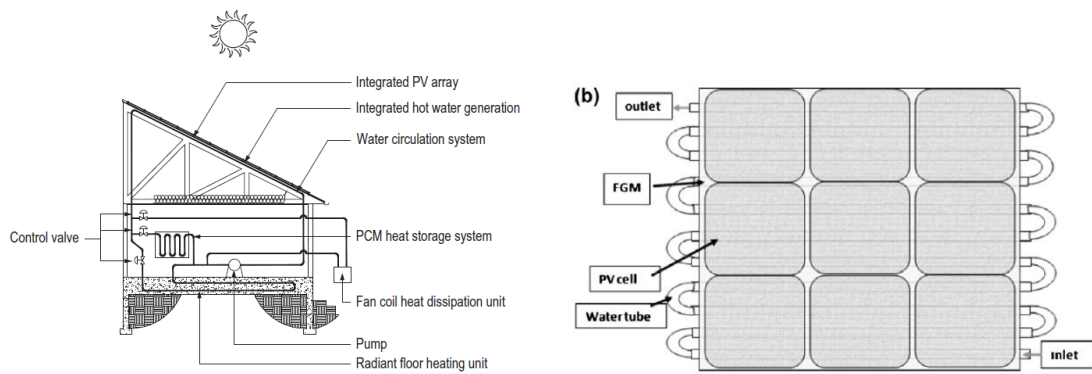


Fig. 2.7. a) Schematic of a water based BIPV/T applied on a roof, b) Schematic of a water based PV/T [49]

2.3. APPROACH

Experimental and numerical approaches have been used to explore PV building integration, its design and performance. In 1999, Krauter et al. [9] conducted an experimental study for a BIPV/T system. Other authors have developed numerical work for various BIPV/T systems [24,26,38,48].

Authors seem to favor a combination of numerical and experimental approaches. Depending on the level of detail and the parameters studied, the heat transfer across these systems can be modeled using a simple thermal network model to a more complex, Computational Fluid Dynamics (CFD). Fig. 2.8 shows an example of a thermal network.

The simpler models that use a thermal network approach (Fig. 2.8) tend to use standard programming software. Athienitis et al. (2005) [33] used Matlab[®] to implement a double facade for pre-heating fresh air, generating electricity with integrated photovoltaic panels and storing solar energy in phase-change material. A simple transient numerical control volume model is developed for the heat transfer in the PCM.

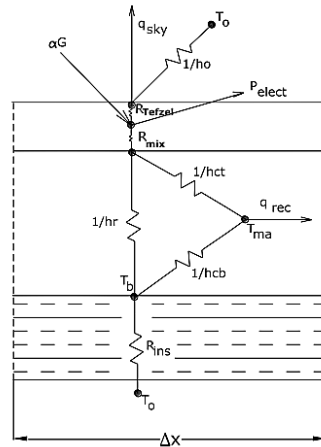


Fig. 2.8. Example of a thermal network of a BIPV/T roof system [6].

This type of approach allows the application of different configurations. In this same work, different types of facade systems were studied with computer simulations and full scale experiments. Matlab[®] was also used by Agrawal and Tiwari (2010) [40] to evaluate the performance and compute the useful exergy for four combinations of the BIPVT systems, i.e. case 1–case 4, at constant mass flow rate and constant velocity of air. The authors used the same software to evaluate the efficiency and life cycle cost of the above BIPV/T system. Candanedo et al. (2010) developed two thermal models for the same system – Steady State Model and Transient Model - both were conceived in Matlab[®]. This software includes interfaces for dynamic systems simulations, such as Simulink[®]. Aelenei et al. (2013) [36,37] used Simulink[®] to implement a model of a BIPV/T-PCM. This model included a physic mode simulation with Simscape[®] library.

For a more complex approach, some authors resort to computer simulation with CFD techniques for different BIPV/T systems. The CFD simulation solves the Reynolds Average Navier-Stokes form of the governing partial differential equations for fluid flow and heat transfer with a finite volume method. Corbin and Zhai (2010) [42] used CFD simulation on the basis of the experimental tests. Koyunbaba et al. (2011) also used this approach to model a BIPV Trombe wall. A study of energy efficiency and ventilation performance of a ventilated BIPV wall was performed by Lin et al (2011) [28]. This type of software contains the broad physical modeling capabilities needed to model the flow, turbulence, heat transfer, and reactions of many systems. Ghani et al (2012) [17] studied the effect of distribution on the PV performance of a BIPV/T collector using a CFD simulation program, Multi Physics Comsol[®]. A three step numerical analysis was conducted to model flow distribution, temperature variation, and photovoltaic yield for a PV/T collector whose design, geometric shape, and operating characteristics varied in order to vary flow uniformity within the collector. ANSYS Fluent[®] and TRNSYS[®] are also widely used to find out the impact of wind flow around the collector and to study different shapes of collector. These simulations are capable of providing very useful and accurate information, if accurate

boundary layer conditions are provided. TRNSYS is basically used by researchers to study the overall performance of systems and for parametric analysis [50]. Kim and Kim (2012) [27] used TRNSYS for modeling an air-type building integrated photovoltaic-thermal system and it was also used by Kalougrinou (2001) [51] for modeling a hybrid PV-thermal solar system. Thevenard (2005) [52] used ESP-r, which proved very useful for estimating the electrical and thermal impact of building integrated photovoltaics. These studies vary from the test room facilities [33] to studies of large scale applications [6].

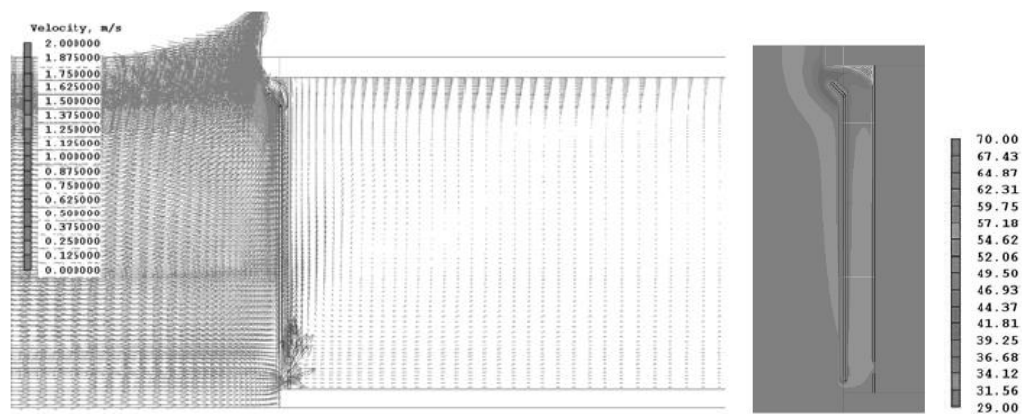


Fig. 2.9. Example of a CFD simulation flow pattern (left). Example of a CFD simulation PV temperature (right) [28].

2.4. EFFICIENCY

Researchers strive to improve the energy efficiency of systems, since some energy is lost in each of the conversion processes. More complex systems that have many components are typically less efficient than simple systems. This is no different for BIPV/T systems. The aim is to make such systems as simple as possible, and as efficient as possible. Making systems that include energy conversions more efficient can help to reduce energy consumption and the production of greenhouse gas emissions. Parameters such as solar radiation and airflow rate, wind velocity, orientation, location, exterior temperature, slope, and material properties are particularly important.

There does seem to be a direct relation between the higher efficiencies obtained by the authors and the type of systems studied (facade, roof, air or water) (Fig. 2.10). Efficiencies of integrated systems in the roof have higher values than those integrated in the facade.

Applications in facades with air as working fluid achieved overall system efficiency between 20.9% and 63% (Jie et al. (2007) presented only the electrical efficiency). Athienitis et al. (2011) [31] demonstrated a high maximum efficiency (63%) system with 50.5% thermal efficiency and 12.5% electrical efficiency. The study was conducted with full-scale prototypes made specifically

for this purpose, including custom PV modules. Other authors showed efficiency values considered normal for such systems [23,24,37]. Looking at integrated systems in facades, we can see that systems with water as the working fluid had higher efficiency (47.5% – 62.3%) than those with air as the working fluid. However, there are too few published papers to establish a rule. Ibrahim et al. (2014) [19] achieved a total maximum efficiency of about 62.3% with 51% thermal and 11.35% electrical, for a spiral flow absorber of water based BIPV/T system.

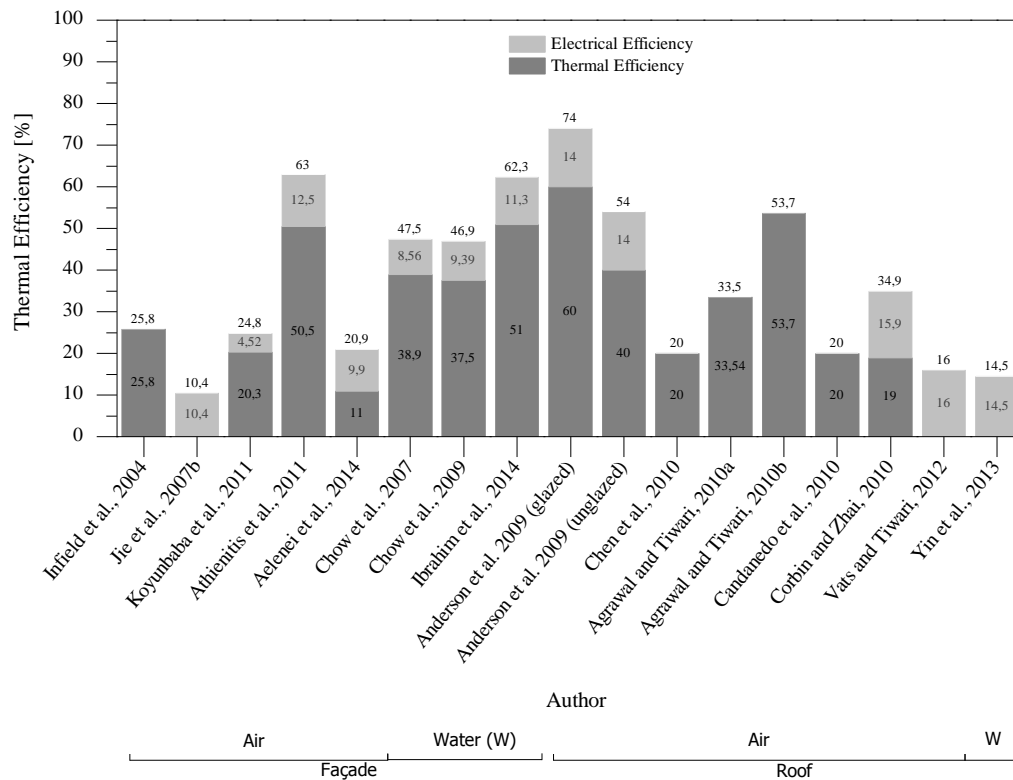


Fig. 2.10. Graphical summary of the efficiency obtained by the authors.

In Fig. 2.10 we can see that the roof applications have mainly had air as the working fluid. The maximum total efficiencies vary between 14.5% and 74%, for authors who only reported thermal or electrical efficiency. The total maximum efficiency presented by authors is generally greater than the efficiency of systems integrated in the facade. These results are best explained by the slope of the roof relative to the sun. Anderson et al. (2009) [39] presented a study of an unglazed BIPV/T solar collector performance with an overall maximum efficiency of 74%, where 60% is thermal and 14% is electrical efficiency. In the same study, the author described a glazed BIPV/T system with an overall maximum efficiency of 54%, (40% thermal, 14% electrical).

Chapter 3. BASIC FUNDAMENTALS OF HEAT AND MASS TRANSFER

3.1. INTRODUCTION

The basic fundamentals of heat and mass transfer used to solve the heat transfer phenomena's across the system is described in this sub-chapter. The conduction, convection and radiation heat transfer modes considered in this study are first briefly reviewed. Then a description of the thermal mass concept is presented. This sub-chapter ends with reference to the phase-change material notion and its numerical approaches.

3.2. HEAT TRANSFER

In physics, the heat transfer or propagation is the transition of thermal energy from a warmer to a cooler mass. In other words, it is the exchange of heat energy between two systems of different temperatures.

The energy, called thermal energy in this case, mainly passes from one body to another in three ways: conduction, convection and radiation. These three modes of heat transfer will be described

separately, but in most cases they occur simultaneously. Conduction is the transfer of energy between adjacent bodies or adjacent parts of a body. Convection is the transfer of energy between a body and its environment, due to fluid motion. Radiation is the transfer of energy to or from a body by means of the emission or absorption of electromagnetic radiation.

Consider the very simple system shown schematically in Fig. 3.1 consisting of two bodies with an air gap (either open or closed) between them.

Assuming that there is a temperature difference between the outer (T_e) and inner (T_i) boundary environments, the three heat transfer phenomena mentioned above - conduction, convection and radiation - will occur. In fact, in the two system components, which are solid elements, the heat transfer takes place by conduction only, while in the air cavity the three heat transfer phenomena can coexist.

Finally, regarding the surfaces that are in contact with indoor or outdoor environments, the phenomena of thermal radiation to the surrounding surfaces and convection with the adjacent air in motion will occur. All these phenomena will be described.

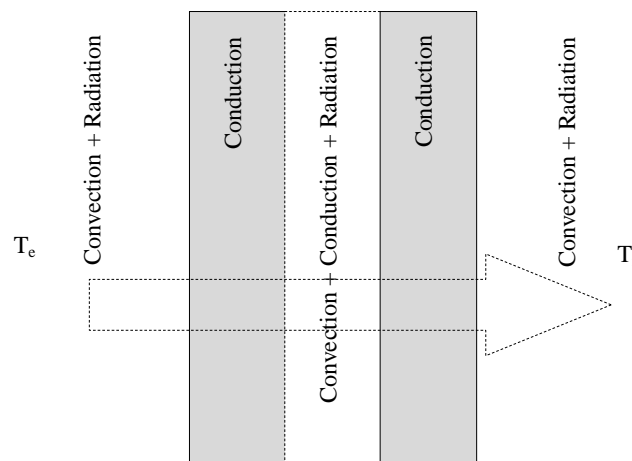


Fig. 3.1. Heat transfer through a ventilated air cavity wall system [53]

3.2.1. Conduction Heat Transfer

Heat transfer by conduction is a process that takes place in the presence of temperature differences between two points of a body. This exchange of energy takes place from the region of higher temperature to the lower temperature region by kinetic motion or the direct impact of molecules and atoms [54]. This phenomenon is governed by Fourier's law, which states that the flow of heat by conduction in a specific direction is proportional to the normal direction, to the

direction of flow and to the temperature gradient in this direction. For the one-dimensional plane wall show in Fig. 3.2, having a temperature distribution $T(x)$, the rate equation is expressed as:

$$q_x'' = -k \frac{\partial T}{\partial x} \quad (3.1)$$

where the heat flux q_x'' (W/m²) is the heat transfer rate in the x direction per unit area perpendicular to the direction of transfer, and it is proportional to the temperature gradient, $\partial T/\partial x$ in this direction, and the proportionality constant k is a transport property known as the material thermal conductivity (W/m.K). Under the steady-state conditions (Fig. 3.2), with linear temperature distribution, the temperature gradient may be expressed as:

$$\frac{\partial T}{\partial x} = \frac{T_2 - T_1}{L} \quad (3.2)$$

then,

$$q_x'' = -k \frac{T_2 - T_1}{L} = k \frac{T_1 - T_2}{L} = k \frac{\Delta T}{L} \quad (3.3)$$

The heat rate by conduction, q_x (W), through a plane wall of area A (m²) is the product of the flux and the area:

$$q_x = q_x'' \cdot A = -k \frac{T_2 - T_1}{L} A = kA \frac{T_1 - T_2}{L} = kA \frac{\Delta T}{L} \quad (3.4)$$

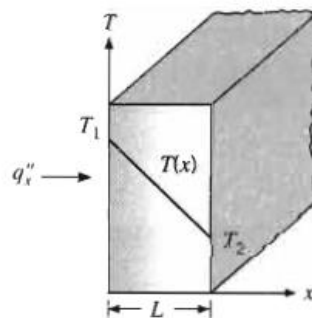


Fig. 3.2. One-dimensional heat transfer by conduction [55]

3.2.2. Convection Heat Transfer

The fluid flow at a given temperature over a solid body at a different temperature causes a transfer of heat that is known as surface convection (Fig. 3.3). In general, this heat transfer can be described by Newton's law:

$$q_c'' = h_c \cdot \Delta T \quad (3.5)$$

where q_c'' , the convective heat flux (W/m^2), is proportional to the difference between the surface and fluid temperatures ΔT , and h_c is the local convective heat transfer coefficient ($\text{W}/\text{m}^2 \text{K}$).

The heat rate by convection q (W), is the product of the convective heat flux q_c'' and the transfer surface area A (m^2):

$$q_c = q_c'' \cdot A \quad (3.6)$$

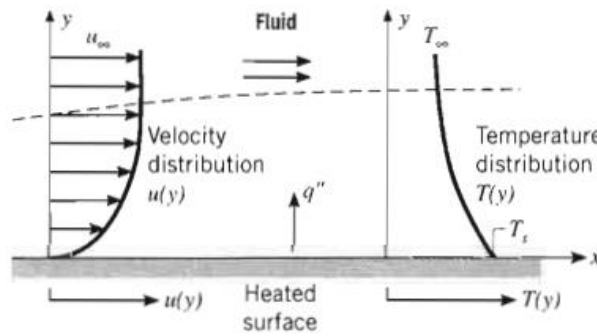


Fig. 3.3. Boundary layer development in convection heat transfer [55]

Given the wide variability of possible values of h , it is more practical and rational from the scientific point of view for this magnitude to depend on dimensionless parameters.

3.2.2.1. Heat transfer dimensionless numbers

Several dimensionless parameters used to characterize the phenomenon of convection are described in literature. The physical meaning of the dimensionless parameters used in this work to study the phenomenon of convection is described next. These parameters are the Reynolds (Re), Prandtl (Pr), Grashof (Gr), Rayleigh (Ra) and Nusselt (Nu) numbers.

Reynolds number

The Reynolds number represents the ratio between inertia forces and viscous forces:

$$Re = \frac{\text{Inertia forces}}{\text{Viscosity forces}} = \frac{\rho V^2 / \ell}{\mu V / \ell^2} = \frac{\rho V \ell}{\mu} = \frac{V \ell}{\nu} \quad (3.7)$$

Where ρ is the specific mass of the fluid (kg/m^3), V is the average velocity (m/s), ℓ is the characteristic length [m] and μ and ν are, respectively, the dynamic (N.s/m^2) and kinematic (m^2/s) viscosity of the fluid.

As the Reynolds number increases, the inertia forces become dominant relative to the viscosity, the velocity and pressure fluctuations increase, and the flow may change from laminar to turbulent. Some authors [54] describe a critical Reynolds number where this transition occur. This value depends strongly on the surface roughness and the level of turbulence flow. The characteristic length ℓ , depends on the geometry of the problem. If the flow is over isolated plates, the characteristic length is the distance from the leading edge of the plate, if flow is in ducts, the length is the value of the hydraulic diameter (D_h) of the duct, which is defined as:

$$D_h = \frac{4A_{cr}}{P} \quad (3.8)$$

where the A_{cr} is the cross-sectional area (m^2) and P is the wetted perimeter.

Prandtl number

The Prandtl number is the ratio between the momentum diffusivity (kinematic viscosity) and the thermal diffusivity:

$$Pr = \frac{\nu}{\alpha_t} = \frac{\mu C_p}{k_f} \quad (3.9)$$

where, μ , K_f and C_p are the dynamic viscosity [N.s/m^2], the thermal conductivity (W/m.K) and the specific heat (J/kg.K), respectively.

Grashof number

The Grashof number represents the relationship between forcing forces and restraining forces; it has a similar role for natural convection as the Reynolds number has for forced convection:

$$Gr = \frac{\text{Buoyancy Forces}}{\text{Viscous Forces}} = \frac{g\Delta\rho V}{\rho v^2} = \frac{g\beta\Delta T \ell^3}{v^2} \quad (3.10)$$

Where g is the gravitational constant (m/s^2), $\beta \cong \Delta\rho/(\rho\Delta T)$ is the volumetric coefficient of expansion, Pr is the Prandtl number, ℓ is the characteristic length [m] (gap between two layers), v is the kinematic viscosity (m^2/s) and ΔT is the temperature difference between two layers.

As in forced convection with the Reynolds number, in naturally occurring convection there is also a critical Grashof number for which the fluid ceases to have laminar characteristics and changes to a turbulent regime.

Rayleigh number

The Rayleigh number is a dimensionless characteristic parameter of the phenomenon of heat transfer in a fluid and has relative importance for the phenomena of conduction and convection. Conduction is the dominant phenomenon of transfer for Rayleigh numbers of less than a certain critical value of the specific fluid, and convection is the prevailing phenomenon for Rayleigh numbers greater than this value.

The Rayleigh number is the product of the Grashof number and the Prandtl number:

$$Ra = PrGr = \frac{g\beta'Pr}{v^2} \Delta T \ell^3 \quad (3.11)$$

where g is the gravitational constant (m/s^2), β is the volumetric coefficient of expansion, Pr is the Prandtl number, l is the characteristic length (m), v is the kinematic viscosity (m^2/s) and ΔT is the temperature difference between two layers.

Nusselt number

The Nusselt number represents the ratio of the actual flow of heat that occurs between a surface and the adjacent fluid, and the heat flow that would occur if the heat transfer was purely by conduction:

$$Nu = \frac{q}{k_f \Delta T / \ell} = \frac{h_c \Delta T}{k_f \Delta T / \ell} = \frac{h_c \ell}{k_f} \quad (3.12)$$

where q is the flux density at the surface (W/m^2), ΔT is the temperature difference between the surface and the fluid (K), h_c is the superficial convective heat transfer coefficient ($\text{W}/\text{m}^2\text{K}$), k_f is the thermal conductivity of the fluid ($\text{W}/\text{m}\cdot\text{K}$), and ℓ is the characteristic length (m).

The Nusselt number may also be viewed as a dimensionless temperature gradient in the boundary layer very close to the solid surface area. Higher Nusselt numbers mean that the heat exchanges are enhanced by convection.

The Nusselt number is expressed in terms of dimensionless parameters which vary according to the nature of the flow (Table 3.1). In a forced convection flow, the Nusselt number is usually a function of the Reynolds number and Prandtl number, while in natural convection it depends on the Rayleigh number. Finally, in mixed convection flows, the Nusselt number is expressed as a function of both the Reynolds and Rayleigh numbers.

Table 3.1. Nusselt number relations depending on the nature of the flow

Natural Convection	Forced Convection	Mixed Convection
$Nu = f(\text{Ra})$	$Nu = f(\text{Re}, \text{Pr})$	$Nu = f(\text{Re}, \text{Ra})$

The literature reports the use of relations of this kind to characterize the phenomenon of convection in the air cavity that can be used in the numerical model of this work to estimate the value of the surface thermal conductance convection, h_c ($\text{W}/\text{m}^2\text{K}$), by the following equation:

$$h_c = \frac{Nu k_f}{\ell} \quad (3.13)$$

Where h_c is the superficial convective heat transfer coefficient ($\text{W}/\text{m}^2\text{K}$), Nu is the Nusselt number, k_f is the thermal conductivity of the fluid ($\text{W}/\text{m}\cdot\text{K}$) and ℓ is the characteristic length (m).

3.2.3. Radiation Heat Transfer

All bodies emit and absorb electromagnetic radiation at different wavelengths, whose intensity is a function of the absolute temperature and type of surface. Unlike the heat transfer phenomena described above, heat radiation needs no medium or support material to be processed [55].

Despite a PV module is opaque to infrared radiation, there is flux through the longwave radiation absorption and re-emission process. Solar radiation (short wave) is transmitted, reflected

and absorbed in each layer, depending on the optical properties of each element. In this type of study, where the first layer is completely opaque, it makes sense only to study the transfer of heat by radiation of long wave, where are determined the radioactive liquid fluxes of longwave that emit from each surface to its adjacent.

3.2.3.1. Long Wave Thermal Radiation

The law that governs the amount of power radiated from a pure radiant body, commonly termed a black body, at absolute temperature T_s (K), is called the Stefan-Boltzmann law and is expressed by:

$$E_b = \sigma T_s^4 \quad (3.14)$$

where σ is the Stefan-Boltzmann constant ($\sigma = 5.67 \times 10^{-8} \text{ W/m}^2 \cdot \text{K}^4$) and E_b is the radiation flux emitted by the black body per unit area (W/m^2), which integrates the entire range of lengths wave emission spectra [55].

The heat flux emitted by a real surface is less than that of a blackbody at the same temperature and is given by:

$$E = \epsilon \sigma T_s^4 \quad (3.15)$$

where ϵ is a radiative property of the surface termed the emissivity. With values in range $0 \leq \epsilon \leq 1$, this property provides a measure of how efficiently a surface emits energy relative to a blackbody. It depends strongly on the surface material and finish.

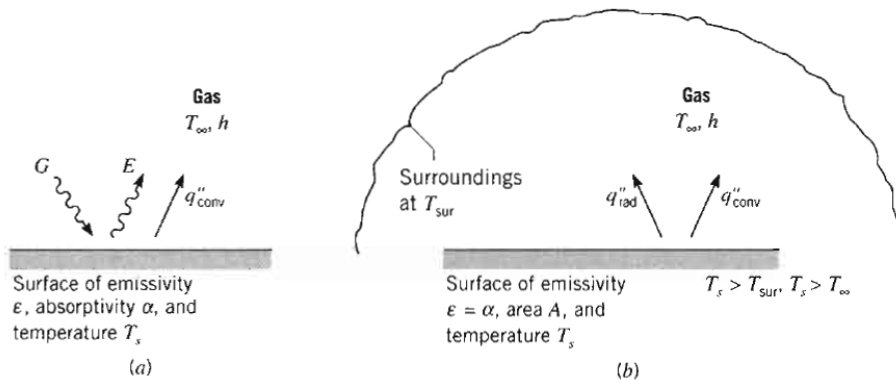


Fig. 3.4. Radiation exchange: a) at a surface and (b) between a surface and large surroundings [55]

If the surface is assumed to be considered a *gray surface* (Fig. 3.4), the net rate of radiation heat transfer from the surface, expressed per unit area (W/m^2) of the surface, is:

$$q_{rad}'' = \varepsilon\sigma(T_s^4 - T_{sur}^4) \quad (3.16)$$

where T_s is a small surface temperature (K), T_{sur} is a bigger surrounding surface temperature (K). The rate of heat transfer by radiation from one surface can be expressed by:

$$q_{rad} = \varepsilon\sigma A(T_s^4 - T_{sur}^4) \quad (3.17)$$

As can be seen from equation (3.17), the rate of radiative heat transfer between surfaces depends on the difference of the fourth power of the surface temperatures. In many engineering calculations, however, the heat transfer equations are linearized in terms of the differences of temperatures to the first power. For this purpose, the following mathematical identity is considered:

$$T_s^4 - T_{sur}^4 = (T_s^2 - T_{sur}^2)(T_s^2 + T_{sur}^2) = (T_s - T_{sur})(T_s + T_{sur})(T_s^2 + T_{sur}^2) \quad (3.18)$$

Therefore, equation (3.17) can be written as:

$$q_{rad} = h_r A(T_s - T_{sur}) \quad (3.19)$$

Where h_r is the radiation heat transfer coefficient modeled in a manner similar to convection. The radiation rate equation was linearized, making proportional to temperature difference rather than to the difference between two temperatures to fourth power. Note however, that h_r depends strongly on temperature, while the temperature dependence of convection heat transfer coefficient h_c is generally weak. This radiation heat transfer coefficient h_r considers not only the temperature of the surfaces and their characteristic but also their geometric orientation with respect to each other. The effects of the geometry of radiant energy exchange can be analyzed conveniently by defining the term *view factor*, F_{12} , to be the fraction of radiation leaving surface A_1 that reaches surface A_2 . The radiation heat transfer coefficient h_r will be described in 4.2.1.

3.2.3.2. Sky radiation

It is necessary to evaluate the radiation exchange between a surface and the sky. The sky can be considered as a black body at some equivalent sky temperature T_{sky} so that the actual net radiation between a horizontal flat plate and the sky is given by equation (3.19). The net radiation from a surface with emittance ε and temperature T to the sky at T_{sky} is:

$$q_{rad} = \sigma A \varepsilon (T^4 - T_{sky}^4) \quad (3.20)$$

The equivalent black body sky temperature of equation (3.20) accounts for the facts that the atmosphere is not at a uniform temperature and it radiates only in certain wavelength bands. The atmosphere is essentially transparent in wavelength region from 8 to 14 μm , but outside of this “window” the atmosphere has absorbing bands covering much of the infrared spectrum. Several relations have been proposed to relate T_{sky} for clear skies to measured meteorological variables. Duffie and Beckman [56] relate a relation for T_{sky} , where it is used an extensive data set from the United States to relate the effective sky temperature to the dew point temperature, dry bulb temperature, and hour from midnight t by the following equation:

$$T_{sky} = T_a \left[0.711 + 0.0056T_{dp} + 0.000073T_{dp}^2 + 0.013 \cos(15t) \right]^{1/4} \quad (3.21)$$

where T_a is the dry bulb temperature (K), T_{dp} is the dew point temperature ($^{\circ}\text{C}$). The used experimental data, covered a dew point range from -20°C to 30°C . The temperature between sky and air temperatures ranges from 5°C in a hot, moist climate to 30°C in a cold, dry climate.

3.3. THERMAL RESISTANCE

There exists an analogy between the diffusion of heat and electrical charge. Just as an electrical resistance is associated with the conduction of electricity, a thermal resistance may be associated with the conduction of heat. Defining a resistance as the ratio of a driving potential to the corresponding transfer rate, it follows from equation (3.4) that the thermal resistance for conduction in a plane wall is:

$$R_{t,cond} \equiv \frac{T_1 - T_2}{q_x} = \frac{L}{kA} \quad (3.22)$$

A thermal resistance may also be associated with heat transfer by convection at a surface. From equation (3.6) the thermal resistance for convection is then:

$$R_{t,conv} \equiv \frac{T_s - T_\infty}{q_c} = \frac{1}{hA} \quad (3.23)$$

From equation (3.19) it follows that a thermal resistance for radiation may be defined as:

$$R_{t,rad} \equiv \frac{T_s - T_{sur}}{q_{rad}} = \frac{1}{h_r A} \quad (3.24)$$

3.4. ENTHALPY TRANSPORT

Phenomena of heat transfer also occur between nodes inside the air cavity, and these have to be accounted for. There is a transport of energy by air (enthalpy transport) in the direction of flow, and the net balance between two sections can be calculated by the following expression [57]:

$$q_v = C_p \dot{m} (T_{in} - T_{out}) \quad (3.25)$$

where q_v is the resultant heat flow (W), C_p is the specific heat of air (J/kg K), \dot{m} is the mass flow between the nodes (kg /s), and T_{in} and T_{out} (K) are, respectively, the temperatures of the fluid at the inlet and outlet nodes of the air cavity. It is considered that in this model the flow rate is high enough for the phenomena of conduction in the flow direction to be disregarded.

3.5. THERMAL MASS

A simple transient heat transfer problem is one for which a component experiences a sudden change in its thermal environment. A system's thermal capacitance is the effective heat capacity of a structure per unit change of interior temperature, and it is important in a system that undergoes significant temperature changes. Thermal capacitance is of particular significance in passive heating or hybrid systems where storage is provided by the system itself. Thermal mass reflects the ability of a material or a combination of materials to store internal energy. The property is characterized by the mass of the material and its specific heat. The equation relating thermal energy q , to thermal mass is [55]:

$$q = M \cdot C_p \cdot \frac{\partial T}{\partial t} \quad (3.26)$$

where M is the mass of the material (kg) C_p is the material specific heat (J/kg.K), q is the energy (W) and $\delta T/\delta t$ is the time dependent temperature (K)

3.6. PHASE CHANGE ENERGY STORAGE

The use of a latent heat storage system using phase change materials (PCMs) is an effective way of storing thermal energy and has the advantages of high-energy storage density and the isothermal nature of the storage process. PCMs have been widely used in latent heat thermal-storage systems for solar engineering applications. The uses of PCMs for heating and cooling applications for buildings have been investigated over the past decade. There are large numbers of PCMs that melt and solidify at a wide range of temperatures, making them attractive for a number of applications [58].

Materials that undergo a change of phase in a suitable temperature range may be useful for energy storage if several criteria can be satisfied. The phase change must be accompanied by a high latent heat effect, and it must be reversible over a very large number of cycles, without serious degradation. The phase change must occur with limited supercooling or superheating, and means must be available to contain the material, and its containers must be reasonable. If these criteria can be met, phase-change energy storage systems can operate over small temperature ranges, have relatively low volume and mass, and have high storage capacity.

Phase-change materials oscillate between solid and liquid phase within a certain temperature range. The principle of operation is that when the environment's temperature is higher than that of the PCM, heat transfers from the surroundings to the material, which creates a cooling effect and changes the PCM's state from solid to liquid. When the environment's temperatures is lower than that of the PCM, heat transfers from the PCM to the surroundings, generating a warming effect and the PCM changes back to its solid state.

If a phase-change material is heated from T_1 to T_2 and undergoes a phase transition at T^* , its storage capacity is the sum of the perceptible heat change of the solid from T_1 to T^* , the latent heat at T^* , and the perceptible heat change of the liquid from T^* to T_2 :

$$Q_s = M \left[C_s (T^* - T_1) + \lambda + C_l (T_2 - T^*) \right] \quad (3.27)$$

where M is the mass of material, C_s and C_l are the heat capacity of the solid and liquid phases, and λ is the latent heat of phase transition.

Equation (3.27) can be schematized by Fig. 3.5. To characterize a PCM it is essential to know the transition temperature and the latent heat of phase change.

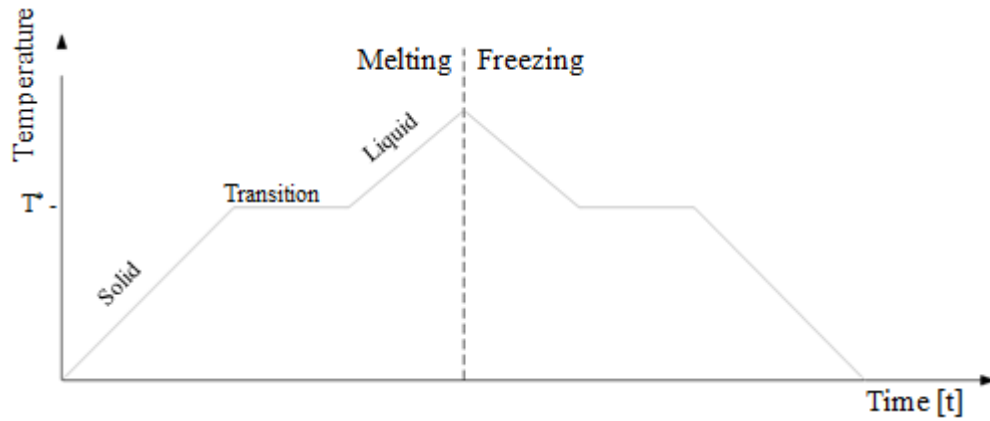


Fig. 3.5. Stages of a phase transition of a PCM

Chapter 4. HEAT TRANSFER NUMERICAL APPROACH

4.1. INTRODUCTION

In order to meet the proposed aim of this work, with the information gathered from the review in mind, it was developed a heat transfer numerical approach. The proposed model is based on an opaque façade system with ventilated air cavity.

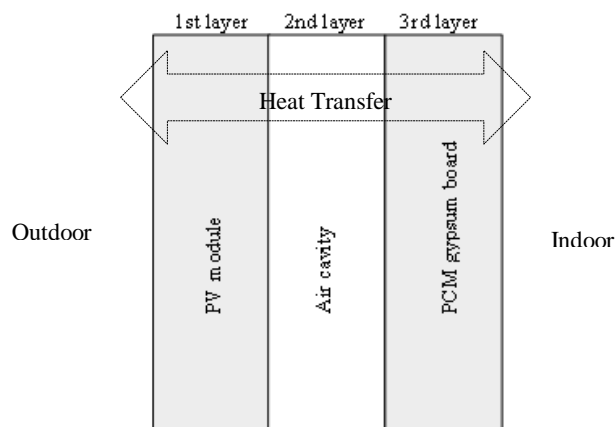


Fig. 4.1. System configuration

The system comprises a first opaque layer (PV module) an air cavity (ventilated or non-ventilated) and a second opaque layer (PCM gypsum board) (Fig. 4.1). An integrated building system is studied as an element consisting of several layers. The objective is to find results of temperature field and heat fluxes through the whole system.

This sub-chapter presents an integral equation model for evaluating the system's thermal performance. The program used for simulation is then briefly described.

4.1.1. Air velocity within the air cavity

A solution of Bernoulli's equation is used to estimate the mean velocity in the air cavity, based on the assumption that density and air temperature in the gap vary linearly with height [56]. The average velocity in the gap is

$$\bar{V} = \left[\frac{2gh}{\left[C_1 \left(A_g / A_v \right)^2 + C_2 \right]} \frac{T_m - T_s}{T_m} \right]^{1/2} \quad (4.1)$$

The term $[C_1(A_g/A_v)^2 + C_2]$ represents the pressure drop in the gap and vents, and C_1 and C_2 are dimensionless empirical constants. The wall height is h and T_m is the mean air temperature in the gap. The term T_s is either T_e or T_i depending on whether air is exchanged with the environment (T_e) or the room (T_i). Duffie and Beckman [56] say that, from data in Trombe et al. [59], values of C_1 and C_2 have been determined by Utzinger [60] to be 8.0 and 2.0, respectively.

4.1.2. PCM model approach

There are multiple methods to characterize a PCM. The literature contains several reviews on phase change materials. Papers by Nkwetta et al. [61] and Sharma et al. [58] give detailed descriptions of the type of materials used as PCMs. Al-Saadi and Zhai [62] review the modeling methods for PCMs. Different mathematical models and methods have been suggested in the literature that deal with phase change problems using the fixed grids method: enthalpy, heat capacity, temperature transforming method, and heat source method. Every method has its main distinct feature for the latent heat liberation, with advantages and disadvantages

In Athienitis et al. [63], the heat flux that represents equivalent internal heat "generation" caused by freezing the PCM at a specific temperature was modeled by the enthalpy method. The enthalpy method [64] simulates the heat released from solidification as a volumetric heat generation.

$$q_1 = \rho L_t \frac{df_s}{dt} \quad (4.2)$$

where f_s is the solid fraction in the two-phase region at the solidus front and L_t is the latent heat for complete phase transition.

The authors use a differential scanning calorimeter (DSC) test to obtain the latent heat L and the rate of solidification df_s/dt in equation (4.2) (Fig. 4.2(a)).

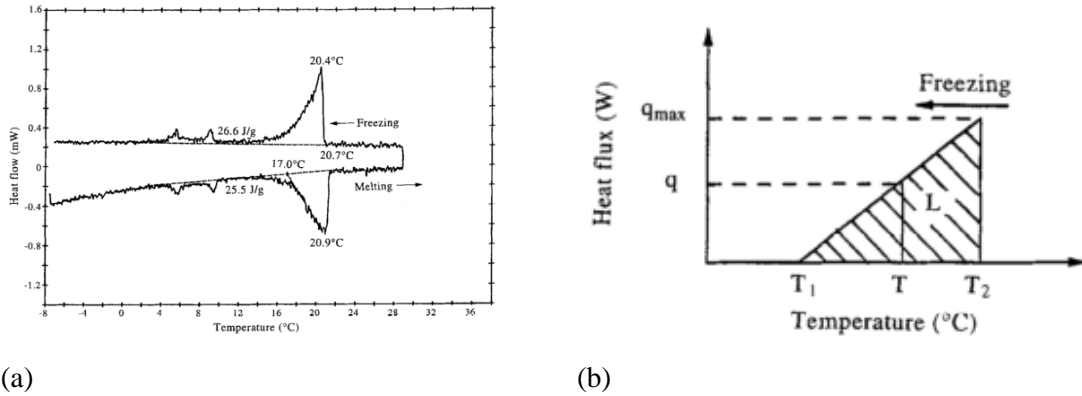


Fig. 4.2. (a) Phase transition curve for a PCM gypsum board from DSC test [63]. (b) Approximation of DSC curve [63]

The DSC curve was modeled in the temperature range of interest, T_1 and T_2 , respectively, indicate the temperature at which the freezing process starts and ends and q_{max} indicates the maximum latent heat flux (Fig. 4.2(b)). The area of triangle $T_1 T_2 q_{max}$ is the value of latent heat for the phase transition range T_1 to T_2 . With a known heating or cooling rate, R , we have

$$L_p = \frac{1}{2} \cdot q_{max} (T_2 - T_1) \cdot \frac{1}{R} \quad (4.3)$$

From trigonometry and interpolation, Athienitis et al. found the expression for q_1 determined at a temperature T as

$$q_1 = 2 \cdot L_p \cdot R \frac{T - T_1}{(T_2 - T_1)^2} \quad (4.4)$$

Comparing the DSC curves with the approximation, it was found that the relationship between L_p and L_t is $L_p = 0.62 \times L_t$.

Since the gypsum board used by Athienitis et al., is almost identical to that used in this work, the approach that defines equation (4.4) has been adopted to model the PCM layer in the present study.

4.2. PROBLEM FORMULATION

Heat transfer across a system can be considered as a set of nodes connected by a thermal network, each with a temperature and capacitance. The numerical analysis considers the schematic thermal network of Fig. 4.3.

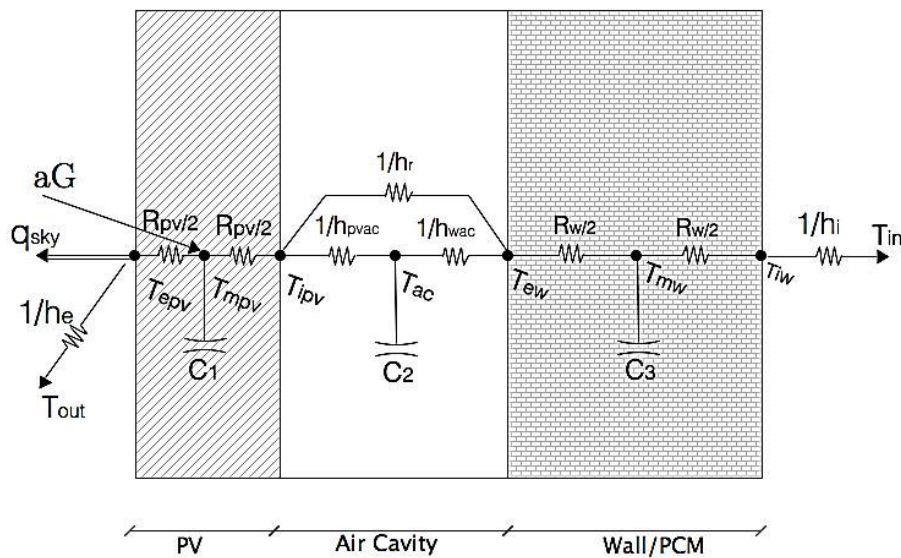


Fig. 4.3. Model studied – Thermal network [37]

4.2.1. Heat Transfer Coefficients

Heat transfer coefficients can be derived analytically through various types of analysis, but these analytic approaches may not offer practical solutions to all problems. As such, many correlations were developed by various authors to estimate the heat transfer coefficients.

In the present work, convective and radiative heat transfer coefficients studied by other authors are used due to the similarity of the studied system.

4.2.1.1. Exterior convective heat transfer coefficient - h_e

Heat loss to the surroundings has been tested by Candanedo et al. [65] using many different approaches. The exterior convective heat transfer correlation was developed by Test et al., [66] for

flat-plate collectors and they are preferable to other formulas, as confirmed by the experimental observations mentioned in the paper by Candanedo et al. [65]. This model resembles a vertical flat-plate collector, so that the following exterior convective heat transfer coefficient is used:

$$h_e = 8.55 + 2.56V_{wind} \quad (4.5)$$

4.2.1.2. Air cavity convective heat transfer coefficients - h_c

Heat transfer inside air cavity has several particularities due to the asymmetric heating (heat transfer occurs mainly through one side of the air channel) and the more complex geometry. However, most researchers have used Nusselt number correlations developed for ducts and vertical collectors with uniform boundary conditions for a given cross section.

In open cavities, the energy added to the room will be expressed by equation (3.25). Air may circulate by either natural or forced convection, and in either case it is necessary to estimate convection coefficients.

The rate of heat transfer between two plates is of obvious importance to the performance of such systems. According to the equation (3.13), Nusselt number correlations are presented for **non-ventilated** (closed) and **ventilated** (open) cavities. The ventilated configuration can be either **natural or forced** ventilation and have laminar or turbulent flow. Reynolds (Re) number characterizes the type of flow. For $Re < 2300$ the flow is considered laminar, transitional flow when $2300 < Re < 4000$, and for $4000 < Re$ the is considered turbulent flow [67]. For low air velocity's, within cavity, like the one experimented in this work (0.035 m/s), the Re number assumes a value under 2300, and the flow is considered as laminar. For higher air velocity's, within cavity, Re number assumes a value above 4000 at the very top of the air channel. For simplification, the turbulent flow near the air cavity exit is neglected and the air flow within the cavity is considered purely laminar.

Closed Cavity (Non-Ventilated)

In closed air cavities (non-ventilated), the heat transfer coefficient is calculated by solving natural convection problems for vertical collectors. The Nusselt correlation given by Shewen [68] for vertical collectors is:

$$Nu = \left[1 + \left(\frac{0.0665 Ra^{0.333}}{1 + (9600 / Ra)^{0.25}} \right)^2 \right]^{0.5} \quad (4.6)$$

where Nu is the Nusselt number and R_a is the Rayleigh number.

From equation (4.6) for vertical collectors and from the equation (3.13), the used convection heat transfer coefficient within a closed air cavity is expressed by:

$$h_c = h_{pvac} = h_{wac} = \frac{k_f}{\ell} \left[1 + \left(\frac{0.0665 Ra^{0.333}}{1 + (9600 / Ra)^{0.25}} \right)^2 \right]^{0.5} \quad (4.7)$$

Open Cavity (Natural-Ventilated)

In the case of open cavities (ventilated), and in the case of natural ventilation, Hollands et al. [69] give the relationship between the Nusselt number and Rayleigh number for a system like the one used in the present work:

$$Nu = 1 + 1.44 \left[1 - \frac{1708 (\sin 1.8\beta)^{1.6}}{Ra \cos \beta} \right] \left[1 - \frac{1708}{Ra \cos \beta} \right]^+ + \left[\left(\frac{Ra \cos \beta}{5830} \right)^{1/3} - 1 \right]^+ \quad (4.8)$$

where the meaning of the + exponent is that only positive values of the terms in the square brackets are to be used (i.e. zero if the term is negative).

From equation (4.8) for open air cavities with natural ventilation and from the equation (3.13), the calculated natural convection heat transfer coefficient within air cavity is expressed by:

$$h_c = h_{pvac} = h_{wac} = \frac{k_f}{\ell} \left[1 + 1.44 \left[1 - \frac{1708 (\sin 1.8\beta)^{1.6}}{Ra \cos \beta} \right] \left[1 - \frac{1708}{Ra \cos \beta} \right]^+ + \left[\left(\frac{Ra \cos \beta}{5830} \right)^{1/3} - 1 \right]^+ \right] \quad (4.9)$$

Open Cavity (Forced-Ventilated)

In the case of opened vertical cavities, mechanically ventilated (forced convection), the following correlation is used [56,70]:

$$Nu = 4.9 + \frac{0.0606 (RePrD_h / \ell)^{1.2}}{1 + 0.0909 (RePrD_h / \ell)^{0.7} Pr^{0.17}} \quad (4.10)$$

where Pr is the Prandtl number, ℓ the length (m), and D_h is the hydraulic diameter (m). This Nusselt number correlation was studied and tested by Candanedo et al. [70] for forced convection asymmetric heating.

Similarly, from equation (4.10) for open air cavities with forced ventilation and from the equation (3.13) the applied natural convection heat transfer coefficient within air cavity is expressed by

$$h_c = h_{pvac} = h_{wac} = \frac{k_f}{\ell} \left(4.9 + \frac{0.0606(RePrD_h/\ell)^{1.2}}{1 + 0.0909(RePrD_h/\ell)^{0.7} Pr^{0.17}} \right) \quad (4.11)$$

4.2.1.3. Room convective heat transfer coefficient - h_i

For the interior room convective heat transfer coefficient (h_i), the one used by Santos [71] was taken as reference value for the horizontal heat flow:

$$h_i = 1/0.13 \left[W/m^2 \cdot ^\circ C \right] \quad (4.12)$$

4.2.1.4. Air cavity radiative heat transfer coefficients - h_r

The exchanges of long-wave thermal radiation between two or more surfaces (which are those of most practical interest because they are associated with the energy balances of the elements' faces' nodes) are a function (the fourth power) of its absolute temperature and surface emittance. They also depend on the geometric relationship between them, described by a dimensionless parameter called a view factor. The view factor between two surfaces can be defined as the fraction of radiant energy emitted by one of them (used as reference), which emits directly to other, which excludes all energy that is transferred by reflection or re-radiation from other surfaces.

In this case, and where the view factor (F_R) for two infinite parallel surfaces is taken to be 1, it is given by:

$$h_r = \frac{F_{R_{pv-pcm}} \cdot \sigma (T_{pv} + T_{pcm}) (T_{pv}^2 + T_{pcm}^2)}{\frac{1}{\varepsilon_{pv}} + \frac{1}{\varepsilon_{pcm}} - 1} \quad (4.13)$$

4.2.2. Thermal Model

Heat transfer across PV module

In this type of thermal analysis, the PV module acts as an opaque surface. As such, the energy balance equations for its surfaces and for the module thermal capacitance necessarily depend on convective and radiative fluxes from outside, from the conduction flux across the panel, and from convective and radiative fluxes to the air cavity.

The surface energy balance equation for T_{epv} node (Fig. 4.3) depends on the heat fluxes between the neighbouring nodes - corresponding to the T_{mpv} node and the outside environment:

$$-\frac{(T_{epv} - T_{mpv})}{R_{pv} / 2} - \varepsilon_{pv} \cdot \sigma \cdot A (T_{epv}^4 - T_{sky}^4) - h_e A (T_{epv} - T_e) = 0 \quad (4.14)$$

where different properties and variables retain the definitions already presented, and T_{epv} is the exterior surface temperature (K), T_{mpv} is the temperature corresponding to the PV thermal capacitance node (K), R_{pv} is the material (PV) conductive resistor (K/W), ε_{pv} is the material (PV) emissivity, σ is the Stefan-Boltzmann constant ($\text{W}/\text{m}^2 \cdot \text{K}^4$), A is the surface area (m^2), T_{sky} is the sky temperature for radiation exchanges (K), h_e is the convective exterior heat transfer coefficient ($\text{W}/(\text{m}^2 \cdot \text{K})$) (Eq.(4.5)) and T_e is the ambient temperature (K).

The volumetric energy balance equation for T_{mpv} node (Fig. 4.3) depends on the conductive heat fluxes through the material. Solar irradiance is applied to this node because it represents the thermal capacitance of the PV module.

$$M_{pv} \cdot C_{pv} \cdot \frac{dT_{mpv}}{dt} = \alpha_{pv} \cdot G + \frac{(T_{epv} - T_{mpv})}{R_{pv} / 2} - \frac{(T_{mpv} - T_{ipv})}{R_{pv} / 2} \quad (4.15)$$

where different properties and variables retain the definitions already presented and, T_{ipv} is the PV interior surface temperature (K), M_{pv} is the PV mass (kg), C_{pv} is the PV specific heat ($\text{J}/\text{kg} \cdot \text{K}$), t is the time (s), α_{pv} is the PV absorptance and G is the solar irradiance (W/m^2).

For node T_{ipv} (Fig. 4.3), the surface energy balance equation depends on the conductive flux from the PV surface, convective flux between the PV surface and air inside the cavity and the radiation flux exchange between the PV and the other surface.

$$\frac{(T_{mpv} - T_{ipv})}{R_{pv} / 2} - h_{pvac} A (T_{ipv} - T_{ac}) - h_r A (T_{ipv}^4 - T_{ew}^4) = 0 \quad (4.16)$$

where different properties and variables retain the definitions already presented, and h_{pvac} is the convective heat transfer coefficient between the PV surface and air cavity ($W/(m^2.K)$) (Eq.(4.7) to Eq.(4.11)), h_r is the radiative interior heat transfer coefficient ($W/(m^2.K)$) (Eq.(4.13)), A is the surface area (m^2), T_{ew} is the wall exterior surface temperature (K), and T_{ac} is the air temperature within the cavity (K).

Heat transfer within the air gap

The air cavity node (T_{ac}) volumetric energy balance depends on superficial convective heat exchanges between the two surface nodes (T_{ipv} and T_{ew}) and the air cavity node (T_{ac}), and from air-air convection with enthalpy transportation (Sub-Chapter 3.4). When the vents are closed, air flow (\dot{m}) becomes equal to zero and there is no enthalpy transportation.

$$M_{air} \cdot C_{p_{air}} \cdot \frac{dT_{ac}}{dt} = h_{pvac} A (T_{ipv} - T_{ac}) + h_{wac} A (T_{ac} - T_{ew}) + \dot{m} C_{p_{air}} (T_{inlet} - T_{outlet}) \quad (4.17)$$

where different properties and variables retain the definitions already presented, and M_{air} is the air mass (kg), C_{air} is the air specific heat ($J/kg.K$), t is the time (s), A is the surface area (m^2), h_{wac} is the convective heat transfer coefficient between the wall and air cavity ($W/(m^2.K)$) (Eq.(4.7) to Eq.(4.11)), \dot{m} is the air mass flow into the air cavity (Kg/s), T_{inlet} is the inlet air temperature (K) and T_{outlet} is the outlet air temperature (K).

Heat transfer across PCM gypsum board

Like the PV module, the PCM gypsum board is also an opaque layer. The surface energy balance equation for T_{ew} node depends on convection between the air inside the cavity and the radiation flux exchange between the wall and the other surface.

$$h_r A (T_{ipv}^4 - T_{ew}^4) - h_{wac} A (T_{ac} - T_{ew}) - \frac{(T_{ew} - T_{mw})}{R_w / 2} = 0 \quad (4.18)$$

where different properties and variables retain the definitions already presented, and T_{mw} is the temperature corresponding to the PCM gypsum board thermal capacitance node (K) and R_w is the material (PCM gypsum board) conductive resistor.

The volumetric energy balance equation for T_{mw} node (Fig. 4.3) depends on the conductive heat fluxes through the material. In the particular case of integrated PCM gypsum board, and following the Athienitis approach mentioned in sub-section, the energy balance for this node also depends on the internal heat generation q_l (W) (Eq. (4.4)).

$$M_w \cdot C_{p_w} \cdot \frac{dT_{mw}}{dt} = \frac{(T_{ew} - T_{mw})}{R_w / 2} - \frac{(T_{mw} - T_{iw})}{R_w / 2} + q_l \quad (4.19)$$

where different properties and variables retain the definitions already presented, and T_{iw} is the wall interior surface temperature (K).

The surface energy balance equation for T_{iw} node (Fig. 4.3) depends on

$$\frac{(T_{mw} - T_{iw})}{R_w / 2} - h_i A (T_{iw} - T_{in}) = 0 \quad (4.20)$$

where different properties and variables retain the definitions already presented, T_{in} is the room temperature (K) and h_i is the convective heat transfer coefficient between the interior wall surface and the room (W/(m².K)) (Eq.(4.12))

4.2.3. Electrical Model for PV Module

The five parameters model of the PV cell [72] is given by:

$$I = I_S - I_0 \left(e^{\frac{V + I R_S}{m V_T}} - 1 \right) - \frac{V + I R_S}{R_p} \quad (4.21)$$

where $V_T = kT/q$.

This cell is represented by an equivalent circuit which consists of a current-controlled generator, a single diode, a shunt and series resistance and is also suitable for a set of identical cells series- or parallel-connected, if all cells are submitted to the same solar irradiance. The electrical equivalent circuit is shown in Fig. 4.4 [73].

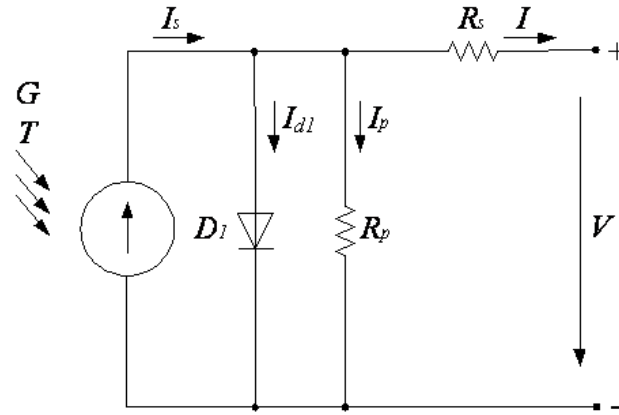


Fig. 4.4. PV equivalent circuit [73]

where G is the solar irradiance, I_s is the photo-generated electrical current, I_d is the current at diode D_1 , I_p is the leakage current, R_p is the equivalent shunt resistance, R_s is the series resistance, I_0 is diode reverse bias saturation current, I is the output current and V is the output voltage.

The model in (4.21) is given by an implicit function that has to be solved by an iterative method to determine, for instance, the output current as a function of the output voltage. From (4.21), considering the short-circuit condition, the photo-generated electrical current is given by:

$$I_s = \frac{I_{SC}(R_s + R_p)}{R_p} + I_0(e^{\frac{I_{SC}R_s}{mV_T}} - 1) \quad (4.22)$$

The second term of (4.22) can be neglected. Hence, the photo-generated electrical current can be approximated by the expression given by:

$$I_s = \frac{I_{SC}(R_s + R_p)}{R_p} \quad (4.23)$$

4.3. SYSTEM PERFORMANCE

The overall system performance was evaluated for of total system efficiency (η_0) which is the sum of the thermal efficiency (η_t) and the electrical efficiency (η_e) [14]:

$$\eta_0 = \eta_t + \eta_e \quad (4.24)$$

There are two approaches to thermal efficiency (η_t) depending on the purpose in summer (η_{ts}) or winter (η_{tw}). In winter, the purpose of the system is to recover and transfer the heat generated by the PV into the room. In summer, the aim is to cool down the PV module and decrease the heat transfer from the outside into the room.

$$\begin{aligned} \eta_t &= \eta_{tw} \quad (\text{winter}) \\ \eta_t &= \eta_{ts} \quad (\text{summer}) \end{aligned} \quad (4.25)$$

Fig. 4.5 shows a scheme with winter and summer configurations, according to the aim of the efficiency calculation.

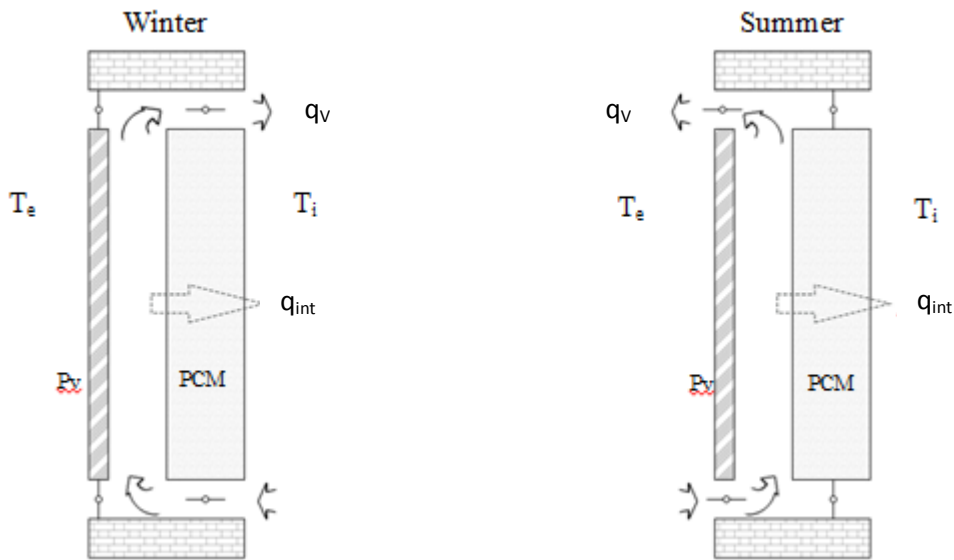


Fig. 4.5. winter (left) and summer (right) configurations

In the winter scenario, the thermal efficiency (η_{tw}) was calculated as a function of the heat gains in the room divided by the solar radiation (G , W/m^2), multiplied by the area of the control volume (A , m^2). In ventilated cases the gain in the room is considered as the sum of the heat rate through the wall (q_{int} , W) plus the air flow from the air cavity to the interior room (q_v , W) [28]:

$$\eta_{tw} = \frac{q_{int} + q_v}{G \times A} \quad (4.26)$$

In the summer scenario, the thermal efficiency (η_{ts}) was taken to be a function of the system heat losses, from inside the room to the exterior environment, divided by the solar radiation (G , W/m^2) multiplied by the area of the control volume (A , m^2). In ventilated cases the loss from the system was taken to be the difference of the air flow from the air cavity to the exterior environment (q_v, W) minus the heat rate through the wall (q_{int}, W):

$$\eta_{ts} = \frac{q_v - q_{int}}{G \times A} \quad (4.27)$$

The energy conversion efficiency (η_e) of a solar panel is the percentage of the solar energy to which the panel is exposed that is converted into electrical energy. This is calculated by dividing a panel's power output (P , W) by the total incident solar radiation (G , W/m^2) and the surface area of the solar panel (A , m^2) [14]:

$$\eta_e = \frac{P}{G \times A} \quad (4.28)$$

As already mentioned, when operating solar cells at elevated temperatures, their efficiency is lowered. When the temperature coefficient (β_c) of the PV module is given the following equation can be used to estimate the efficiency according to the cell temperature [67]:

$$\eta_e = \frac{P}{G \times A} \left(1 - \beta_c (T_{mpv} - T_{NOCT}) \right) \quad (4.29)$$

where β_c (K^{-1}) is the temperature coefficient equal to 0.005, and T_{NOCT} is the nominal operating cell temperature (20°).

4.4. IMPLEMENTATION OF THE NUMERICAL MODEL IN MATLAB®

The thermal and electrical models were implemented in Matlab®/Simulink® with the Simscape® toolbox. Simulink® is a block diagram environment for multidomain simulation and model-based design. It supports simulation, automatic code generation, and the continuous testing and verification of embedded systems [74]. Simulink® provides a graphical editor, customizable block

libraries, and solvers for modeling and simulating dynamic systems. It is integrated with Matlab[®], enabling users to incorporate Matlab[®] algorithms into models and export simulation results to Matlab[®] for further analysis.

The Simscape[®] language enables users to add new physical domains and to create physical modeling components and libraries. It is based on the MATLAB programming language, well-known to engineers. Using this object-oriented modeling language, it is possible to define custom components, complete with parameterization, physical connections, and equations represented as causal implicit Differential Algebraic Equations (DAEs). It is also possible to use MATLAB to analyze the parameter values, perform preliminary computations, and initialize system variables. The Simulink[®] block and dialog box for the component are automatically created from the Simscape[®] file [75].

Once the physical network diagram is constructed in the diagram editor, the first step implemented by Simscape[®] is to analyze the components in the network and their connections in order to convert it into what is known as a structural model. The structural model is the framework of the physical network. The equations, parameters, and initialization for the components are added to this framework to create a behavioral model of the system. The behavioral model represents the set of DAEs symbolically at the equation level and has all of the information necessary to describe the system. Further steps are required to ensure a robust and quick simulation. The system of equations contained in the behavioral model is analyzed and reduced via symbolic simplification methods. The index of the system of equations is reduced after all possible simplifications have been made. This is done by first identifying the higher index constraint equations and then differentiating these equations in time. With this technique, Simscape[®] can reduce many common classes of index-2 problems to index-1 and index-0 problems. Once the index has been reduced, the resulting system is presented to the integrator as a DAE or ODE, depending on the type of integrator. The integrator integrates the system to generate the simulation results [72].

4.4.1. Heat Transfer in Simscape[®]

Heat transfer by conduction, convection and radiation is in Simscape[®] represented by its “Thermal Elements”. All three elements are bidirectional and they only consider one-dimensional heat transfer. This sub-section presents the principal thermal blocks.

4.4.1.1. Conduction in Simscape®

Heat transfer by conduction in Simscape® is described by the block shown in Fig. 4.6. The conductive heat transfer block represents heat transfer by conduction between two layers of the same material. The transfer is governed by the Fourier law described in equation (3.4):



Fig. 4.6. Simscape® Conductive Heat Transfer block

Convection in Simscape®

Heat transfer by convection in Simscape® is described by the block shown in Fig. 4.7. The convective heat transfer block represents heat transfer by convection between two bodies by means of fluid motion. The transfer is governed by the Newton law described by equation (3.6):



Fig. 4.7. Simscape® Convective Heat Transfer block

Radiation in Simscape

In Simscape® the radiation between objects is represented by the symbol in Fig. 4.8. The radiative heat transfer block represents heat transfer by radiation between two bodies. The transfer is governed by the Stefan-Boltzmann law and is described by equation (3.14).



Fig. 4.8. Simscape® Radiative Heat Transfer block

Custom Component in Simscape®

The domains in Simscape® include several different components for the construction of physical systems, but now and again these are not enough to create the intended system. An

example of this is the modeling of heat transfer with a variable heat transfer coefficient. Modifying the convective heat transfer block code and using an “ssc_build” command, it is possible to build a custom convective heat transfer block with a variable heat transfer coefficient, computed by the equations in 4.2.1 or from the workspace. Fig. 4.9 represents the custom block with the variable heat transfer coefficient port.



Fig. 4.9. Custom Simscape® Convection Heat Transfer block

Thermal mass in Simscape®

The thermal mass block (Fig. 4.10) represents a thermal mass that reflects the ability of a material or a combination of materials to store internal energy. The property is characterized by the mass of the material and its specific heat. The thermal mass is described by equation (3.26):



Fig. 4.10. Simscape® Thermal Mass block

Solar cell in Simscape®

The solar cell block (Fig. 4.11) represents a solar cell current source. The solar cell model includes the following components: solar-induced current, temperature dependence, and thermal port. The cell is governed by the electrical circuit represented by Fig. 4.4, and follows equation (4.21).

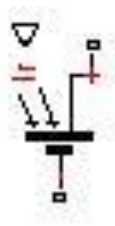


Fig. 4.11. Simscape® Solar Cell block

4.4.2. Constructing the Model

The model is constructed using the blocks described in this section. It is constructed by dividing the system into 1-D layers. Each layer represents a different material and heat transfer between them occurs through the thermal block. The exterior and interior temperatures come from the workspace as well as data from solar irradiance. The air-air convection or enthalpy transport mentioned in sub-section 0 exists in the air cavity and this is added to the model by equation (3.25). The PCM internal heat generation referred to in equation (4.19) is also added to the PCM layer block Fig. 4.12 represents an example of the PV thermal layer block, the PV electrical model block and model first window interface.

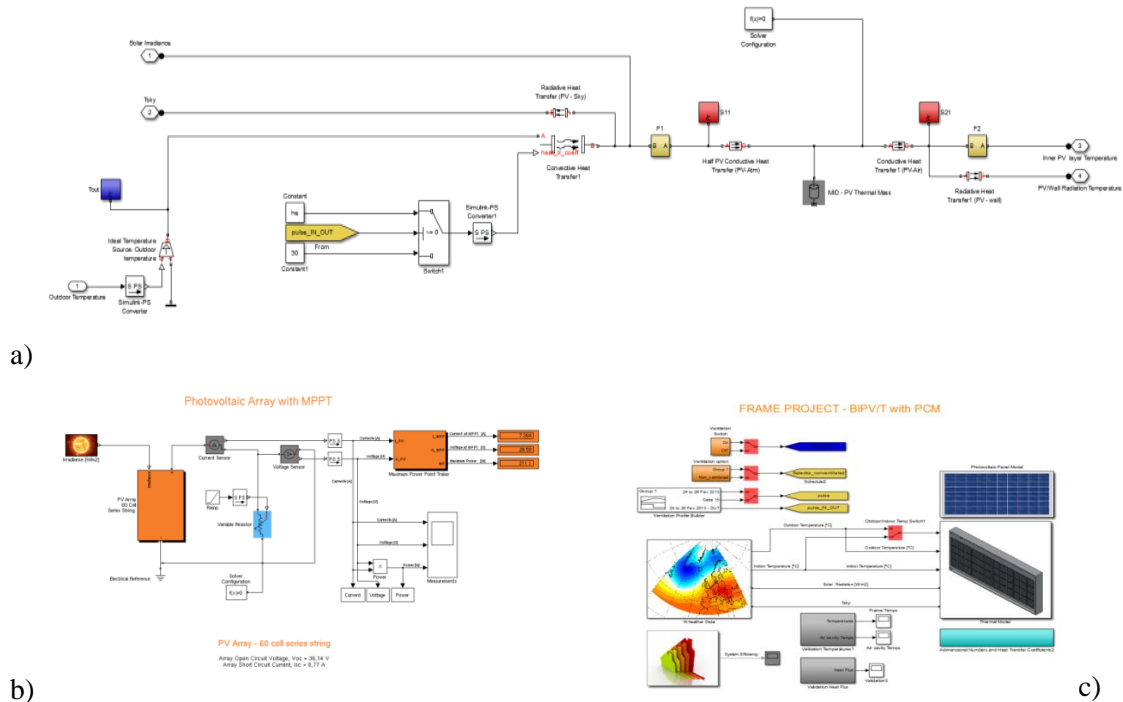


Fig. 4.12. Simscape PV thermal layer block (a), PV electrical model block (b), First window interface (c).

According to the numerical study of this chapter, the results will be analyzed and used to support the design and construction of the prototype. Subsequently the results will be compared and validated.

Chapter 5. EXPERIMENTAL EVALUATION

5.1. INTRODUCTION

As a rule, the objective of experimental work is to understand those physical phenomena that are difficult to predict through simple calculations and to support or validate the results obtained through numerical simulations. In this case, in line with the proposed objectives, was performed the analysis and validation of the results from numerical study carried out in Chapter 4.

To study the influence of some parameters on the thermal behavior and level ventilation of a BIPV/T-PCM system, a prototype was projected, constructed and installed on the SOLAR XXI building, to test different modes of ventilation, radiation levels and environmental conditions. The results from the monitoring system were used afterwards to verify the level of accuracy of the numerical model described in Chapter 4.

This chapter starts with a proposed design. Then it describes the system, the experimental set-up and the instrumentation. The measurement program is then described and some experimental results presented.

5.2. DESIGN PROJECT

By implementing the project and design in 3D software it is possible to build and simulate real-world operating conditions and thus reduce the time and cost of building and testing physical prototypes. SolidWorks® helps ensure that projects are rigorous and efficient in terms of cost, by detecting design errors on the computer screen and not on the factory floor, where changes are more difficult, expensive and time-consuming.

The space for the installation of the prototype was limited so custom components had to be conceived and designed. The frame (Fig. 5.13 (b)) to support the other elements was designed with limited dimensions and the PV module (Fig. 5.13 (a)) had to be customized. The PCM layer (Fig. 5.13 (c)) was designed to maximize the PCM utilization area, and ensure the limits imposed by the local geometry and the need for ventilation. Fig. 5.13 (d) shows the complete assembly of the prototype.

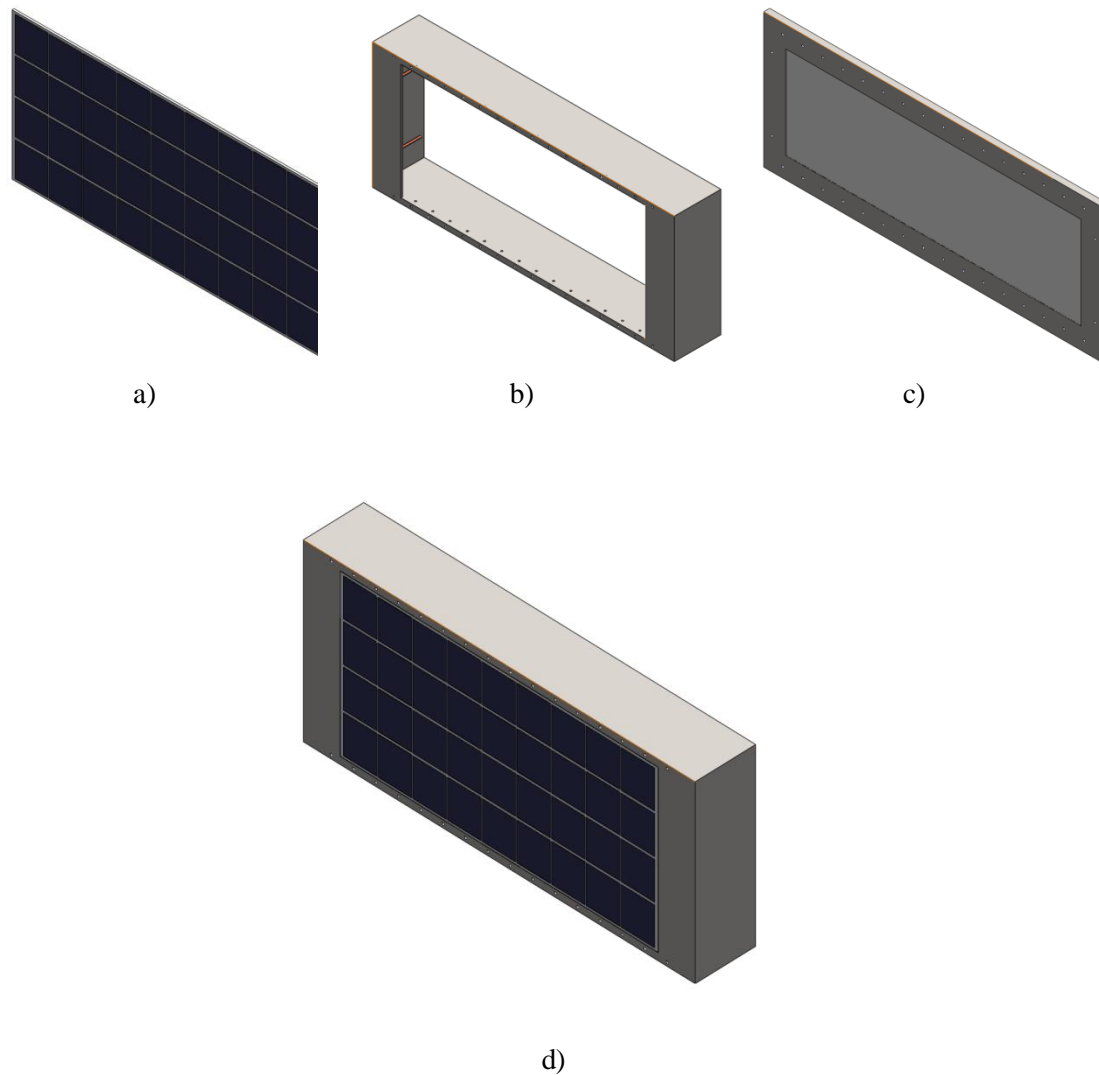


Fig. 5.13. PV module (a), Frame (b), PCM layer (c), Assembly (isometric) (d)

Access to the interior of the prototype was secured by a moving mechanism. Fig. 5.14 (a) shows the back of the prototype where two orientation axes and one knob can be seen. The section view of Fig. 5.14 (b) shows the operation of the PCM layer on axles.

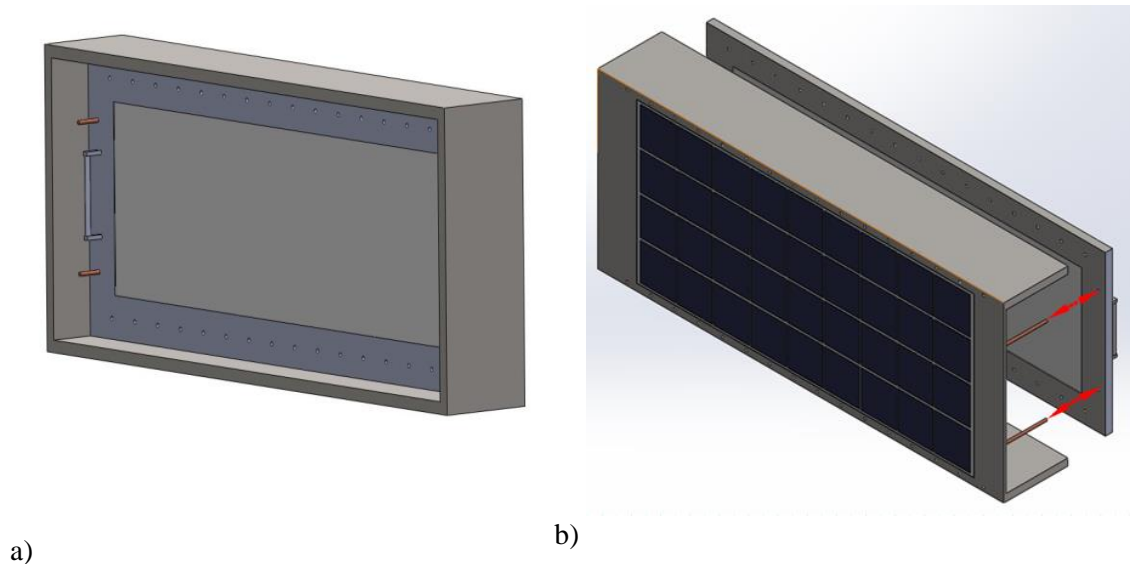


Fig. 5.14. Assembly (back) (a), Section of semi-exploded view (b)

5.3. SYSTEM DESCRIPTION

The prototype was installed on a main facade of Solar XXI, and office building (Fig. 5.1) in Lisbon and has been tested in real conditions since then (Fig. 5.1). The modules consist of an outer layer (PV module) and an inner layer (gypsum wallboard incorporating a PCM). In the case of BIPV/T-PCM (i.e. the module incorporating a PCM in the gypsum board), the PV panels absorb the solar radiation during the day, thereby generating heat during the conversion process; this heat is used to melt the phase change material. At night, the PCM solidifies and delivers heat that keeps the panel warm for a prolonged period of time. The purpose of the BIPV-PCM and the expected behavior is to keep the outside wall temperature warm (over 20°C), to prevent heat loss through the wall. The BIPV-PCM system is designed to be integrated within a building envelope to build up the thermal energy directly in the wall of the building.



Fig. 5.1. Solar XXI building (top), Prototype installed on the Solar XXI main facade (bottom) [37]

The external and internal frame of the prototype has a ventilation system that can provide, if necessary, the ventilation of the inner air gap with interior or exterior environment. The air flow can be controlled by opening or closing the slot openings. The internal layer (plaster PCM board) is movable so that the air gap width can be controlled and its influence on the overall system behavior assessed. Fig. 5.2 gives a cross section view of the system.

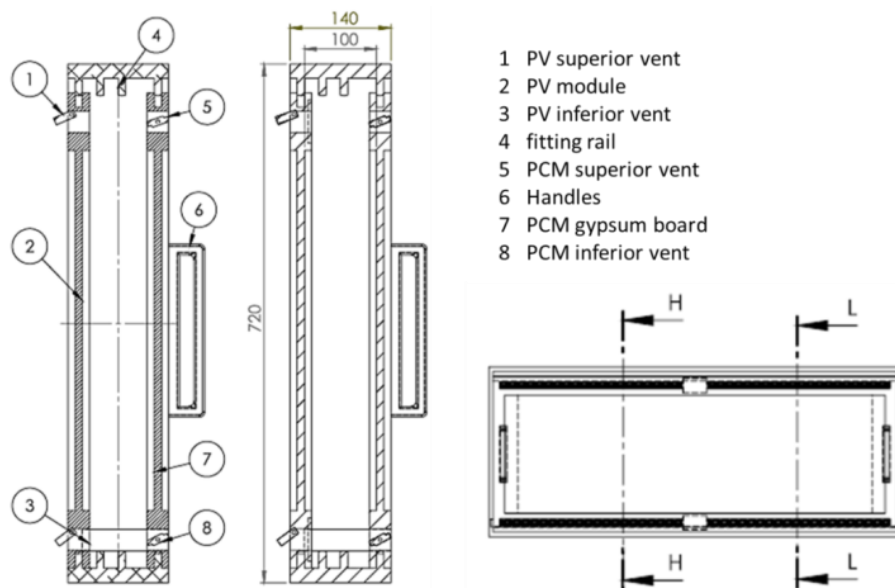


Fig. 5.2. Crosssection of BIPV-PC [35].

The PCM used is incorporated in a gypsum board, namely, Alba@balance plasterboard. The PCM gypsum board is integrated in the BIPV-PCM system adjacent to the interior room. The outer layer of the system is a PV polycrystalline module with a peak power, P_{max} , of about 120 Wp. The air gap formed between two layers (internal-PCM gypsum board and external-PV module) is about 10 cm wide.

The properties of each layer are summarized in Table 5.1.

Table 5.1. Materials properties.

Material	Thickness (L) m	Conductivity (K) $W/m.K$	Specific Heat (C_p) $J/kg.K$	Density (ρ) kg/m^3	Other Properties		
					Short Circuit Current (I_{SC}) A	Open Circuit Voltage (V_{OC}) V	Absorptivity α
PV	0.0038	148	677	2330	7.7	21.8	0.9
Air	0.01	0.0257	1007	1.205	Kinematic Viscosity (ν) m^2/s		Expansion Coefficient (β) $1/K$
					15.11×10^{-6}	3.43×10^{-3}	
PCM	0.025	0.33	1132	1000	Latent Heat (L) J/kgK	Freezing	
					12000	Start (T_1) $^{\circ}C$	End (T_2) $^{\circ}C$
						18	23

5.4. EXPERIMENTAL SET-UP AND INSTRUMENTATION

The installed prototype is completely monitored on all surfaces and in the inner air gap, to understand the thermal behavior of the system. Interior and exterior air temperatures are also monitored, as well as the overall solar radiation. The surface temperature of each layer of the prototype was measured by means of type PT 100 thermal sensors (sub-section 5.4.2) (2mm*2,3mm), with 4 sensors on each surface. At the same time and to give a more accurate surface temperature measure, a Self-Adhesive Patch (sub-section 5.4.2) sensor was used, one on each surface. The heat flux measurements were taken by a Hukseflux sensor HFP01-05 (sub-section 5.4.3). Three PT100 sensors were placed at three different levels inside the air gap, as shown in Fig. 5.3. The exterior and interior ambient temperatures were also measured using PT100 sensors and the solar radiation was measured with a Hukseflux SR11 sensor (sub-section 5.4.3). The map of sensors is presented in Fig. 5.3.

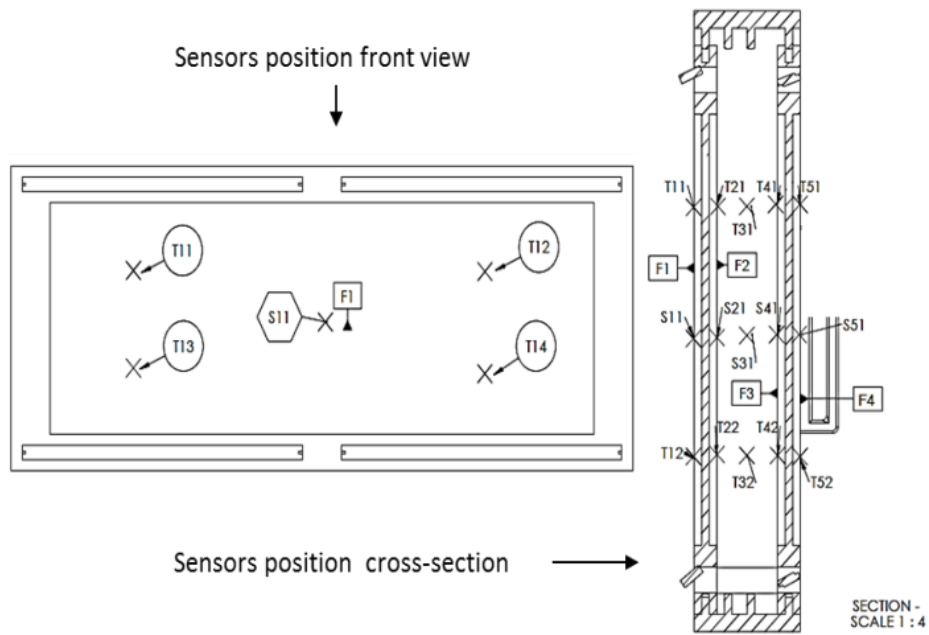


Fig. 5.3. Cross section set-up and sensor positions [37]

Table 5.2 summarizes the sensors used and their locations.

Table 5.2. Sensors identification and positions

PCM surface facing room	PCM surface facing air gap	Air gap between PCM and PV	PV facing air gap	PV outside
PT100 2x2,3mm	PT100 2x2,3mm	PT100 2x2,3mm	PT100 2x2,3mm	PT100 2x2,3mm
T51	T41	T31	T21	T11
T52	T42	T32	T22	T12
T53	T43	T33	T24	T13
T54	T44	T34	T25	T14
Patch PT100	Patch PT100		Patch PT100	Patch PT100
S51	S41		S21	S11
Hukseflux HFP01-05	Hukseflux HFP01-05		Hukseflux HFP01-05	
F5	F4		F2	

In Fig. 5.4 we can see the installation of the temperature sensors and flux meters in the inner layers of the PV module (a) and PCM (b), respectively.



a)

b)

Fig. 5.4. Sensors installed on inner PV layer (a), Sensors installed on inner PCM layer (b)

The need to measure the temperature inside the air cavity at several heights meant that a support structure had to be built for the three air temperature sensors (Fig. 5.5).



Fig. 5.5. Detail of the support structure for the three air temperature sensors

5.4.1. Data Acquisition Logger

The instrumentation was controlled with an Agilent 34970A Data Acquisition / Data Logger Switch Unit Fig. 5.6 (a). The logger consists of a three-slot mainframe with a built-in 6 1/2 digit digital multimeter. Each channel could be configured independently to measure one of 11 different functions without the added cost or hassle of signal-conditioning accessories. There is a choice of

eight optional plug-in modules to create a compact data logger, full-featured data acquisition system or low-cost switching unit. On-module screw-terminal connections eliminate the need for terminal blocks and a unique relay maintenance feature counts every closure on every switch for easy, predictable relay maintenance. The 34970A module features a built-in thermocouple reference and 20 two-wire channels.

Agilent BenchLink Data Logger was the data acquisition software (Fig. 5.6 (c)) and was included with the 34970A. BenchLink Data Logger is a familiar Microsoft® Windows® interface for test configuration and real-time data display and analysis. It is easy to set up and quickly take measurements, export data or use the built-in graphs to log the results. The software is freeware.

The accuracy of the data logger voltage measurement is specified as 0.0041% for normal operating temperature (18°C-28°C), 0.008% at 35°C and 1.4% at 150°C [76].

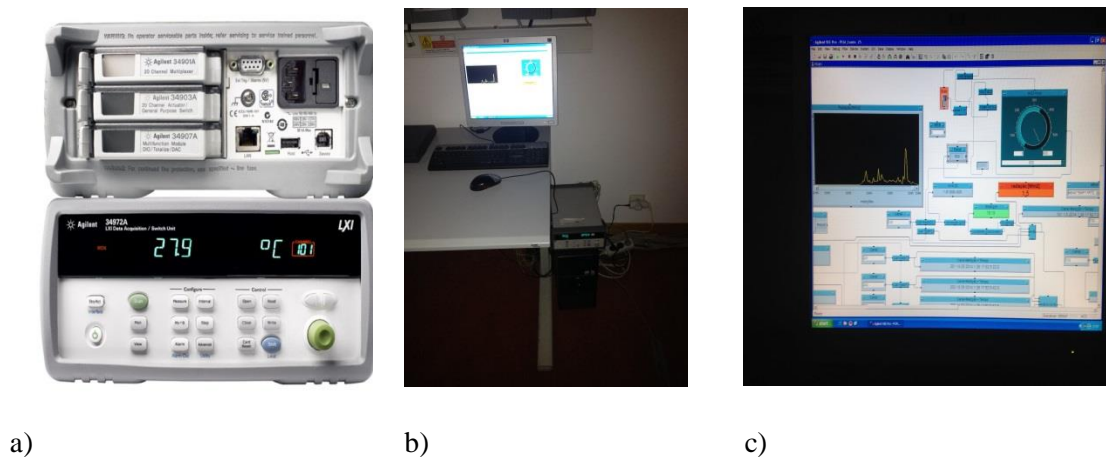


Fig. 5.6. Data Logger (a), Data Acquisition apparatus (b), Data logger acquisition software (c)

5.4.2. Temperature Sensors

The temperature was measured during the experimental work with PT100 sensors (Fig. 5.7 (a)). Inside the air cavity the sensor was left exposed to maintain sensitivity. To measure the surface temperature, a sensor was installed with an aluminium heat shield and insulated on the side exposed to convection and radiation.

This sensor measures the heat resistance temperature by correlating its electrical resistance with temperature. Most of these sensors are made from a coil of thin wire mounted on a ceramic or glass carrier. The element is usually quite fragile so it is often placed inside a sheathed probe to protect it. The resistance temperature detector (RTD) element is made from a pure material, usually platinum, nickel or copper. The PT100 is generally regarded as the most accurate industrial temperature sensor available, and also provides excellent stability and repeatability. The most common devices used in industry have a nominal resistance of 100 ohms at 0 °C, and are

called Pt100 sensors. The PT100s can measure temperatures from -200°C up to 500°C , with $\pm 0.1^{\circ}\text{C}$ accuracy. It can be repeatedly cycled a few hundred degrees and still pass the test of the best stopover resistance. Few materials can be treated in this way and keep stable.

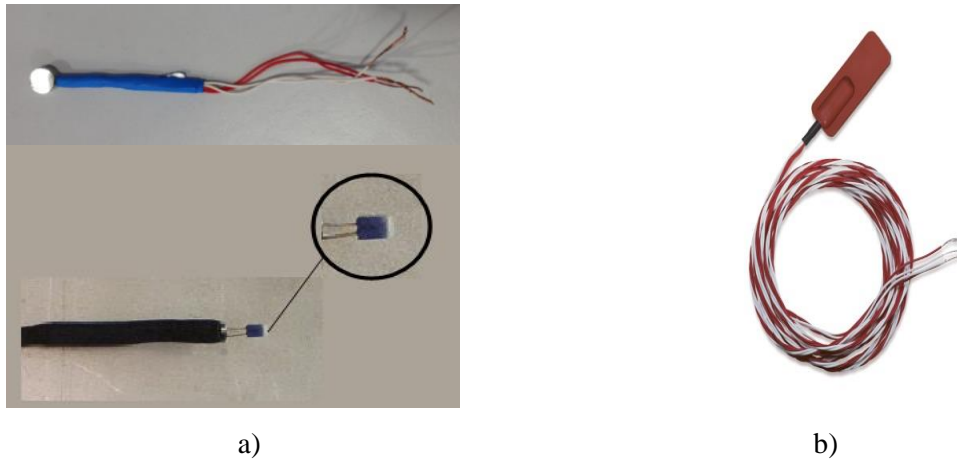


Fig. 5.7. PT 100 sensor (a). PT 100 Self-adhesive sensor (b)

For a more accurate surface temperature measure, the signal converter is housed in silicone rubber under a self-adhesive aluminium film (Fig. 5.7 (b)). After removing the protective film, the sensor can be directly glued to the surface to be monitored.

Fig. 5.8 shows three types of installation for the PT-100 sensors: air exposed, surface application, and self-adhesive.



Fig. 5.8. PT 100 sensor (a), PT 100 Self-adhesive sensor (b)

5.4.3. Fluxmeter Sensors

Heat flux sensor

The heat flux measurements for the experimental work were performed by a Hukseflux HFP01 fluxmeter Fig. 5.9 (a). This sensor measures the heat flux that passes through the object in which it is incorporated or on which it is mounted. The HFP01 uses a thermopile. This thermopile measures the differential temperature across the ceramics-plastic composite body of HFP01. Working in completely passive way, HFP01 generates a small output voltage proportional to the local heat flux.

For the readout, we only need an accurate voltmeter that works in the millivolt range. To calculate the heat flux, the voltage must be divided by the sensitivity; this constant is supplied with each individual instrument.

$$\varphi = V_{sen} / E_{sen} \quad (5.1)$$

where φ is the heat flux (W/m^2), V_{sen} is the measured signal (Volt) and E_{sen} is the conversion factor.

If we measure the heat flux across surface objects whose thermal resistance is comparable to that of the sensor then some corrections are needed to avoid the occurrence of so called “resistance errors”. The following formula was provided by the heat flux sensor’s manufacturer:

$$\varphi = \frac{(R_{thobj} + R_{thsen})V_{sen}}{E_{sen}R_{thobj}} \quad (5.2)$$



a)



b)

Fig. 5.9. Hukseflux HFP01 fluxmeter (a). Hukseflux HFP01 fluxmeter installed at PV interior layer (b)

where ϕ is the heat flux (W/m^2), R_{thobj} is the thermal resistance of the object ($\text{m}^2 \text{K}/\text{W}$), R_{thsen} is the thermal resistance of the sensor ($\text{m}^2 \text{K}/\text{W}$), V_{sen} is the measured voltage (Volt) and E_{sen} is the sensor sensitivity.

Some errors may occur when the sensor is not close to the surrounding material, and the void created between them is filled with air (air conductivity is about ten times smaller than the flux sensor conductivity). To prevent errors of this kind, which are difficult to detect, the sensors were installed on the surface, following the manufacturer's recommendations, i.e. using silicone glue (Fig. 5.9 (b)) (Appendix D).

Table 5.3. Sensitivity calibration constant

Sensor	Sensitivity	Units
7767	62.52	$\mu\text{V}/(\text{Wm}^{-2})$
7768	62.18	$\mu\text{V}/(\text{Wm}^{-2})$
7769	62.5	$\mu\text{V}/(\text{Wm}^{-2})$
7770	62.71	$\mu\text{V}/(\text{Wm}^{-2})$

Pyranometer

The solar radiation was measured by an SR11 pyranometer (Fig. 5.10 (a)). It is a high accuracy solar radiation sensor. The SR11 measures the solar radiation received by a plane surface from a 180° angle of view. This quantity, expressed in W/m^2 , is called "hemispherical" solar irradiance.



a)



b)

Fig. 5.10. Hukseflux SR11 pyranometer (a). SR11 pyranometer installed at PV exterior layer (b)

The SR11 pyranometer can be used outdoors under the sun, as well as indoors with lamp-based solar simulators. Its orientation depends on the application and may be horizontal, tilted (for plane-of-array radiation) or inverted (for reflected radiation). For the experimental work described here, the SR11 pyranometer was installed at a tilted angle of 90° following the vertical surface of

the PV module (Fig. 5.10 (b)). Thus, the radiation measured corresponds to the radiation that reaches the vertical surface of the PV module.

The calibration of this apparatus results in sensitivity uncertainty of 1.8%, compared to typical uncertainty of more than 2.8% for this pyranometer class.

5.4.4. Hotwire Anemometer

The airspeed in the cavity was monitored with a portable logger equipped with a hotwire anemometer (Fig. 5.11). This equipment - Testo 425 – has an air velocity measuring range of 0 - 20 m/s, a precision of $\pm (0.03 \text{ m/s} + 5\% \text{ of m.v.})$ and a resolution 0.01 m/s.

Even though the airspeed was calculated by equation (4.1), a measurement was taken to check the agreement between calculated and measured values. It was not possible to measure the air velocity in the center of the cavity, and it is believed that insufficient information was acquired in this experimental procedure to be used for the same purpose, although the measured values to inlets and outlets of the cavity were very close to the calculated value.

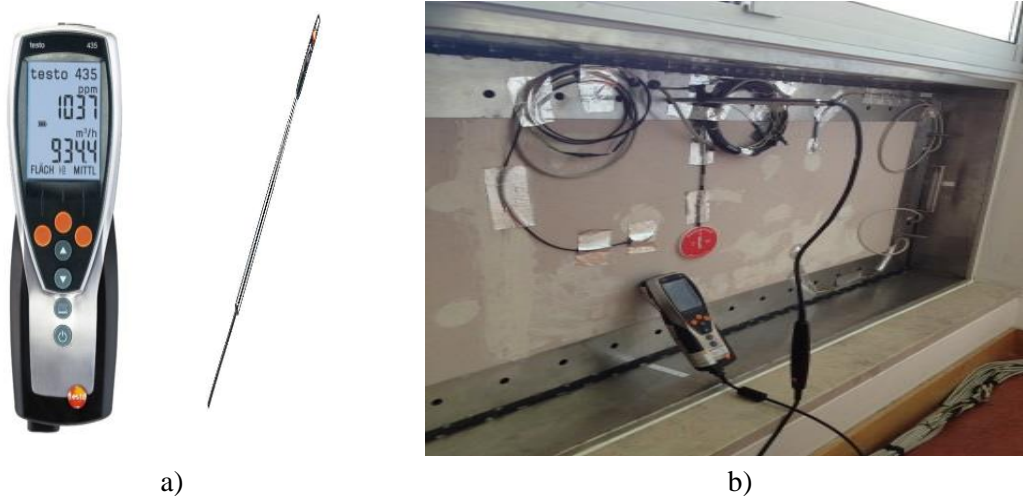


Fig. 5.11. Hotwire anemometer logger (Testo 425) (a). Taking measurement with the hotwire anemometer (b)

5.4.5. Thermal Images

Thermal images were taken to obtain different types of evaluations for the prototype temperature. The images were captured by a Testo Fluke Ti25 camera. The thermal and visual images can be displayed simultaneously as total fusion (thermal overlay visual) or PIP images (Picture-In-Picture). The temperature range of thermal images ranges from -20°C to $+350^{\circ}\text{C}$ in the Ti25. The thermal image can be displayed in various color palettes.



Fig. 5.12. Testo Fluke Ti25 thermal camera

5.5. MEASUREMENT CAMPAIGN AND EXPERIMENTAL RESULTS

To obtain a more detailed analysis of the system, the measurement program was divided into two, a winter and summer program. Two days two days with different radiation and outdoor temperature were chosen in each period. The system was analyzed for surface temperature, taking into account both the indoor and outdoor temperatures and the incident solar radiation. The heat fluxes, airflows and air stratification within the cavity are also shown, along with the system efficiency.

5.5.1. Winter Campaign

The system was installed in January 2013 and the installation of the sensors was concluded in first part of February, enabling the first experimental results to be obtained in the second part of February. Interior and exterior temperatures as well as the solar radiation measurements are presented in Fig. 5.13. We can see that only three days in February were characterized as having sunny winter conditions, the best climatic conditions for the experimental campaign with a clear sky, solar radiation values of almost 900W/m^2 , maximum of outside temperature of about 12°C and the minimum values between 4 to 6°C

For the winter campaign of this experimental work, an analysis of the thermal performance of the BIPV/T-PCM system was proposed for two days with slightly different climatic conditions in order to estimate the behavior of the system, the PCM and inside room temperature for two different outside ambient conditions.

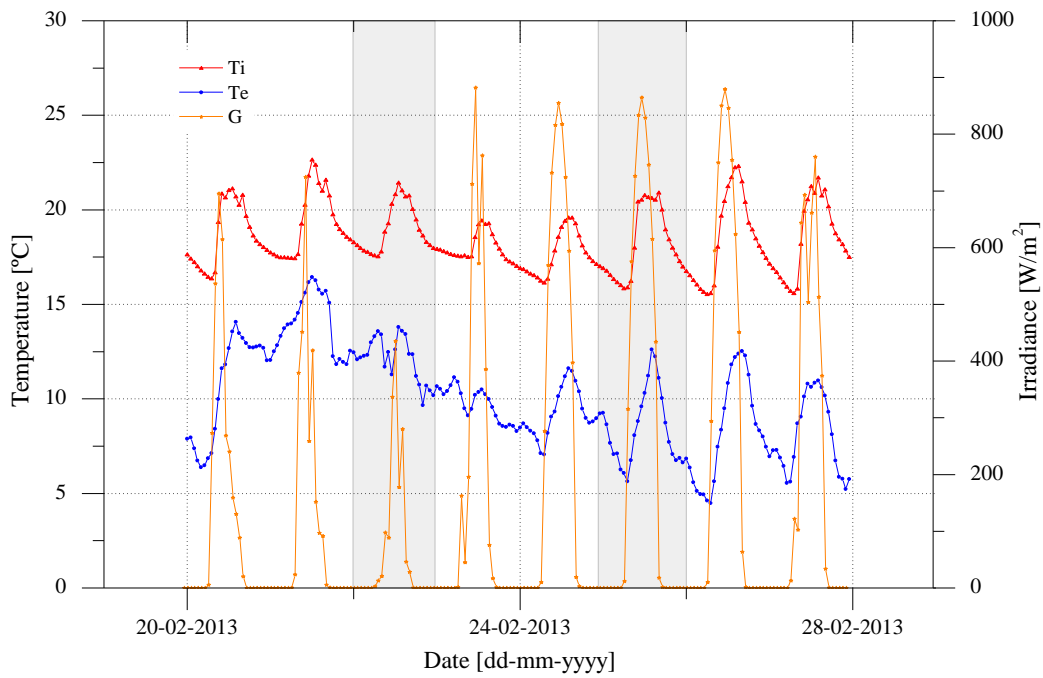


Fig. 5.13. Exterior, interior temperature and solar radiation measurements February 2013 [35]

The 22nd of February had low solar irradiance with big fluctuations during the day, ranging from very low values of about 80 W/m² to highs of 900 W/m². It was a very cloudy day and the maximum outside temperature was around 10°C, as can be seen in Fig. 5.14.

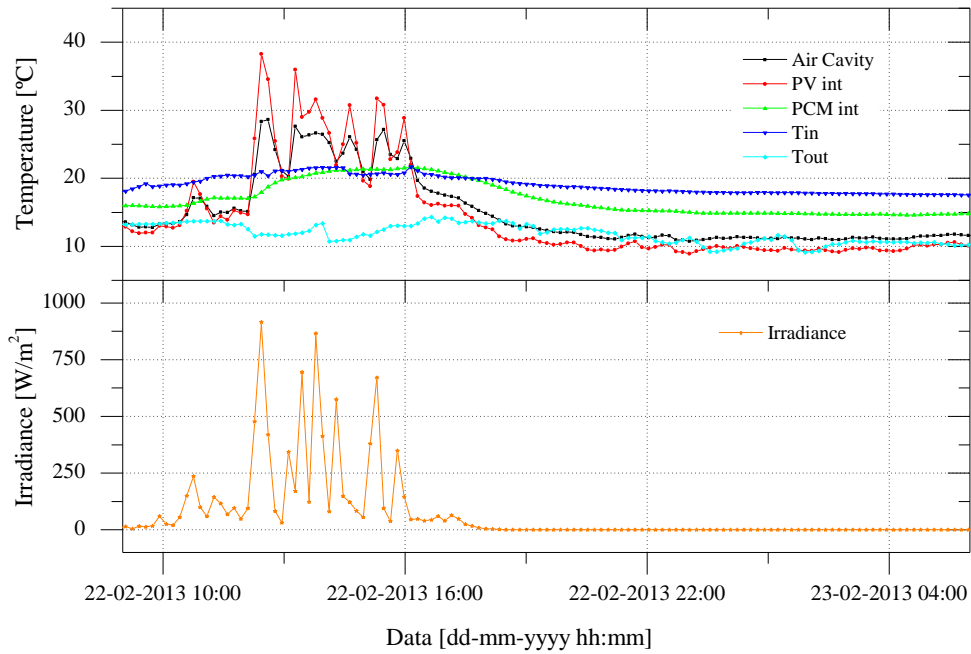


Fig. 5.14. Temperature and irradiance values, 22 February 2013 [35].

All the surface temperatures of the system exhibited a very high variation, especially on the inner part of PV module and the air gap temperature. The air gap temperature was highly influenced by the PV module temperature and exhibits values between 20–25°C in the daytime. The PCM gypsum board, however, has a more “stable” configuration, as expected, with the surface facing the room remaining at about 20°C in the day and 16°C at night. The inside room temperature also has a constant configuration, showing that, even on a cloudy day and with an outside ambient temperature of approximately 11°C, the temperature is around 20°C for most of the day and 18°C at night. It is known that the general behavior of the room is influenced by other factors and the building itself. Even so, the PCM gypsum board surface temperature shows that there is no heat loss through the BIPV/T-PCM system

Looking at and Fig. 5.15 and Table 5.4, we can see the temperatures profiles through the system cross section at certain times on 22 February.

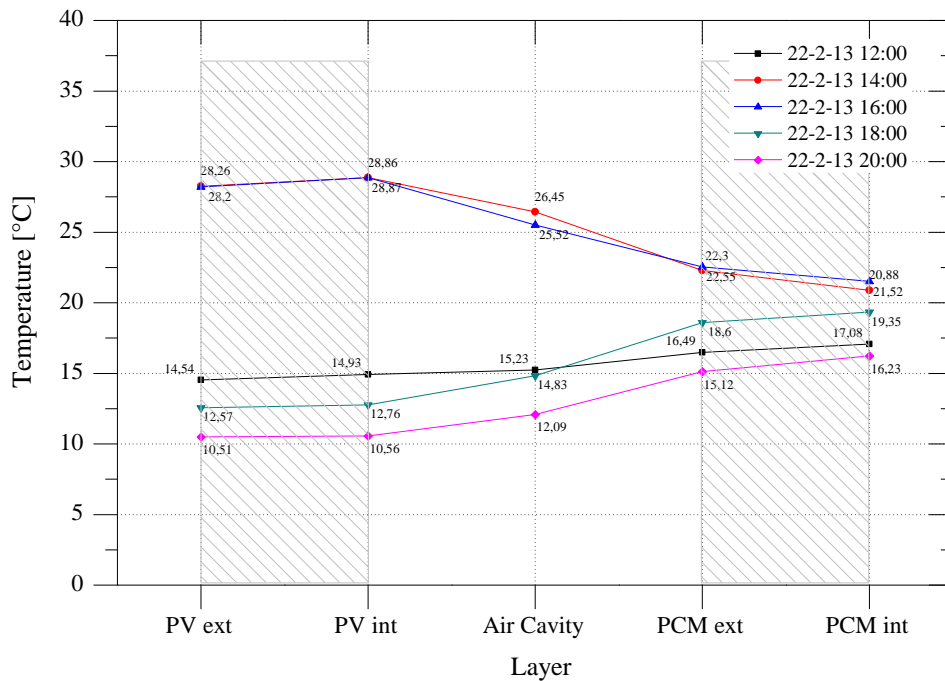


Fig. 5.15. Cross section temperatures at different times, 22 February 2013 [35].

It is noticeable that the greatest temperature differences at different times of the day are shown by the PV module, with a difference of about 18°C between the temperature at 14:00 and 20:00, and the smaller ones are shown by the PCM and are about 4°C from 12:00 to 20:00.

Table 5.4. Cross section temperatures at different times, 22 February 2013

Layer	Temperature [°C] for 22-02-2013				
	12:00	14:00	16:00	18:00	20:00
PV ext	14.54	28.26	28.2	12.57	10.51
PV int	14.93	28.86	28.87	12.76	10.56
Air Cavity	15.23	26.45	25.52	14.83	12.09
PCM ext	16.49	22.30	22.55	18.60	15.12
PCM int	17.08	20.88	21.52	19.35	16.23

Looking at the heat flux in the PCM layers in Fig. 5.16, we can see how this kind of material can regulate it. The fluxmeters located on the outer layer of the PCM (F4 – PCM ext) record a flux with a maximum of around 120 W/m^2 near noon. The sensor on the inner layer of the PCM shows a smoothing and lowering of the transmitted flux levels. This phenomenon is due to the absorption of energy by the PCM in the form of latent heat.

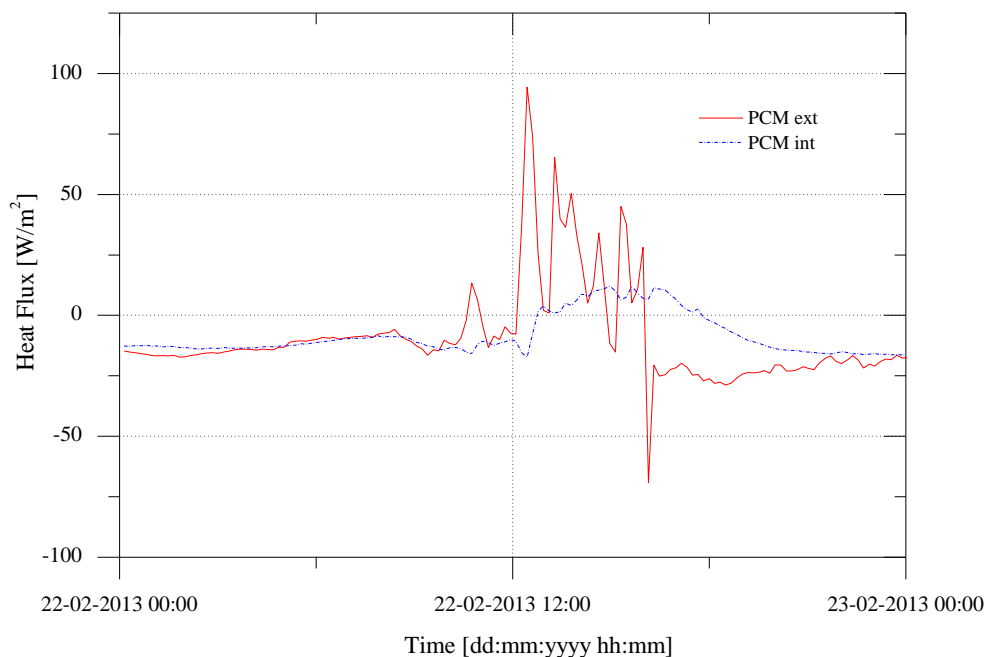


Fig. 5.16. Heat flux through PCM surfaces 22 February 2013.

Now looking at the experimental data measured on 25 February 2013, it can be seen that the outside ambient temperatures are different (Fig. 5.17). It was a very sunny day with irradiance values reaching 900 W/m^2 , and an outside temperature of about 10°C . The thermal behavior of the BIPV/T-PCM showed a more regular path than the results from 22 February. In this case the PV module reached a maximum temperature of 58°C in the peak hour of the day (between 12h and 15h), the air gap had a maximum temperature of 48°C , the PCM gypsum board a maximum temperature of 29°C and the inside room temperature kept a fairly constant temperature of 20°C .

The temperature profiles of the PV module and air gap show a more dynamic behavior, a higher difference between the maximum and minimum values, which were 56°C for the PV module and 45°C for the air gap. The profiles of the PCM layer and the inside room temperature are more constant, with a temperature difference between maximum and minimum values of about 18°C for the PCM and 5°C for the inside room temperature

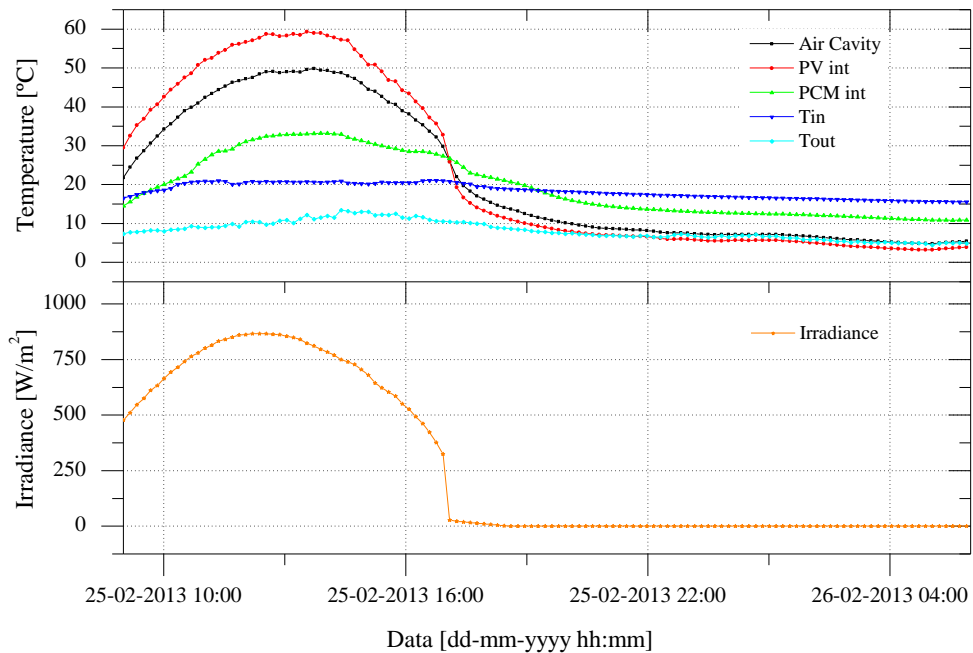


Fig. 5.17. Temperature and irradiation values, 25 February 2013 [35]

Table 5.5 and Fig. 5.18 present the cross section temperatures for 25 February 2013. The temperature profiles show a quite similar path compare with those from 22 February. The PV module and the air gap exhibit higher temperature differences at different times of the day, while the PCM again has a smaller difference in temperature at different times of the day.

Table 5.5. Cross section temperatures at different times, 25 February 2013

Layer	Temperature [°C] for 25-02-2013				
	12:00	14:00	16:00	18:00	20:00
PV ext	54.82	57.23	42.22	11.61	7.11
PV int	56.15	59.02	44.24	13.27	8.11
Air Cavity	46.68	49.44	39.01	16.24	10.15
PCM ext	36.50	40.63	34.35	21.68	14.93
PCM int	30.30	33.19	28.85	22.14	16.32

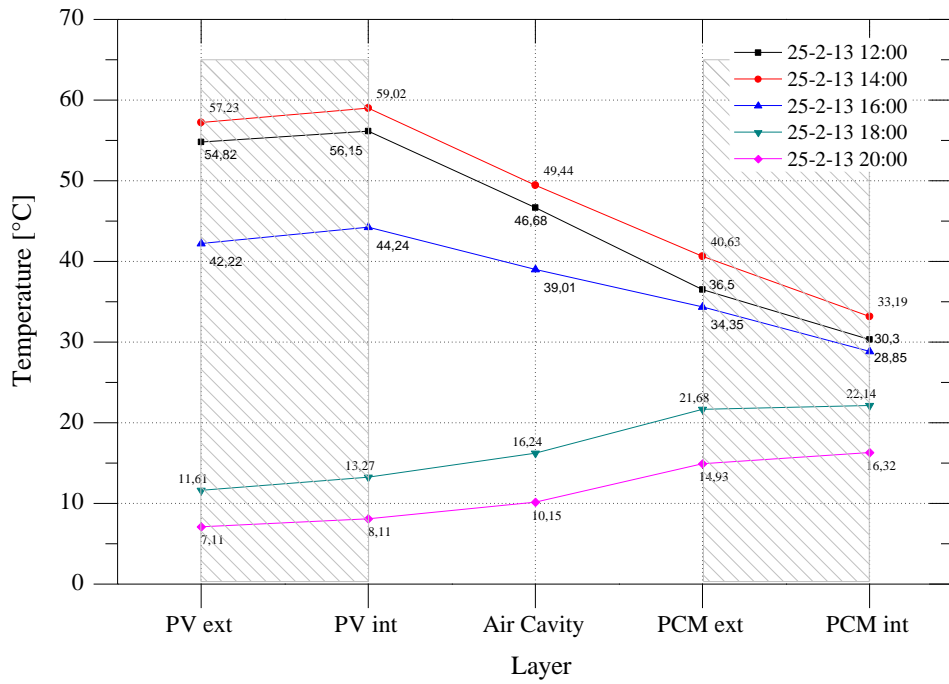


Fig. 5.18. Cross section temperatures at different times, 25 February 2013 [35]

Like Fig. 5.16, Fig. 5.19 also shows the heat flux in the PCM layers of the system. On a sunny day such as this, the reduction of the heat flux values is not evident, but a lag is visible with respect to time. As with irregular climatic conditions days (Fig. 5.16), this phenomenon is also justified by the absorption of energy in the form of latent heat.

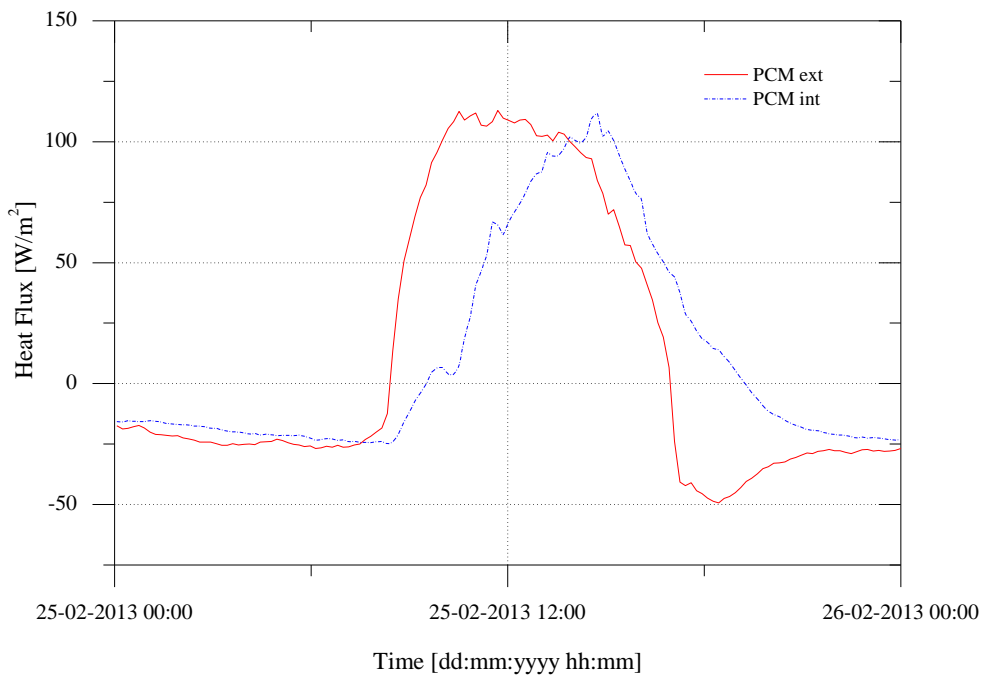


Fig. 5.19. Heat flux through surfaces, 25 February 2013

5.5.2. Summer Campaign

Like the winter campaign, an analysis of thermal performance for two days with different climatic conditions was proposed for the summer program, in order to estimate the behavior of the system.

Two different months had to be observed to obtain two summer days with different climatic conditions.

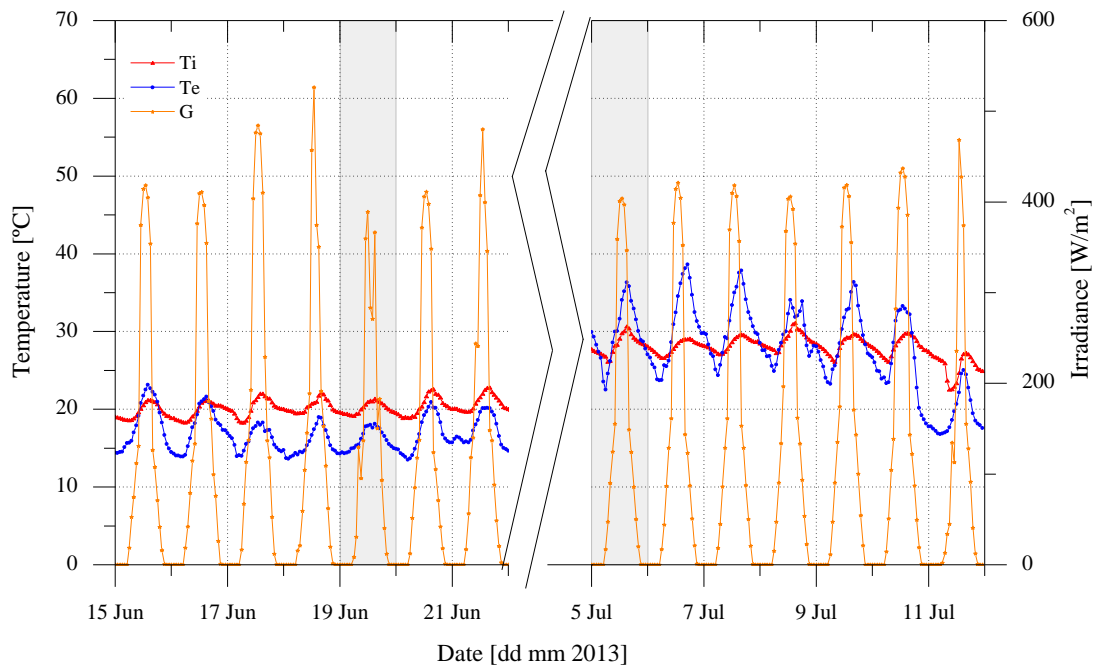


Fig. 5.20. Exterior, interior temperature and solar radiation measurements, June and July 2013

June (Fig. 5.20) presents the early summer conditions, with radiation in the vertical plane not exceeding 550 W/m^2 . Outdoor and indoor temperatures have similar values, without major fluctuations. The outdoor temperature has a range between 14°C and 22°C , while indoor temperatures fluctuate between 18°C and 22°C .

The month of July (Fig. 5.20) has plenty of days with sunny conditions, with radiation in the vertical plane not exceeding 450 W/m^2 and the maximum outside temperature around 38°C and the minimum 23°C , while indoor temperatures fluctuate between 26°C and 31°C .

The 5th of July is a typical summer day with radiation that rises suddenly from about 50 W/m^2 to 450 W/m^2 during the day. The outside temperature on this sunny day had a significant oscillation between 23°C and 38°C , while the inside room temperature was more or less constant, with values of 20°C for the daytime and 18°C during the night. The temperature profile of the PV module and the air gap exhibits a regular behavior with a high difference of about 8°C between them. In these climatic conditions, it can be seen that the temperature profile (PV module and air

gap) is committed to a behavior that reacts to radiation and outside temperature without being able to individually highlight either. This means that the radiation has a maximum value of about 400 W/m² at 13:00, and the maximum value of about 37°C for outside temperature occurs at around 15:00, whereas the temperature profile maximum occurs at 14:00. With this high temperature profile for the PV module and the air gap, it is normal to have the PCM layer behavior close to the outside temperature profile.

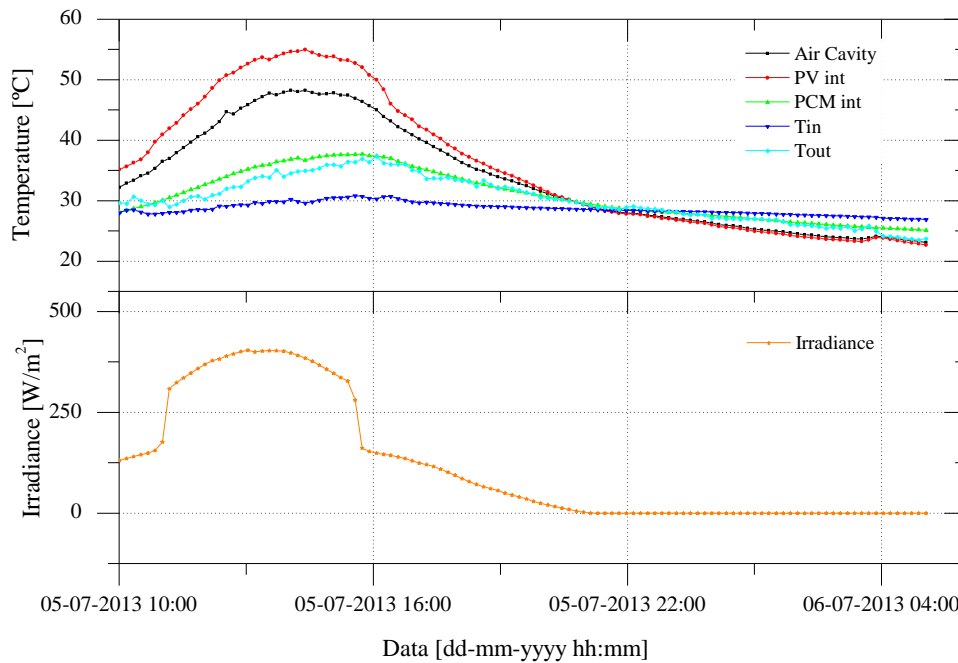


Fig. 5.21. Temperature and irradiation values, 5 July 2013

Table 5.6 and Fig. 5.22 show the cross section temperatures at different times for 5 July 2013. Comparing the two summer and winter sunny days (Fig. 5.18 and Fig. 5.22), there is a smaller range of system temperatures for summer days as well as minimum temperatures of the PV module. This is explained by the high outdoor temperature but low incident radiation on the vertical plane, which is typical of summer days.

Table 5.6. Cross section temperatures at different hours, 5 June 2013

Layer	Temperature [°C] for 05-02-2013				
	12:00	14:00	16:00	18:00	20:00
PV ext	52.44	56.68	46.47	36.12	30.08
PV int	49.93	54.45	46.13	36.36	30.37
Air Cavity	43.45	47.96	42.81	35.08	30.25
PCM ext	37.21	41.73	39.86	34.24	30.57
PCM int	33.77	37.07	36.65	32.84	30.13

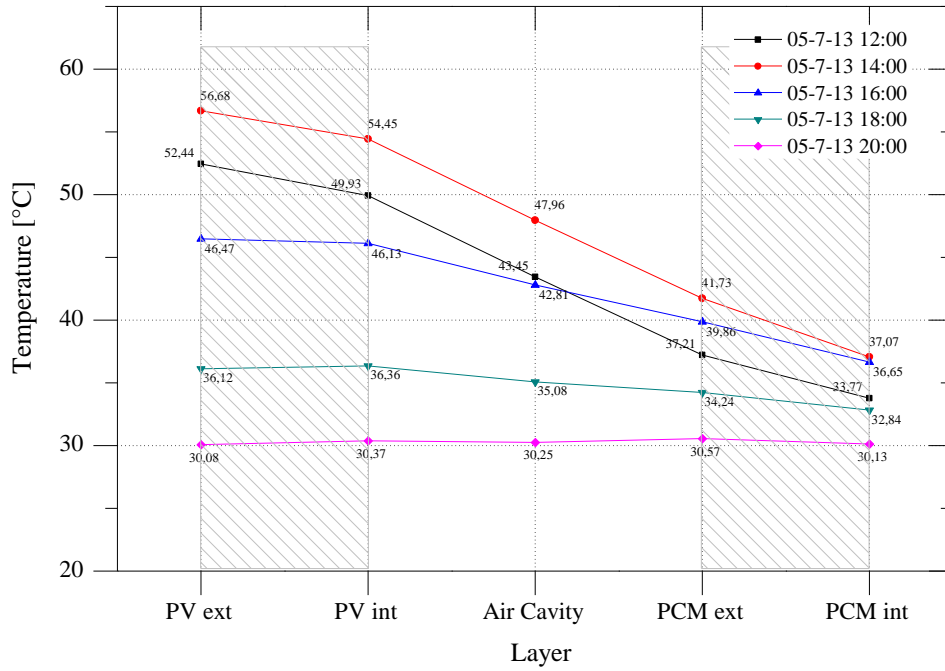


Fig. 5.22. Cross section temperatures at different times, 5 July 2013

Similarly to what happened on 25 February, Fig. 5.23 represents the heat flux from the sunny day of July 5, where we can observe the same discrepancy in the F5 (PCM int) sensor due to the absorption and release of energy in the form of latent heat.

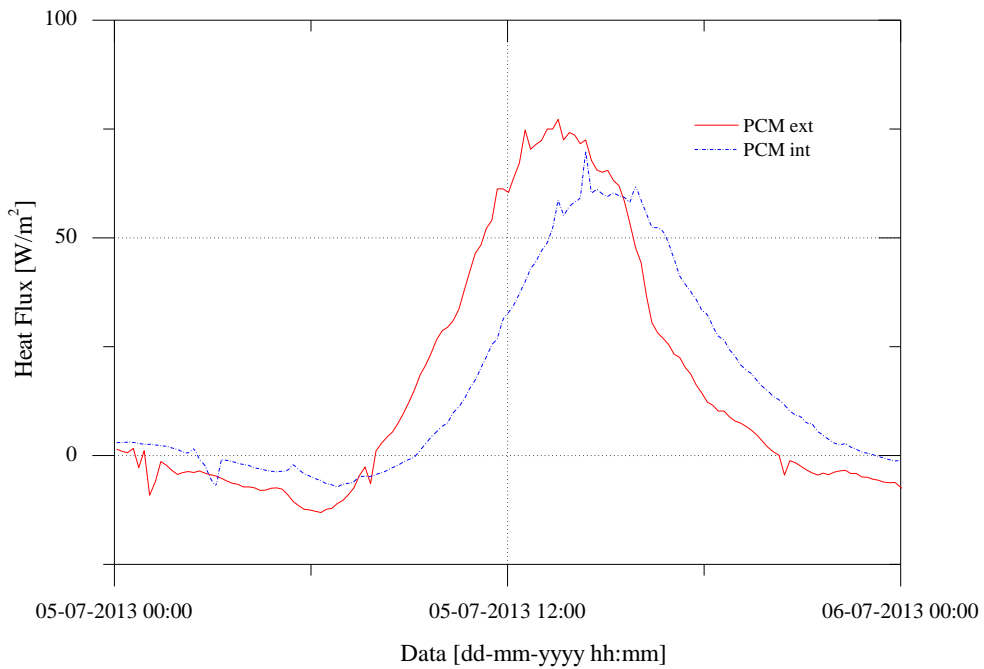


Fig. 5.23. Heat flux through surfaces 5 July 2013

For this summer campaign an analysis of the thermal performance was also performed for 19 June when the climatic conditions were slightly different. As can be seen from Fig. 5.24, it was a mild day with average outdoor and indoor temperatures of 20°C and 16°C, respectively. This cloudy day presents a low radiation on the vertical plane, ranging widely between 100 W/m² and 400 W/m². The temperature profile of the PV module and air gap exhibit a similar variation to the radiation profile, with minimum temperatures of 20°C and maximum of 34°C. The PCM continues to exhibit regular behavior and keeps the temperature between 19°C and 23°C.

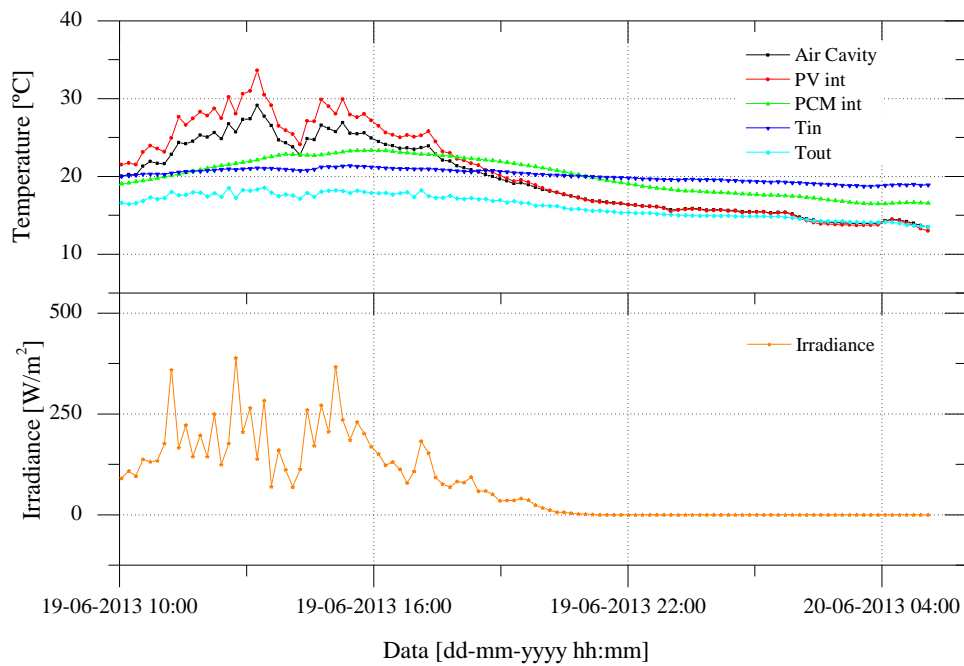


Fig. 5.24. Temperature and irradiation values, 19 June 2013

Table 5.7 and Fig. 5.25 represent the temperature profile for this June day. The greatest temperature difference through the day is still shown by the PV module with values between 17°C and 29 °C. The inner face of the PCM has a low range of values over time, between 20 and 23 degree Celsius.

Table 5.7. Cross section temperatures at different times, 19 June 2013

Layer	Temperature [°C] for 19-06-2013				
	12:00	14:00	16:00	18:00	20:00
PV ext	29.13	27.00	24.87	20.66	17.13
PV int	28.81	27.10	25.49	21.11	17.59
Air Cavity	25.88	24.81	23.87	20.40	17.59
PCM ext	22.69	23.67	23.8	22.03	19.89
PCM int	21.44	22.80	23.17	22.17	20.49

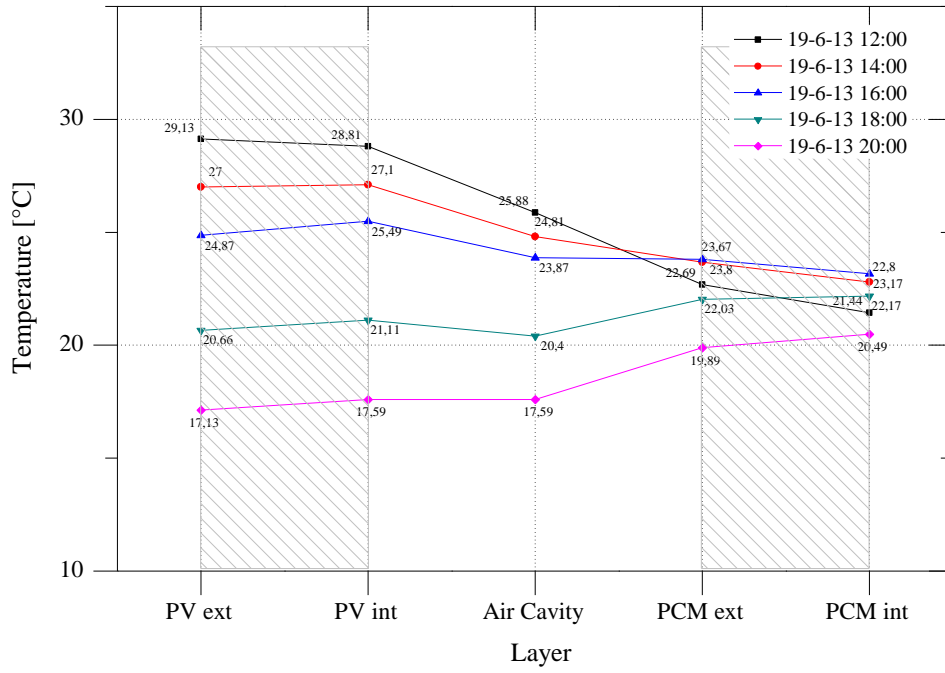


Fig. 5.25. Cross section temperatures at different times, 19 June 2013

Fig. 5.26 reinforces the phenomenon of energy transfer in the form of latent heat seen in Fig. 5.19 relating to a cloudy day. The same heat flux profile smoothing is noted on the inner surface of the PCM (F5).

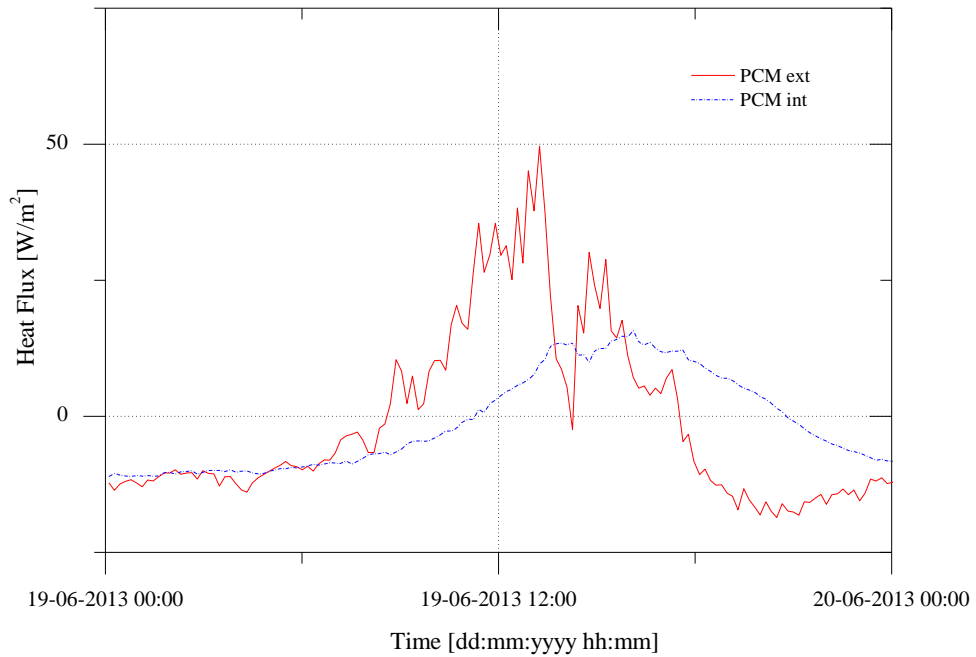


Fig. 5.26. Heat flux through surfaces 19 June 2013

5.5.3. Campaigns Comparison

To analyze the influence of some parameters on the energy transfer to and across the system, it is best to place the results side by side for comparison (Fig. 5.27). In this case, radiation and outside temperature are the main parameters which influence this transfer. The energy transfer between the system and the building takes place by cavity ventilation (q_v) and by heat flux (q_{int}), which passes through the PCM. q_{int} is the experimental data from the F5 (PCMint) sensor (Table 5.2), and q_v is the application of equation (3.25), where the air mass flow rate is calculated using equation (4.1), which is validated in sub-section 5.6.3.

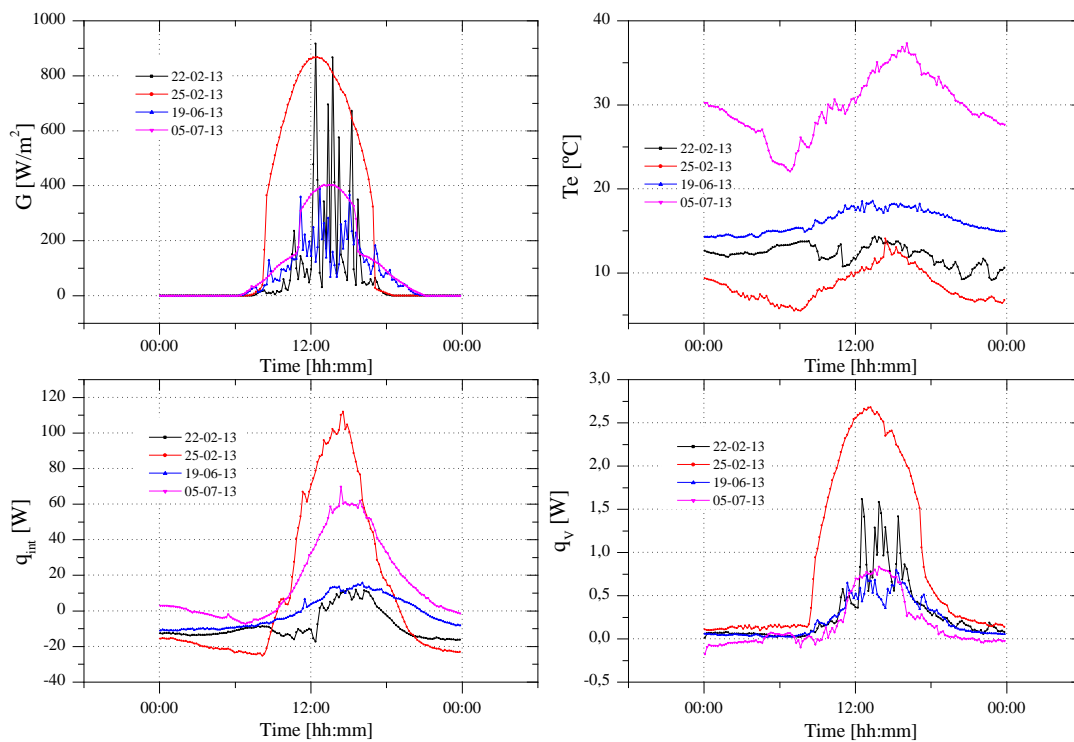


Fig. 5.27. Four days' parameters: Radiation (top left), Exterior temperature (top right); Four days' data: Heat flux through PCM (bottom left), Air flow system (bottom right)

The influence of radiation on system performance is obvious. The q_{int} and q_v profiles follow the radiation profile. However, q_{int} has a “stable” profile configuration due to the latent heat phenomena.

5.5.3.1. Stratification Inside the Air Cavity

Table 5.8 and Fig. 5.28 present the vertical temperature profile for the air cavity center line.

Table 5.8. Dimensionless vertical maximum temperatures

H^*	Maximum temperature within air cavity [°C]			
	22/02/2013	25/02/2013	19/06/2013	05/06/2013
0	20.38	20.66	21.11	29.86
0.27	26.57	46.79	28.30	46.73
0.5	28.61	49.85	29.12	48.26
0.73	30.63	53.42	29.08	49.82

The temperatures are presented as function of a dimensionless height,

$$H^* = \frac{y}{H} \quad (5.3)$$

where y is the vertical position of the sensor within the air cavity and H is the total height of the cavity. $T_{in} = T_i$ is considered.

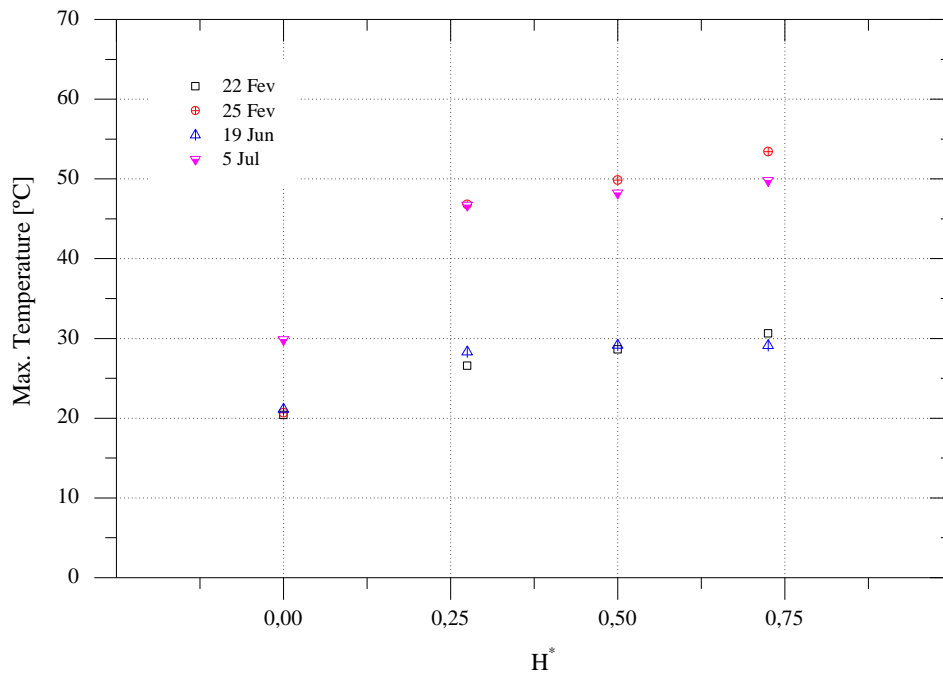


Fig. 5.28. Stratification within the air cavity

It is possible to observe how the air warms up in the vertical direction of the air cavity. The stratification phenomenon is evident on higher radiation days, particularly on 25 February, where the difference between the inlet and outlet temperature reaches 32 °C.

5.6. VALIDATION OF THE NUMERICAL MODEL

5.6.1. Introduction

The numerical model (sub-section Chapter 4) was validated against experimental data collected over a 2-day period (highlighted in Fig. 5.13) and Fig. 5.20). The vents remained closed throughout the night and were open during the day. The time step used in the simulations corresponds to that used by the data acquisition system, which is 10 minutes. The initial conditions in the numerical model were set according to the corresponding measured values. As the Solar XXI building where the system was tested is an office building that is occupied in the daytime, only the results for the period of time from 10h00 to 17h00. are presented. The numerical versus experimental results of the thermal behavior of the BIPV/T-PCM system in terms of the internal surface temperature of the photovoltaic module (PV int), the PCM (PCM int) and the air in the gap (Air) are shown in Fig. 5.29.

5.6.2. Validation

The comparison between experimental and numerical results shows relatively good agreement. The maximum difference between the numerical and experimental results for the first and second day is around 3.5-4.0 °C and 1-2.6°C, respectively. A likely explanation of these differences is that they occur when the vents are opened and air begins to flow through the gap driven by the pressure differences which are also induced by the wind action on the building surface, which was not measured. The numerical model was not able to reliably describe the PV temperature surface changes during this phase of the day. This dynamic behavior is also observed in the case of the air gap temperature. However, the differences in the PCM gypsum board temperatures are smaller.

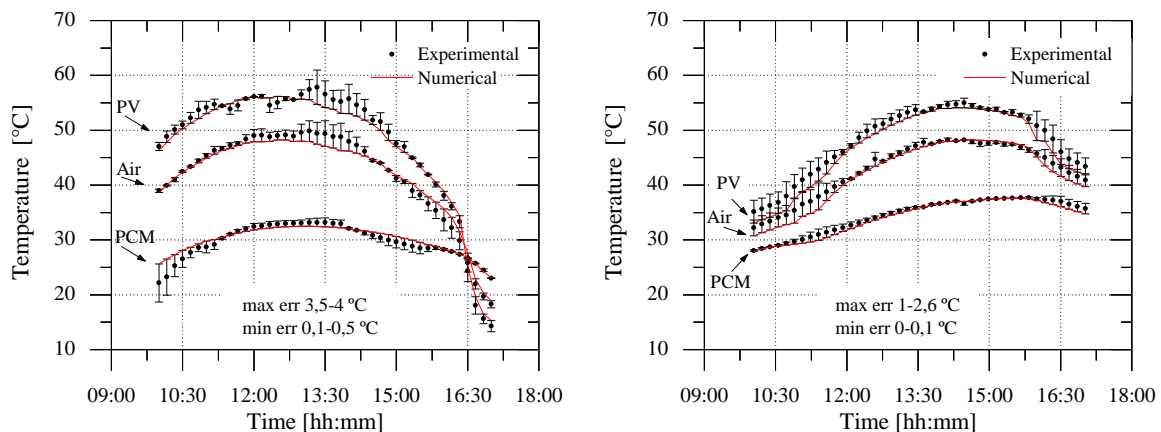


Fig. 5.29. 25 February (left); 5 July (right) [37].

As with the surface temperatures, the heat fluxes through layers are also validated. In terms of heat fluxes, the numerical versus experimental results of the thermal behavior of the BIPV/T-PCM for the photovoltaic module (PV int), exterior and interior PCM (PCM_ext, PCM_int) are shown in Fig. 5.30 for 25 February and in Fig. 5.31 for 5 July.

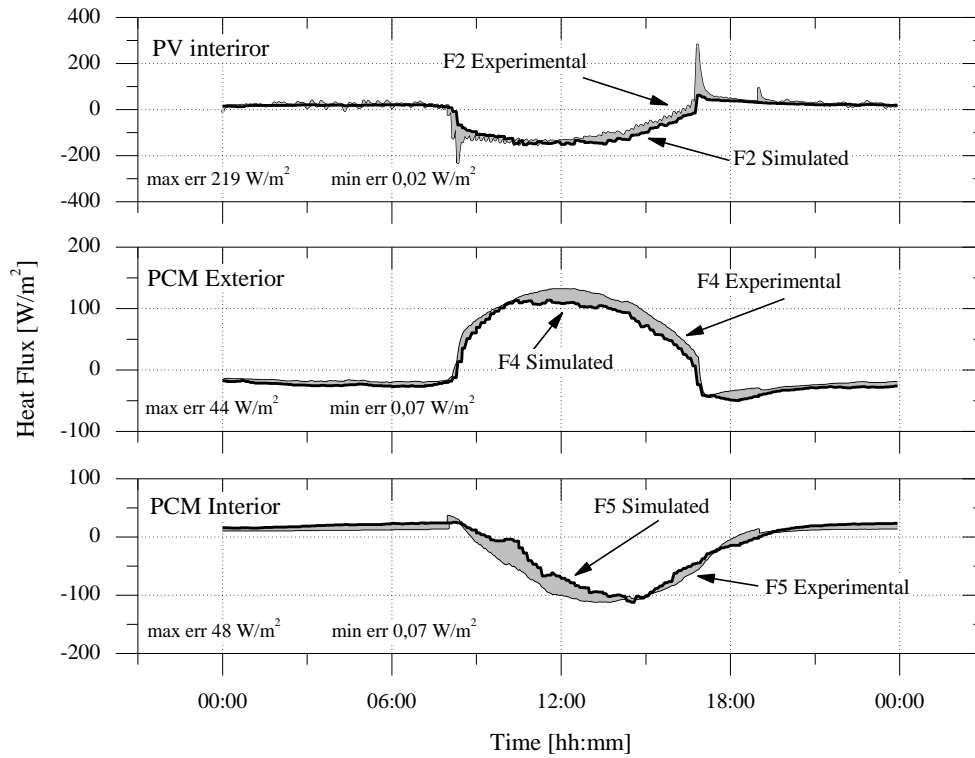


Fig. 5.30. Simulated versus experimental values of heat flux through layers for 25 February 2013

The experimental and numerical results show relatively good agreement, for both days, when compared. The minimum error is limited to a very small range between 0.02-0.07 W/m^2 for 25 February (Fig. 5.30) and 0.005-0.02 W/m^2 for 5 July (Fig. 5.31), and the lowest error values are recorded at night. The maximum difference between the numerical and experimental results is 44 to 48 W/m^2 in Fig. 5.30 and 13 to 18 W/m^2 in Fig. 5.31. There are two peaks, of 219 W/m^2 (Fig. 5.30) and 137 W/m^2 (Fig. 5.31), for the maximum error that can be explained by the sensitivity of the sensor to the sudden change in solar radiation as it relates to the sensor on the PV module.

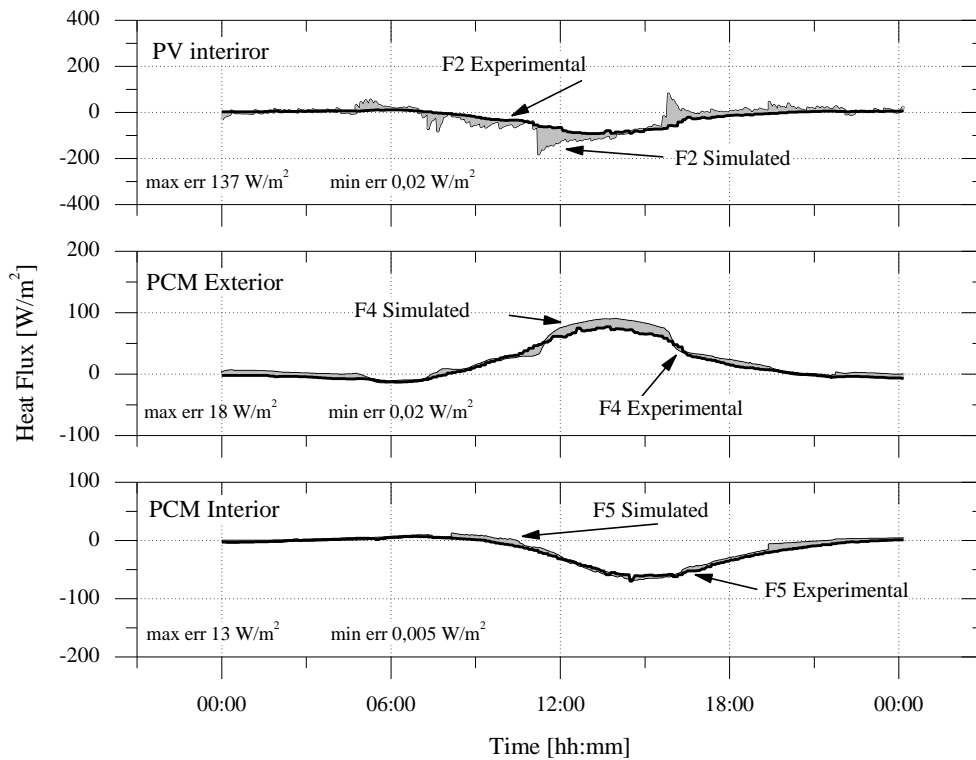


Fig. 5.31. Simulated versus experimental values of heat flux through layers for 5 July 2013

5.6.2.1. Thermography

Fig. 5.32 shows thermal images. Images were recorded at 12:00 on a sunny day (5 July). Comparing the images in Fig. 5.32 with Table 5.6 and Fig. 5.22, it can be seen that the respective values are similar. Table 5.6 give a temperature of 52.44°C for the PVext and 33.77°C for PCMint, while in Fig. 5.32 the figures are 51.9°C and 29.7°C, respectively. Taking into account the reflectivity of the glass, the thermal camera may approximate values with some margin of error. However the temperature that the camera measures relates to the glass where are installed the temperature sensors.

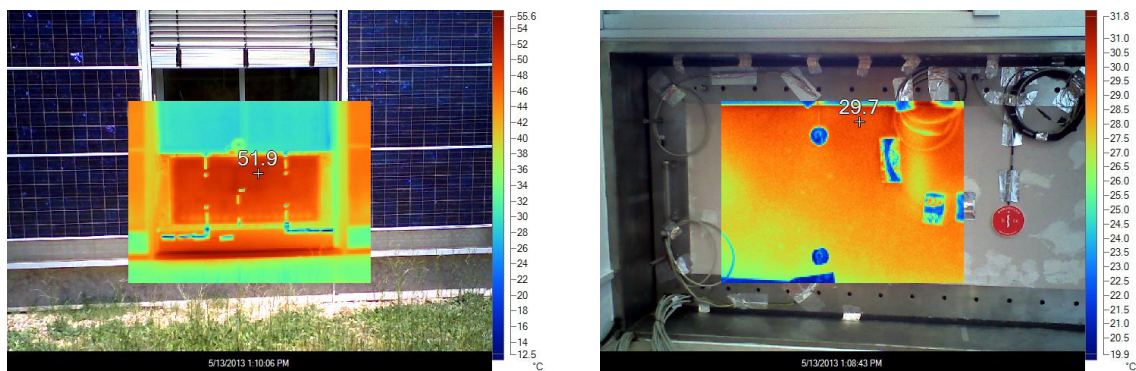


Fig. 5.32. Thermal images and photos at 12:00 on 5 July 2013

5.6.3. Air Velocity Within the Cavity

Fig. 5.33 was obtained using equation (4.1) to estimate the air velocity inside the cavity. The air channel was divided into five vertical volumes and the equation was applied to each. The figure also shows the experimental data of the average velocity (V_{ch_exp}) of small periods (10 minutes) obtained using the hotwire anemometer described in sub-section 5.4.4. Although there are few measurements, the air velocity model could be considered validated, as the calculated and experimental values show good agreement.

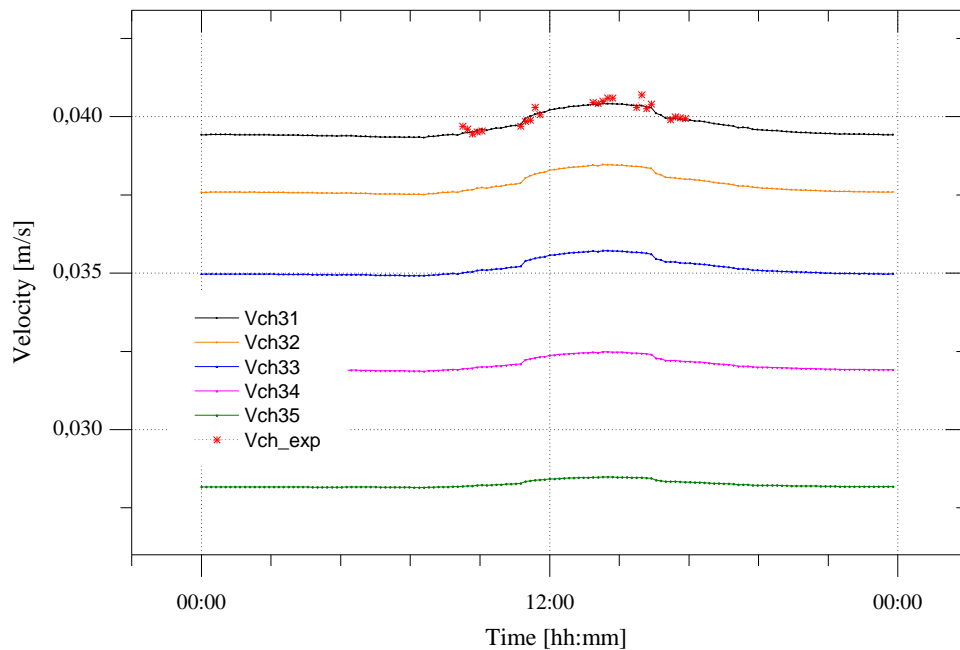
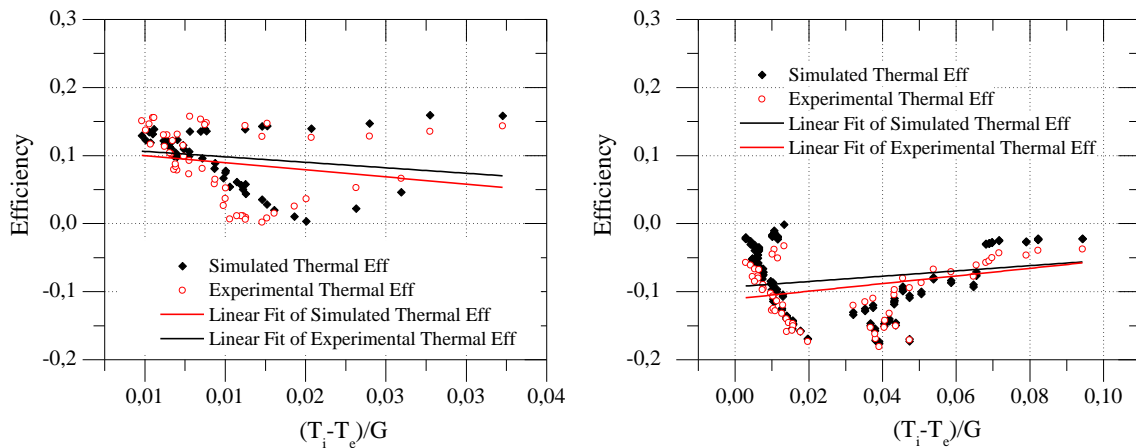


Fig. 5.33. Air velocity within cavity

5.6.4. System Performance

5.6.4.1. Thermal

The system performance is shown in Fig. 5.34 where the total system efficiency is plotted together with the thermal efficiency as a function of the parameter $(T_i - T_e)/G$, [$m^2 \cdot ^\circ C/W$]. For better readability, the best day of winter (25 February) and summer (5 July) are presented.



Simulated

$$\text{Efficiency} = 1,60969 \left(\frac{T_i - T_e}{G} \right) + 0,1223 \quad R^2 = -0,01402$$

Simulated

$$\text{Efficiency} = 0,38792 \left(\frac{T_i - T_e}{G} \right) - 0,09278 \quad R^2 = 0,04114$$

Experimental

$$\text{Efficiency} = 2,09545 \left(\frac{T_i - T_e}{G} \right) + 0,1210 \quad R^2 = -0,01352$$

Experimental

$$\text{Efficiency} = 0,56022 \left(\frac{T_i - T_e}{G} \right) - 0,11051 \quad R^2 = 0,01726$$

Fig. 5.34. Thermal BIPV-PCM system efficiency. 25 February 2013 (left), 5 July 2013 (right)

As can be seen in Fig. 5.34, the simulated and experimental values show good agreement.

In winter the system has a maximum thermal efficiency of 15.8% but in summer the thermal efficiency has negative values due to the reversal of the direction of the heat flux.

For both days, the simulated and experimental linear regression has similar values for slope and YY axis intercept. Note that the linear regression was performed not with the intention of representing the behavior of the function (as can be seen by the low R^2 value), but to compare the modeling points to the experimental. R^2 has a very low value but one that is very similar for the experimental and simulated efficiency.

5.6.4.2. Electrical

Fig. 5.35 shows the simulated electrical system efficiency. For technical reasons related to construction, it was not possible to present experimental data from the PV panel. The electrical model was validated by the author in [73].

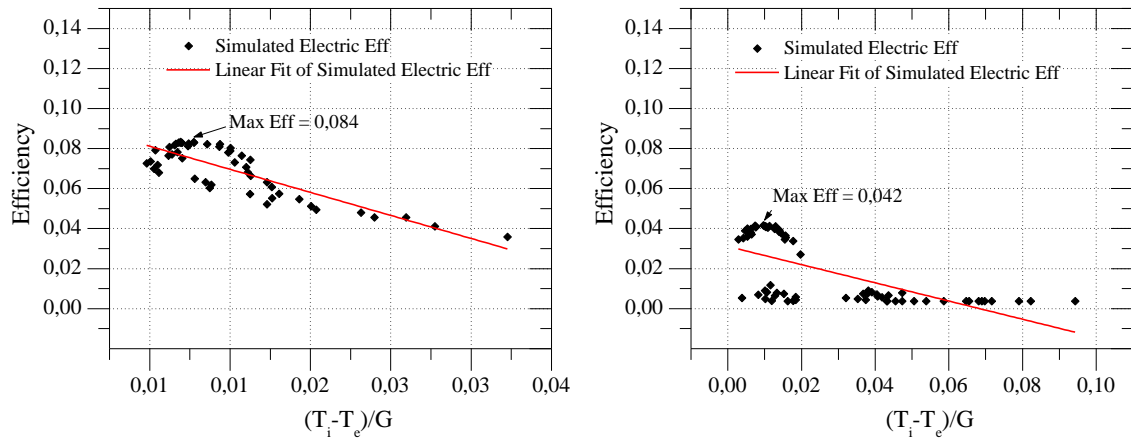


Fig. 5.35. Electrical BIPV-PCM system efficiency

The simulated values show a maximum electrical efficiency of 8.4% for the winter and 4.2% for the summer configuration. The very low value for summer is easily justified by the high position of the sun relative to the vertical facade where the system is installed.

The values for efficiency are not very satisfactory, especially for summer, where the thermal efficiency has only negative values due to the reversal of the direction of the heat flux. Bearing in mind that this type of system is sized to winter seasons having as reference the countries of northern Europe, it is necessary to adapt them to the summer climate of Portugal. In this sense it is not expected that the system reaches a very high efficiency for the summer, but that minimizes heat transfer into the building.

Given this less promising scenario for summer results, there is a clear need for system optimization to find new parameters able to improve efficiency.

Chapter 6. SYSTEM OPTIMIZATION

6.1. INTRODUCTION

Based on the results obtained in numerical and experimental analysis (Chapter 4 and Chapter 5), an optimization of the system is justified, as stipulated in the initial objectives, to decrease the high temperatures that the prototype presents in summer, and to improve system performance in winter in order to achieve greater overall efficiency.

In this chapter, it is intended to optimize the problem under study and find the best solution, considering a set of constraints to which it is subject. The aim is to find the maximum thermal efficiency set by **equation (6.1)** for the winter configuration (see equation (4.26)),

$$\eta_{tw} = \frac{q_{int} + q_V}{G \times A} \quad (6.1)$$

and by **equation (6.2)** for the summer configuration (see equation (4.27)).

$$\eta_{ts} = \frac{q_V - q_{int}}{G \times A} \quad (6.2)$$

However, increased thermal efficiency may result in reduced electrical efficiency. A constraint is therefore added to the optimization. In this case, the purpose of this restriction, set by equation (6.3), is to ensure the maximum electrical efficiency of the PV panel (see equation (4.29)).

$$\eta_e = \frac{P}{G \times A} \left(1 - \beta_c (T_{mpv} - T_{NOCT}) \right) \quad (6.3)$$

This is a nonlinear problem, which makes finding the solution a difficult task. Some common methods for nonlinear optimization in solving complex engineering problems include the Method of Lagrange Multipliers, Newton's Method, Quasi-Newton Method, Conjugate Gradient Method, Levenberg-Marquardt Algorithm Method, and the Genetic Algorithm (GA).

The GA is used here. The GA is an optimization method that can be applied to problems with or without constraints, for which there is no standard optimization algorithm. Such problems include those in which the objective function is discontinuous, non-differentiable, stochastic or highly nonlinear. This algorithm uses the basic principles of genetics, such as selection, crossover and mutation, to get the best result. A common application of GAs is for the optimization of nonlinear functions dependent on several parameters, where the goal is to find a set of possible values that maximize or minimize the result.

The following section gives a brief description of the genetic algorithm method (GA) and its application to the optimization problem.

6.2. OPTIMIZATION METHOD (GA)

The GA belongs to the class of stochastic optimization algorithms that work in a "randomly oriented" manner, according to probabilistic rules based on analogy with the mechanisms of natural genetics.

The genetic algorithm emerged in the 1970s in the work of John Henry Holland, at a time when several computer scientists were independently studying evolutionary systems, sharing the idea that evolution could be used as an optimization tool for engineering problems. All these systems aim to "evolve" a population of candidate solutions to the problem towards an optimal solution,

using operators inspired by genetic variation and natural selection. This process is repeated until certain a stopping criterion, set at the outset, is met [77].

It was in 1975 that Holland published his book *Adaptation in Natural and Artificial Systems* [77], which presented the GA as an abstraction of biological evolution and gave a theoretical framework for adapting it for evolutionary problems. Subsequently, the methodology was developed in more detail by David E. Goldberg, a former student of Holland. Goldberg's studies were published in *Genetic Algorithms in Search, Optimization & Machine Learning* [78].

According to Holland, the GA is a method that enables evolution from one population of "problem solutions" to a new population, using a kind of natural selection, together with genetically inspired operators, particularly the crossing, mutation and inversion.

The GA is based on the repeated change of a population consisting of possible solutions to the problem, among which, in each step, the genetic algorithm will randomly pick the one that is best suited to generating a new population. We can thus think of a hierarchical system, where the best parents are indicated in each generation to produce children who will form the next generation. Over successive generations, the population evolves towards an optimal solution.

6.2.1. Elements of the Genetic Algorithm

Although a great deal of work has been done in recent years on the genetic algorithm proposed by Holland, nowadays many researchers use the term "genetic algorithm" to describe something far from his original conception. Therefore, there is no strict definition of "genetic algorithm" that is accepted by the scientific community as a whole that shares the same evolutionary computation technique. The main differences between the GA and classical optimization methods are shown in the table below.

Table 6.1. Differences between the GA and classical optimization methods

Classic Algorithm	Genetic Algorithm
Generates a single point at each iteration.	Generates a population of points at each iteration.
The sequence of points approaches an optimal solution.	The best point in the population approaches an optimal solution.
Selects the next point in the sequence by a deterministic computation.	Selects the next population by computation which uses random number generators.

However, most GAs have at least the following elements in common:

- **Population** – an array of individuals, usually understood as a set of chromosomes, representing a set of possible solutions to the problem (e.g. bits sequence of binary language). Each chromosome is formed by "genes" (e.g. bits). Each gene has two possible states: 0 and 1. Each chromosome can be thought of as a point in the search space of possible solutions. At each iteration, the genetic algorithm performs a series of computations on the current population to produce a new population. Each successive population is called a new generation.
- **Selection** – a process that randomly chooses between candidate population elements to integrate a new population, in the hope of it being better than the previous one, i.e. the selection operator chooses chromosomes from the population that will be allowed to reproduce. The strategy is that the fittest chromosomes produce better descendants than the less fit. During this selection process, candidates are subject to a review in accordance with the fitness function that allows them to pass to descendants. There are many methods to make the selection. The main ones are: Roulette, Tournament, Deterministic Sampling (DS), Stochastic Remainder Sampling (SRS) and Stochastic Universal Sampling (SUS). All of them are described by Goldberg [78].
- **Crossing** – occurs among the selected candidates to produce new descendants. The crossing exchanges subparts of two chromosomes by imitating the biological recombination between two single chromosomes.
- **Mutation** – randomly changes the state of the genes of the descendant chromosomes.

These genetic operators are responsible for improving the population.

6.3. APPLICATION OF THE METHOD

Implementing genetic algorithms requires the prior definition of essential parameters for the optimization routine. It starts by specifying the initial parameters and randomly creates an initial population of individuals within these limits. Then the suitability of each individual is checked by the objective function. Genetic operators that modify the population with the aim of improving it are applied. This iterative process, corresponding to successive generations, continues until it reaches convergence [79]. Fig. 6.1 shows the flowchart of a simple routine optimization through genetic algorithms.

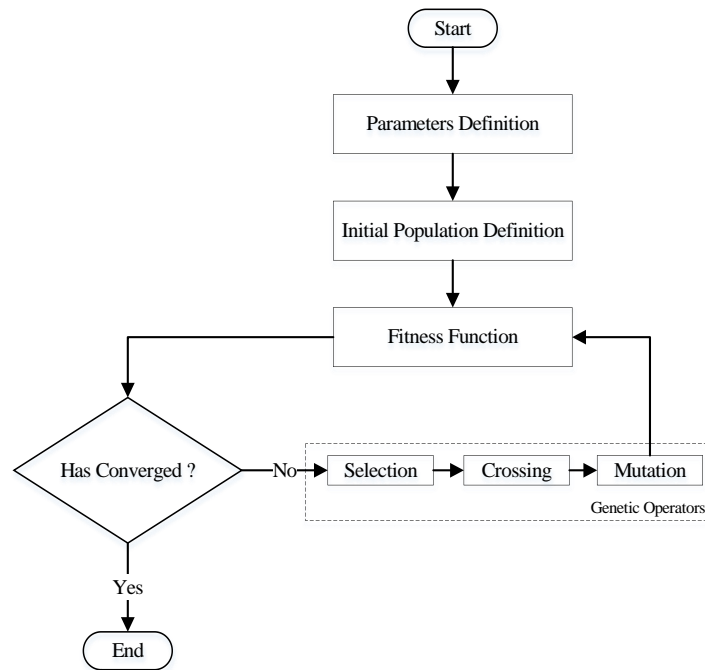


Fig. 6.1. Flowchart of a simple routine optimization through genetic algorithms [79]

In the problem under consideration in this flowchart, the Fitness Function is the energy efficiency mentioned in sub-section 4.3., which aims to maximize. After careful analysis of the experimental data, the selected variables are those shown in Table 6.2. Variables were chosen for their degree of influence on the system.

- **Ventilation** is always an important variable in this type of system. By changing the intensity, the rate of energy transfer between the air cavity and the surrounding environment is adjusted. On the other hand, increasing the intensity cools down the photovoltaic module.
- The **air cavity thickness** influences not only the mass flow rate but also the heat transfer by radiation and conduction between the first and second layer. The increased flow also cools down the photovoltaic module.
- The **PCM thickness** has an influence on heat transfer by conduction in the second layer. High values of this variable may indicate the need for isolation.
- The **latent heat** phenomenon is the novelty in this type of system. By introducing this variable in the optimization process, it is intended to understand its influence on the behavior of the gypsum board, and on the absorption and release of energy that will regulate the temperature of the photovoltaic module and the interior room.

The corresponding parameters of the Fitness Function are:

Table 6.2. Optimization parameters

Parameter	Variable
Ventilation	Vch
Air Gap	AirCavityThickness
PCM Thickness	PCMthickness
Latent Heat	LatentHeat

that are initialized in the respective intervals:

Table 6.3. Variables range

Variable	Range	Units
Vch	[0,035 – 10]	m/s
AirCavityThickness	[0,02 – 0,1]	m
PCMthickness	[0,025 – 0,050]	m
LatentHeat	[1000 – 50000]	J/kg

The initial population consists of a group of individuals represented by $X^i = [X_1^i \ X_2^i \ X_3^i \ X_4^i]$ with $i = 1, \dots, n \in IN$ where

$$X_1^i = Vch$$

$$X_2^i = AirCavityThickness$$

$$X_3^i = PCMthickness$$

$$X_4^i = LatentHeat$$

Indeed, the initial population of individuals is generated randomly within the limits and represents the matrix

$$P^0 = \begin{bmatrix} X_1^{01} & X_2^{01} & X_3^{01} & X_4^{01} \\ \dots & \dots & \dots & \dots \\ \dots & \dots & \dots & \dots \\ X_1^{0n} & X_2^{0n} & X_3^{0n} & X_4^{0n} \end{bmatrix} \quad (6.4)$$

It is then verified by the fitness function, the aptness of each individual, and all the genetic operators that manipulate the population are applied to improve it.

In each generation (iteration) there is a population represented by

$$P^k = \begin{bmatrix} X_1^{k1} & X_2^{k1} & X_3^{k1} & X_4^{k1} \\ \dots & \dots & \dots & \dots \\ \dots & \dots & \dots & \dots \\ X_1^{kn} & X_2^{kn} & X_3^{kn} & X_4^{kn} \end{bmatrix} \quad (6.5)$$

This manipulation occurs over successive generations (iterations) and it is therefore essential to ensure a sufficient number of generations (iterations) to get the optimum result.

The iterative process ends with some pre-defined convergence criteria:

- A maximum permissible error for the value of each individual is reached.
- The genetic diversity of the population is tested. If individuals are very similar to each other, i.e. if the evaluation of the objective function of each individual gives very similar results, this may mean that they are in the same region. This features the presence of a maximum or minimum of the function.
- A final inspection must be made (sub-section 6.3.1), for example, stipulating a maximum allowable number of generations (iterations).

The number of individuals in the population is selected according to the complexity of the problem to be solved. With a small number of individuals, the search universe may be poorly represented. If the number of individuals is very large the computational time may become infeasible. A study on how to identify the optimal number of individuals was performed by Haupt [80].

6.3.1. Software Application (Matlab)

Optimizations are complex operations and require the use of powerful software. Matlab[®], in which the numerical approach was implemented, has an optimization toolbox (Appendix C) that can apply various methods, including genetic algorithms.

This toolbox requires synchronization between the Matlab[®] code language, Simulink[®] environment and Optimization Function. For this reason, a Fitness Function, Constraint Function and an interface between the source (Matlab[®]) language and Simulink[®] environment must be created.

The Optimization Function is defined by two functions:

- Fitness Function** – the function to be optimized. For standard optimization algorithms, this is known as the “Objective Function”. It is written as a file or anonymous function in Matlab® code (Appendix A), and it passes as a function handle input argument to the main genetic algorithm function (inserted in the “Problem/Fitness_function” field of the optimization tool app). This function sets the variables of the problem and the optimization objective. The toolbox software tries to find the minimum of the fitness function.
- Constraint Function** – the function that puts restrictions on the Fitness Function. For standard optimization algorithms, this is known as the “Restriction Function”. It is also written as a file or anonymous function in Matlab® code (Appendix B), and it passes as a function handle input argument to the main genetic algorithm function (inserted in the “Constraint/Nonlinear_constraint_function” field of the optimization tool app). The function sets the variables’ lower and upper bounds and the constraint to be applied to the Fitness Function.

Note: Nonlinear inequality constraints have the form $c(x) \leq 0$, where c is a vector of constraints, one component for each constraint. Similarly, nonlinear equality constraints are of the form $ceq(x) = 0$. Nonlinear constraint functions must return both c and ceq , the inequality and equality constraint functions, even if both do not exist. Return empty [] for a non-existent constraint.

Fig. 6.2 shows the functional diagram of the optimization toolbox.

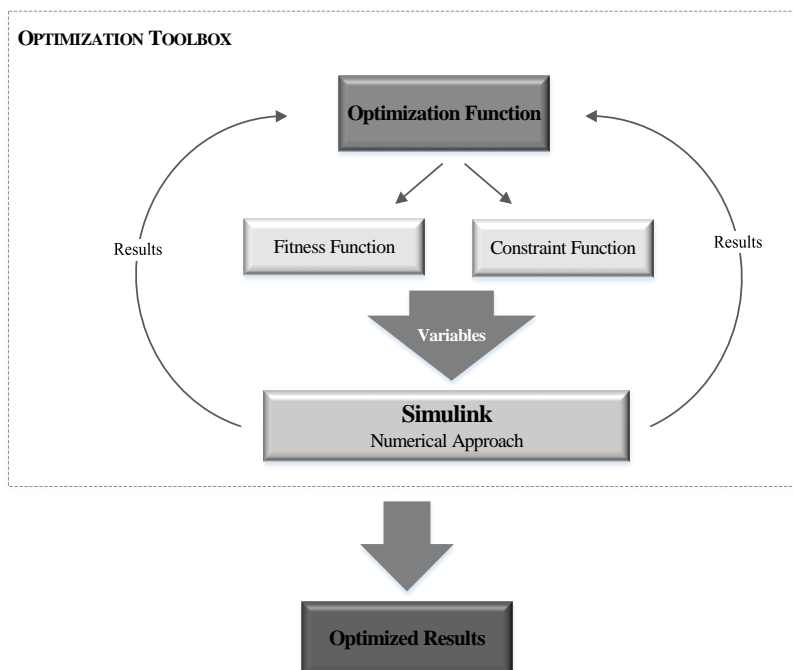


Fig. 6.2. Functional diagram of the optimization toolbox

The optimization process starts with the optimization function. It begins by defining the type of solver, that is, the desired optimizing method (in this case it is the genetic algorithm method).

The optimization function then runs the optimization function where the number of variables is defined. Simultaneously, the optimizing function runs the constraint function where all constraints are defined. From this process a vector of variables is created that gives input to the Simulink[®] environment, where the numerical approach to the problem is computed. Simulink[®] returns a vector with the value of the variables to optimize (thermal and electrical efficiency), the optimization function analyzes it using the GA method, and the interactive process resumes until some pre-defined stop criterion is found:

Stopping criteria can be defined in the optimization tool application under the Stopping Criteria field (Appendix C). The genetic algorithm uses the following conditions to determine when to stop:

- **Generations** – the algorithm stops when the number of generations reaches the value of Generations.
- **Time limit** – the algorithm stops after running for an amount of time in seconds equal to Time limit.
- **Fitness limit** – the algorithm stops when the value of the fitness function for the best point in the current population is the same as the fitness limit or lower.
- **Stall generations** – the algorithm stops when the average relative change in the fitness function value over Stall generations is less than Function tolerance.
- **Stall time limit** – the algorithm stops if there is no improvement in the objective function during an interval of time in seconds equal to Stall time limit.
- **Stall test** – the stall condition is either average change or geometric weighted. For geometric weighted, the weighting function is $1/2n$, where n is the number of generations prior to the current one. Both stall conditions apply to the relative change in the fitness function over Stall generations.
- **Function Tolerance** – the algorithm runs until the average relative change in the fitness function value over Stall generations is less than Function tolerance.

Nonlinear constraint tolerance – the Nonlinear constraint tolerance is not used as stopping criterion. It is used to determine the feasibility with respect to nonlinear constraints. Also, a point is feasible with respect to linear constraints when the constraint violation is below the square root of Nonlinear constraint tolerance.

Each of these criteria is relevant and has to be adjusted to the problem under study, in order to ensure that the optimization routine does not terminate prematurely or perpetually extend.

The desired plot checkbox should be marked in the Plot Functions field [81].

6.3.1.1. Maximizing an Objective

All solvers attempt to minimize an objective function. If there is a maximization problem (as in this problem), that is, a problem of the form:

$$\max_x f(x), \tag{6.6}$$

then, it must be defined as $g(x) = -f(x)$ and g should be minimized.

6.4. OPTIMIZATION SCENARIOS

For any optimization process it is necessary to define the scenarios to be analyzed. In this work, the system is divided into two different objectives. As in the experimental analysis, optimization will also be oriented in the winter configuration and the summer configuration. In these configurations, the entire optimization process and all the variables are unchanged. The difference is in the inputs and in the system behavior.

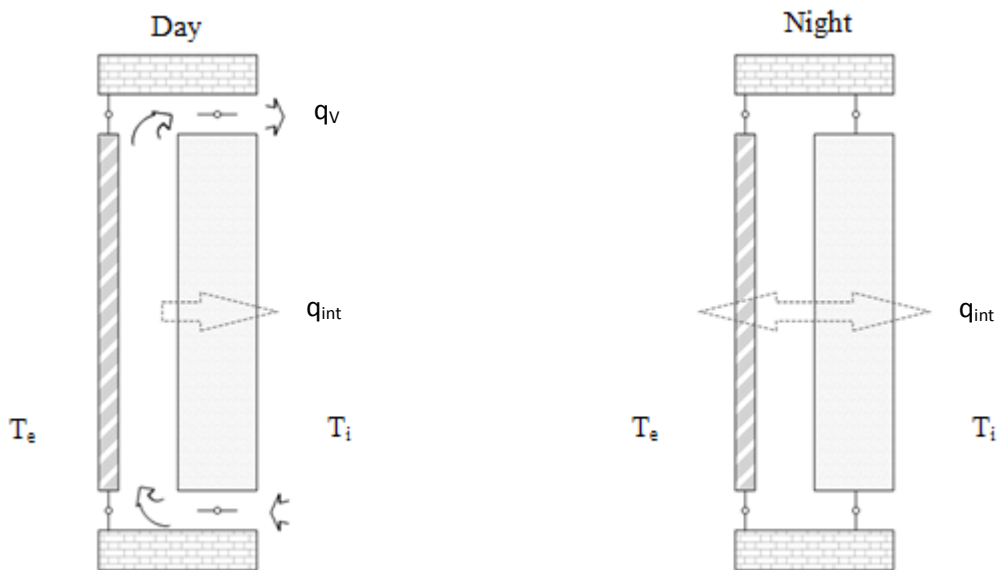


Fig. 6.3. Winter configuration for the optimization process

Fig. 6.3 shows the winter configuration. During the day, the vents remain open and the energy transfer takes place with the recirculation of air between the room and the air cavity (q_v), and with the heat transfer by conduction through the PCM board (q_{int}). During the night, when the room air is warmer than the interior of the cavity air, the vents remain closed and energy transfer only occurs by heat transfer by conduction through the PCM board (q_{int}).

The aim in the winter is to obtain the maximum energy transfer when the air inside the cavity is warmer than the room (day), and to avoid energy loss to the outside when the air inside the cavity is colder than the room (night).

Fig. 6.4 shows the summer configuration. In this configuration the outer vents are always open. The energy transfer takes place with the circulation of air between the outdoor environment and the air cavity (q_v), and with the heat transfer by conduction through the PCM board (q_{int}). During the day the simulation is done with forced ventilation and at night the option is to simulate natural ventilation in order to save energy.

The aim in the summer is to remove the maximum energy from the air cavity to the outdoor environment in order to reduce the PV module temperature, and minimize the heat transfer by conduction through the PCM board to the room.

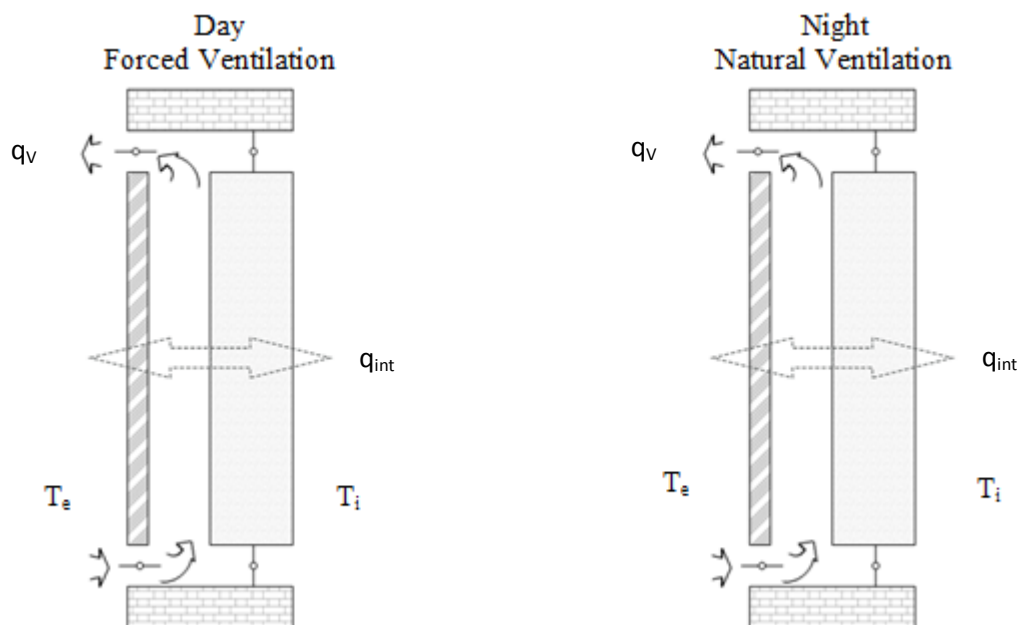


Fig. 6.4. Summer configuration for the optimization process

At the beginning of the optimization process we have to define the inputs in the system. In addition to the physical characteristics of all the materials, the weather conditions that may affect

the behavior of the system are also introduced. Fig. 6.5 shows inputs for the winter (left) and for the summer (right) of the climatic conditions for the optimization process.

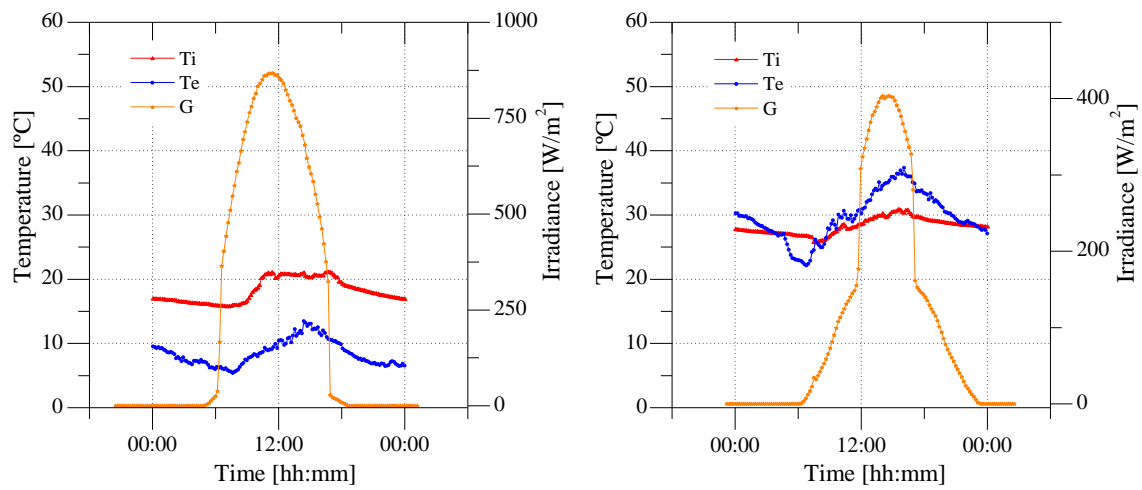


Fig. 6.5. Climatic conditions for the optimization process

6.5. RESULTS

The results of the optimization process covering the test cases shown in sub-section 0 are presented graphically and numerically for better analysis. The results of the optimization process for the winter climatic conditions are presented first, and then the results for the summer climatic conditions. In each case, the value of maximum thermal efficiency (Fitness Function), the maximum value of electrical efficiency (Constraint Function), the value of the variables obtained to achieve the maximum value of these efficiencies, and the corresponding temperatures obtained are presented.

6.5.1. Winter

The thermal efficiency values were obtained for several generations of individuals created by the optimization process using genetic algorithms. In the winter configuration, the optimization process achieved a thermal efficiency of 54.4%, as shown in Table 6.4. This is the result of the objective defined in the Fitness Function.

Table 6.4. Thermal efficiency from winter optimization process

Fitness Value	Generation						
	0	1	2	3	4	5	6
Mean Fitness	0.2705	0.5362	0.5439	0.5443	0.5443	0.5443	0.5441
Best Fitness	0.3223	0.5411	0.5442	0.5443	0.5443	0.5443	0.5443

The fitness value of an individual is the value of the Fitness Function for that individual. Because the toolbox software finds the minimum (or maximum, see sub-section 0) of the Fitness Function, the best fitness value for a population is the smallest (or highest) fitness value for any individual in the population.

The half red dots in Fig. 6.6 denote the best fitness values, while squares denote the averages of the fitness values in each generation. The plot also displays the best and mean values in the current generation, numerically at the top.

Typically, the best fitness value improves rapidly in the early generations, when the individuals are further from the optimum. The best fitness value improves more slowly in later generations, whose populations are closer to the optimal point.

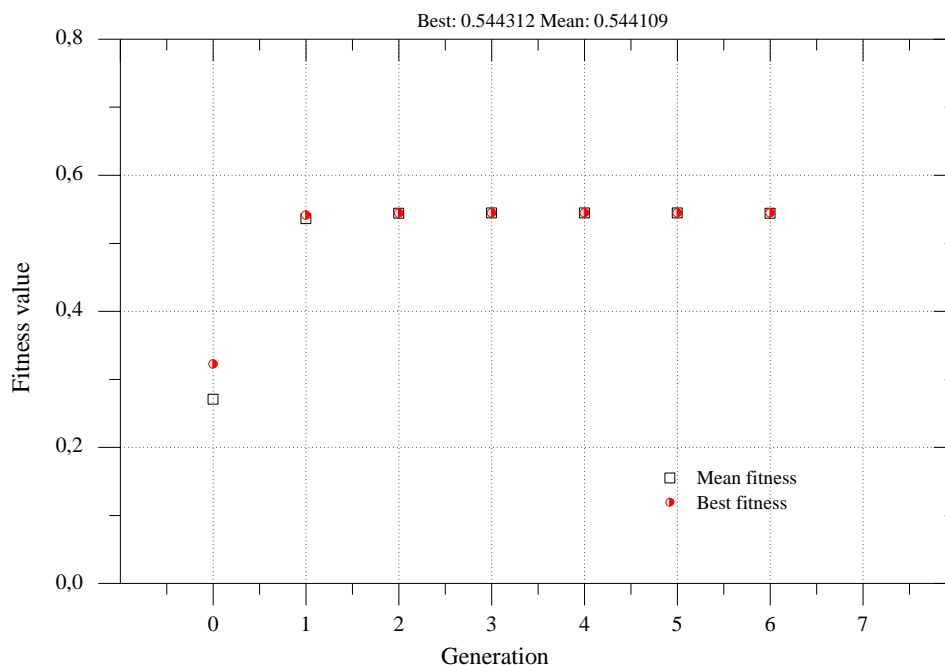


Fig. 6.6. Maximum (Best) and mean Thermal efficiency for several generations of the winter optimization process.

Acting as a constraint function, the electrical efficiency reached a maximum close to 10%, as can be seen in Table 6.5.

Table 6.5. Electrical efficiency of the winter optimization process

Constraint	Generation						
	0	1	2	3	4	5	6
Max constraint	0.09985	0.09992	0.09993	0.09993	0.09993	0.09993	0.09993

This is a good result when compared with the maximum electrical efficiency stated by the manufacturer of 12.5% under standard test conditions. There was an improvement of 1.6%. As already mentioned, this photovoltaic module is installed vertically on the south-facing facade.

The half black dots in Fig. 6.7 denote the maximum constraint values in each generation. The plot also displays the maximum constraint value in the current generation, numerically at the top. As in the fitness value, the maximum constraint value improves rapidly in the early generations, when the individuals are further from the optimum. The maximum constraint value improves more slowly in later generations, whose populations are closer to the optimal point.

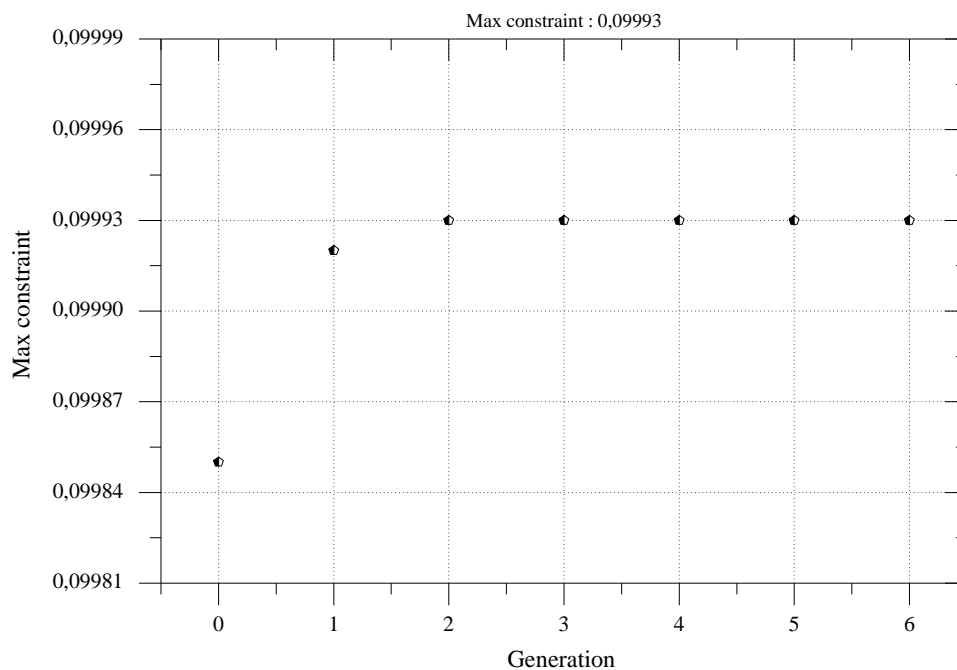


Fig. 6.7. Electrical efficiency from the winter optimization process

Fig. 6.8 shows the values of the variables (Table 6.2) obtained from the winter optimization process. It was with these values of the variables that the optimization process achieved the values shown in Fig. 6.6 and in Fig. 6.7.

The values of the variables of the optimization process for the winter season suggest forced ventilation during day, with an air velocity equal to 9.0835 m/s (Table 6.6). This velocity in conjunction with increased air cavity thickness (0.0865 m) increases the mass flow rate and the energy transfer to the interior room, simultaneously cooling down the photovoltaic module.

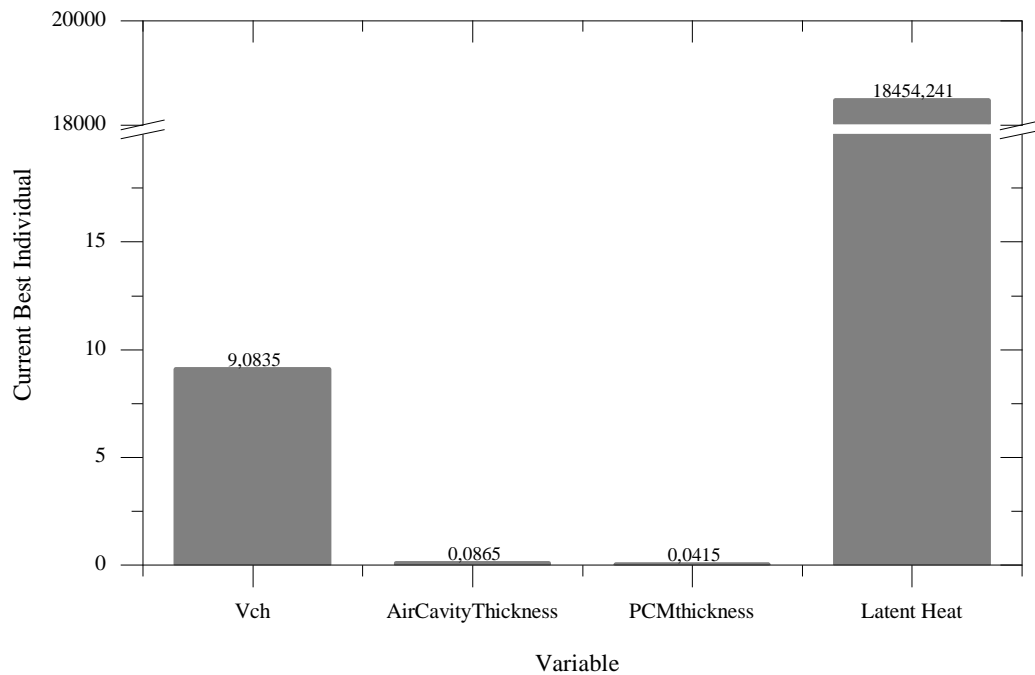


Fig. 6.8. Optimization variables: winter optimization process results

The thickness of 0.0415 m creates a greater resistance to heat transfer by conduction, minimizing loss during the night when the ventilation is turned off and the vents are closed. According to the optimization process, the phase change material should have a release and absorption of energy in the form of latent heat equal to 18454.241 J/kg. This phenomenon will regulate and smooth the temperature peak of the material.

Table 6.6. Optimization variables: winter optimization process results

Variable	Value	Units
Ventilation	9.0835	m/s
Air Gap	0.0865	m
Latent Heat	18454.241	J/kg
PCM Thickness	0.0415	m

As can be seen in Fig. 6.9, the maximum temperature reached by the photovoltaic module is 45 °C, 15 °C less than that shown in Fig. 5.17. It is the highest temperature suggested by the manufacturer for the proper functioning of the module.

The figure makes it clear that PCM gypsum board has a more “stable” configuration, as expected, with the surface facing the room maintaining a temperature of about 28°C during the day and 15°C at night.

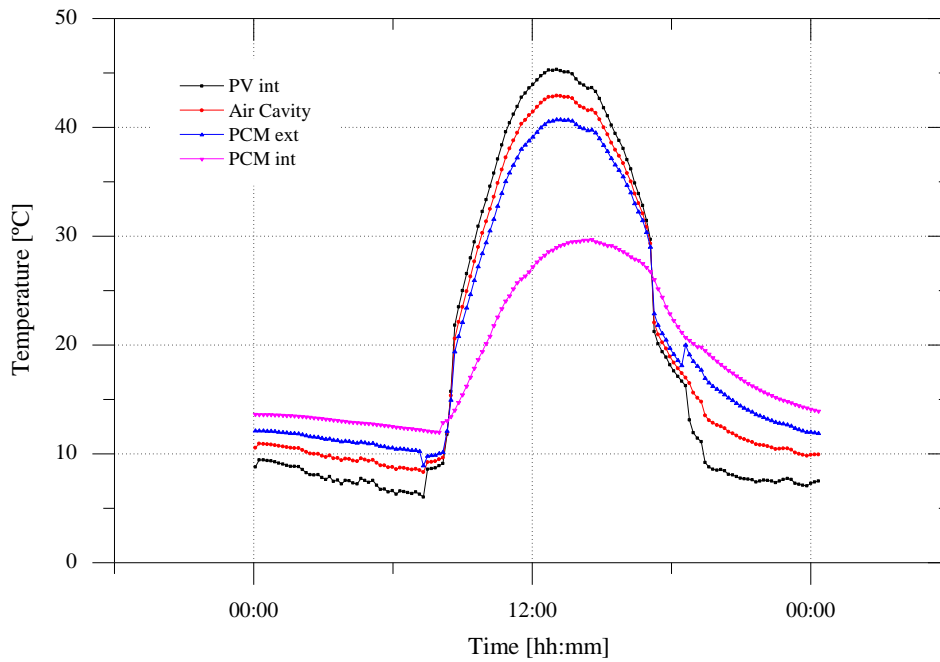


Fig. 6.9. System temperatures obtained from the optimization process

6.5.2. Summer

In the summer configuration, the optimization process achieved a thermal efficiency of 26.8%, as shown in Table 6.7. This is the result of the objective defined in the Fitness Function for the summer configuration (Fig. 6.4).

Table 6.7. Thermal efficiency of the summer optimization process

Fitness Value	Generation						
	0	1	2	3	4	5	6
Mean Fitness	0.2081	0.2615	0.2651	0.2668	0.2652	0.267	0.2675
Best Fitness	0.2566	0.2671	0.2672	0.2672	0.2676	0.2679	0.2682

The half red dots in Fig. 6.10 again denote the best fitness values, while squares denote the averages of the fitness values in each generation. The plot also displays the best and mean values in the current generation, numerically at the top.

The average fitness is simply the mean of the fitness values across the entire population. The population changes in each generation and a new average population fitness is obtained. Generally, the most interest is in the best fitness, as only one solution is needed and the best one will obviously be chosen. Average fitness, however, is useful for showing what the algorithm is doing. If the average fitness reaches the best fitness, it probably means that the population contains N copies of the best individual and any further search is likely to be wasted effort without a restart or large-scale mutation operation. So, what is generally seen is that best fitness tends to

get better over time, quickly at first and then slowing down as the algorithm finds better and better solutions that are harder and harder to improve upon. The average fitness will never be better than the best fitness, and it is typically quite a bit worse, with the difference between the two usually decreasing over time until the algorithm completely converges (Fig. 6.10).

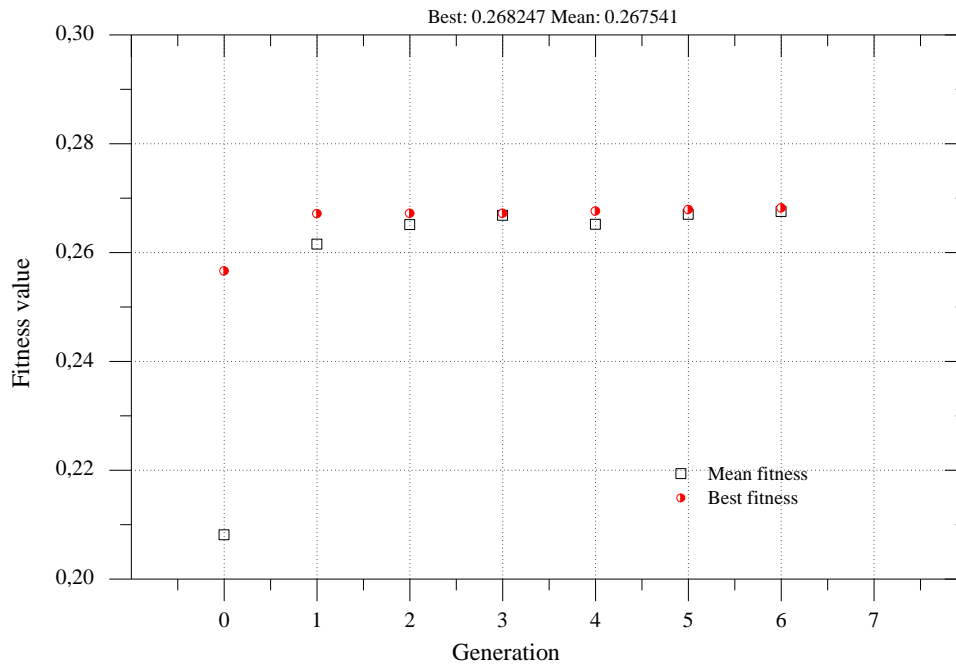


Fig. 6.10. Maximum (Best) and mean Thermal efficiency for several generations of the summer optimization process.

As in the winter configuration, the electrical efficiency acts as a constraint function and reached a maximum close to 5%, as can be seen in Table 6.8. The result obtained is not the most favourable when compared with the value provided by the manufacturer (12.5%). However, it is easily explained by the position of the sun relative to the vertical facade (where the system is installed) in the summer. Compared with the electrical efficiency obtained before optimization, the system has improved 0.8%.

Table 6.8. Electrical efficiency of the summer optimization process

Constraint	Generation						
	0	1	2	3	4	5	6
Max constraint	0.04992	0.04993	0.04994	0.04994	0.04994	0.04994	0.04994

The half black dots in Fig. 6.11 denote the maximum constraint values in each generation. After the 3rd generation the system stabilized at the final value (4.994%).

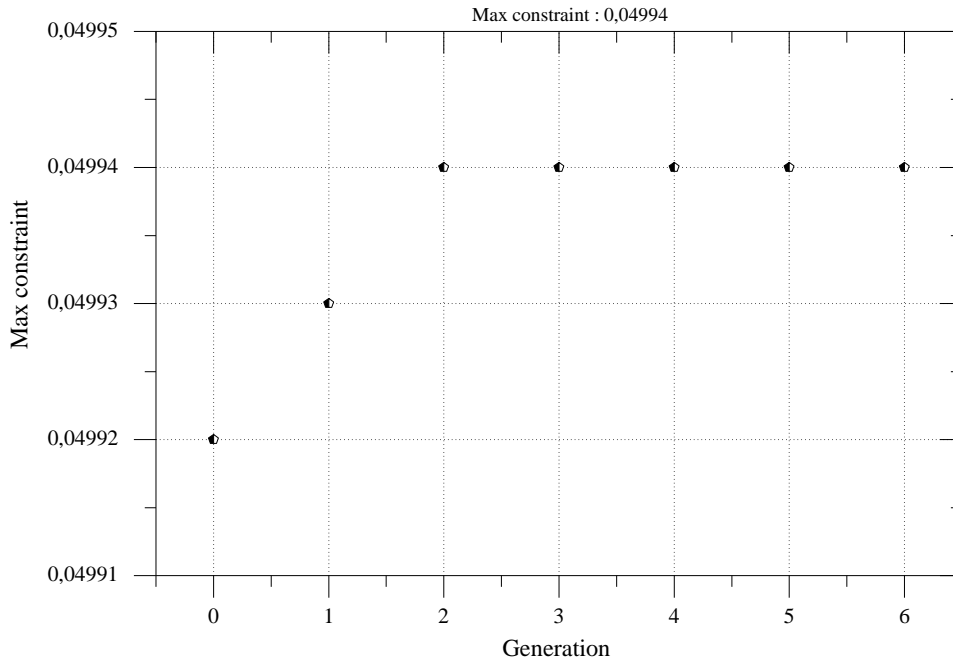


Fig. 6.11. Electrical efficiency of the summer optimization process

Fig. 6.12 shows the values of the variables (Table 6.2) obtained from the summer optimization process.

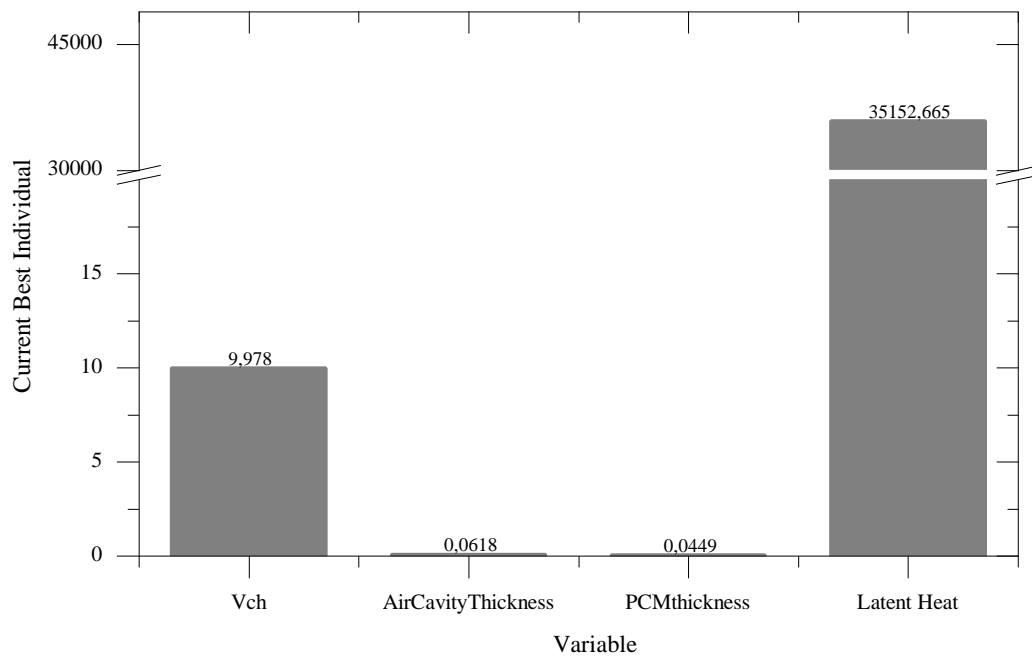


Fig. 6.12. Optimization variables: summer optimization process results

As expected, the optimization results (Table 6.9) indicate strong ventilation (9.978 m/s) and air cavity thickness of 6 cm, for the purpose of cooling the panel during the day. In order to minimize the energy exchange between the exterior and the interior, the optimization process has increased the thickness of the gypsum board (4.49 cm). Increasing the variable "latent heat" (35150.576 J/kg) allows better regulation of the heat transfer between layers.

Table 6.9. Optimization variables: results from summer optimization process results

Variable	Value	Units
Ventilation	9.978	m/s
Air Gap	0.0618	m
Latent Heat	35152.665	J/kg
PCM Thickness	0.0449	m

As can be seen in Fig. 6.13, the maximum temperature reached by the photovoltaic module is 46 °C, 10 °C less than that shown in Fig. 5.21.

“PCM int” has substantially lower temperatures than “PCM ext”, reinforcing the idea of the resistance that gypsum board offers to the energy exchange between exterior and interior. The effect of temperature peak regulation by the latent heat phenomenon is clearly visible in the “stable” temperature profile presented by the “PCM int” curve.

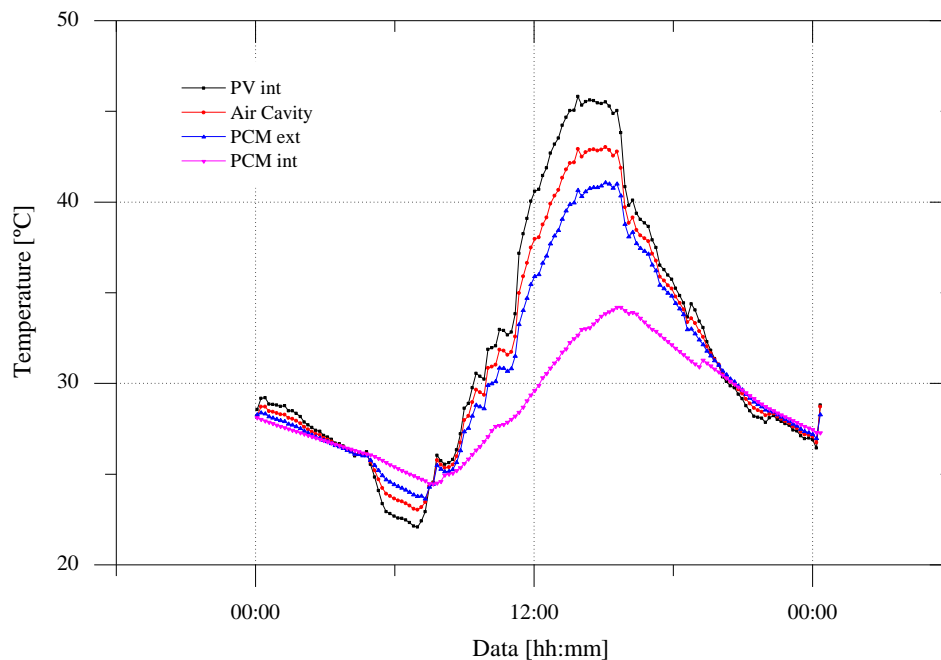


Fig. 6.13. System temperatures obtained from the optimization process

6.5.3. Overall

After presenting the results of the optimization process for the winter and summer configurations, they can be summarized so as to make a direct comparison.

Regarding the winter configuration, Fig. 6.14 shows that an optimization of the system of about 40% was possible, shifting overall efficiency from 24% to 64%. As expected, the largest increase is related to thermal efficiency (16-54%), however the increase of electrical efficiency (8.4 – 9.9%) is also significant for this type of system.

In the summer configuration, the optimization managed to change the thermal efficiency from a negative to a positive value, which caused total efficiency to increase to 36%. As mentioned previously, the electrical efficiency failed to achieve a significant increase (0.07%) due to the vertical positioning of the PV module.

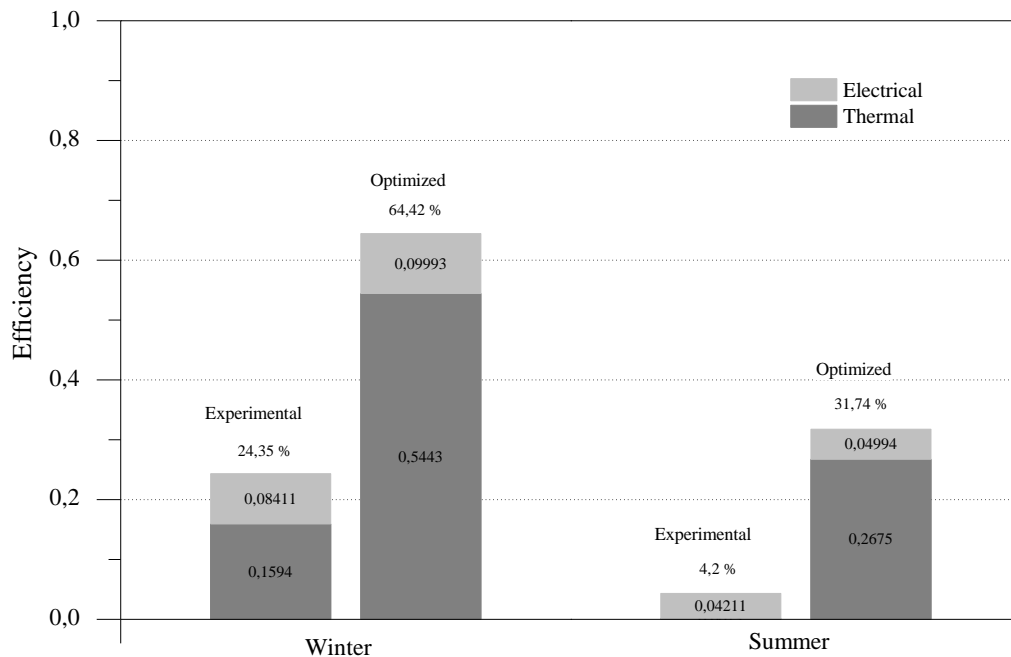


Fig. 6.14. Total efficiency analysis

Fig. 6.15 gives the values of the variables resulting from the experimental evaluation and from the winter and summer optimization processes.

It is evident in both optimization processes that the ventilation in the experimental facility is quite poor. Looking at the values of the air velocity and the cavity thickness obtained from the optimization, it can be concluded that a greater flow is required for a higher energy transfer (inwards or outwards) and cooling of the photovoltaic module.

The values obtained for the variable relating to the PCM thickness, suggest the need to create some resistance to heat propagation. Decreasing the thermal conductivity constant or applying

some type of insulation may be the solution to achieve the desired effect. However, increasing the storage and release capacity of the PCM, as suggested by the results of the variable relating to the latent heat (18454 – 35152 J/kg), may be the path to take. The optimization process unequivocally shows the influence of the PCM on controlling the temperature peaks (Fig. 6.9 and Fig. 6.13).

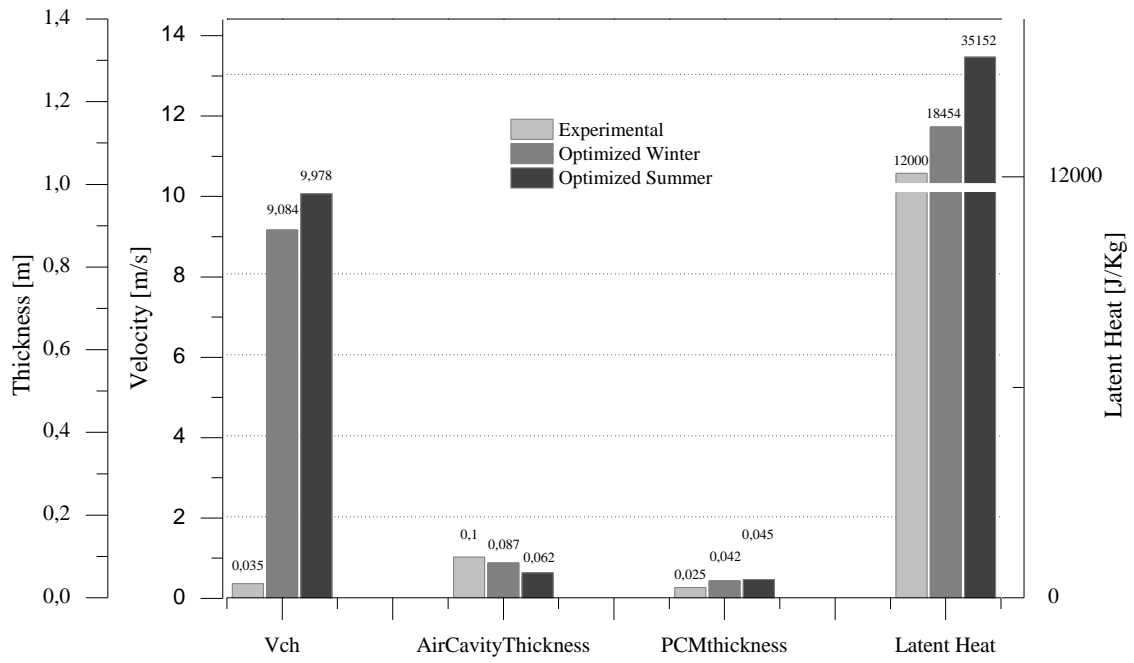


Fig. 6.15. Variables analysis

Chapter 7. CONCLUSION

7.1. DISCUSSION

This work has studied the thermal and electrical behavior of a building integrated PV/T system analytically, numerically and experimentally. This system integrates the material phase change in its configuration, and its thermal behavior was analyzed by the same means. In order to improve the system efficiency, an optimization was performed using the genetic algorithm method.

Some brief conclusions about the methods used and results obtained are now presented, as well as some possible future developments.

Regarding the numerical model, a model was specifically designed to calculate the temperature distribution, heat fluxes and flow rates in the cavity; it was flexible enough to accommodate different system configurations.

The numerical model developed is two-dimensional, allowing the system dependent variables, specifically the temperatures and heat fluxes, to be calculated. Natural or mechanically ventilated systems can be simulated in this model, with different ventilation modes, multi-layer compositions

and a host of air cavity geometries. This numerical program comprises a heat transfer model that includes the conduction, convection and radiation phenomena.

Another important part of the numerical work focused on modeling the phase change material, since this has some specific characteristics that distinguish it from other elements, particularly in relation to physical properties.

The numerical model was validated against the experimental results of the present work.

Regarding the experimental evaluation, the system was studied in a real environment to gain information on its thermal behavior and to validate the numerical model.

This analysis was conducted in two different seasons for days with a quite distinct radiation profile. It was clear that for all the situations evaluated (heating and cooling), the ventilation inside the air cavity was defective (construction issues). The use of a PCM proved to be a good option, however, resulting in good indicators regarding its thermal performance. Despite the low percentage of PCM in the gypsum board, it was possible to see how this type of material can regulate the temperature and heat fluxes. The stratification of the air temperature can clearly be seen within the air cavity, prefiguring a reduction of thermal consumption in the room in the event of forced ventilation.

This analysis also showed that there is a close relationship between the temperature distribution in the system and the solar radiation during the day, and the outside air temperature at night. In this regard, it was found that the maximum temperatures were reached in the winter because higher values of solar radiation on a vertical plane were recorded in this season.

The numerical and experimental components of the work were conducted almost simultaneously, allowing their results to be compared. In the first place, this made it possible to test the functionality of the numerical model, and second, it helped to understand some experimental data. In terms of temperatures and heat fluxes, comparisons between the numerical and experimental values showed a quite satisfactory agreement.

Once the numerical model had been validated, to complete the work, an optimization of the system was conducted using the genetic algorithm method. The optimization aimed to increase the efficiency of the system for two different configurations, winter and summer. The variables were the thickness of air cavity, the air flow velocity within cavity, the PCM latent heat and the thickness of the gypsum board. It was found that, with some changes in the variables analyzed, the system can improve to give higher efficiencies.

7.2. FUTURE WORK

The experimental evaluation of this work was performed in a real environment subject to the relevant physical phenomena. For this reason, the numerical model can simulate only to a certain degree of uncertainty. To avoid making various assumptions to minimize this uncertainty, it is recommended to install the prototype in a controlled environment and thus reduce the influence of sporadic phenomena, like gusts of wind, on the system. The numerical model of the PCM adopted an approach that seemed interesting to the author. It would be interesting to compare the results of simulations when a different approach had been taken to modelling the PCM.

The thermal analysis carried out in this work demonstrates the importance of ventilation inside the cavity. Fans could be used in a future construction to provide forced ventilation, adjustable to the cavity.

The analysis has also shown that it is important to highlight the quality and the percentage of the PCM in gypsum board. A new type of PCM could be considered for a new system. It should have a higher capacity for energy storage and a working temperature appropriate to the PV module's operating temperature.

The result of the optimization suggests that the increased thickness of the PCM may indicate a need for heat transfer resistance, which may involve the use of some type of insulation.

REFERENCES

- [1] Parliament E, Union C of the E. Directive 2002/91/EC of the European Parliament and of the Council. 2003.
- [2] Commission Of The European Communities. Proposal For A Directive Of The European Parliament And Of The Council On The Energy Performance Of Buildings. 2001.
- [3] European Commission. Directive 2010/31/EU of the European Parliament and of the Council of 19 May 2010 on the energy performance of buildings. Official Journal of the European Union; 2010.
- [4] Bouzoukas A. New Approaches for Cooling Photovoltaic/Thermal (PV/T) Systems. University of Nottingham, 2008.
- [5] Petter Jelle B, Breivik C, Drolsum Røkenes H. Building integrated photovoltaic products: A state-of-the-art review and future research opportunities. Sol Energy Mater Sol Cells 2012;100:69–96.
- [6] Candanedo L, Athienitis AK, O'Brien L, Candanedo J. Transient and Steady State Models for Open-Loop Air-Based BIPV/T Systems. Orlando: 2010.

- [7] NREL. Design Brief -Building Integrated Photovoltaics n.d.:29.
- [8] Report T. 41.A.2: IEA - SHC Task 41 Solar energy and Architecture. Solar Energy Systems in Architecture - Integration Criteria and Guidelines. 2012.
- [9] Krauter S, Araújo RG, Schroer S, Hanitsch R, Salhi MJ, Triebel C, et al. Combined photovoltaic and solar thermal systems for facade integration and building insulation. *Sol Energy* 1999;67:239–48.
- [10] Chow TT, He W, Ji J. An experimental study of façade-integrated photovoltaic/water-heating system. *Appl Therm Eng* 2007;27:37–45.
- [11] Chow TT, He W, Chan ALS, Fong KF, Lin Z, Ji J. Computer modeling and experimental validation of a building-integrated photovoltaic and water heating system. *Appl Therm Eng* 2008;28:1356–64.
- [12] Chow TT, Chan ALS, Fong KF, Lin Z, He W, Ji J. Annual performance of building-integrated photovoltaic/water-heating system for warm climate application. *Appl Energy* 2009;86:689–96.
- [13] Chow TT, Hand JW, Strachan PA. Building-integrated photovoltaic and thermal applications in a subtropical hotel building. *Appl Therm Eng* 2003;23:2035–49.
- [14] Chow TT. A review on photovoltaic/thermal hybrid solar technology. *Appl Energy* 2010;87:365–79.
- [15] Jie J, Chow T-T, He W. Dynamic performance of hybrid photovoltaic/thermal collector wall in Hong Kong. *Build Environ* 2003;38:1327–34.
- [16] Ji J, Han J, Chow T, Yi H, Lu J, He W, et al. Effect of fluid flow and packing factor on energy performance of a wall-mounted hybrid photovoltaic/water-heating collector system. *Energy Build* 2006;38:1380–7.
- [17] Ghani F, Duke M, Carson JK. Effect of flow distribution on the photovoltaic performance of a building integrated photovoltaic/thermal (BIPV/T) collector. *Sol Energy* 2012;86:1518–30.
- [18] Ghani F, Duke M, Carson JK. Estimation of photovoltaic conversion efficiency of a building integrated photovoltaic/thermal (BIPV/T) collector array using an artificial neural network. *Sol Energy* 2012;86:3378–87.
- [19] Ibrahim A, Fudholi A, Sopian K, Othman MY, Ruslan MH. Efficiencies and improvement potential of building integrated photovoltaic thermal (BIPVT) system. *Energy Convers Manag* 2014;77:527–34.
- [20] Jie J, Hua Y, Gang P, Jianping L. Study of PV-Trombe wall installed in a fenestrated room with heat storage. *Appl Therm Eng* 2007;27:1507–15.

-
- [21] Jie J, Hua Y, Wei H, Gang P, Jianping L, Bin J. Modeling of a novel Trombe wall with PV cells. *Build Environ* 2007;42:1544–52.
- [22] Jie J, Hua Y, Gang P, Bin J, Wei H. Study of PV-Trombe wall assisted with DC fan. *Build Environ* 2007;42:3529–39.
- [23] Koyunbaba BK, Yilmaz Z, Ulgen K. An approach for energy modeling of a building integrated photovoltaic (BIPV) Trombe wall system. *Energy Build* 2013;67:680–8.
- [24] Infield D, Mei L, Eicker U. Thermal Performance Estimation for Ventilated PV Facades. *Sol Energy* 2004;76:93–8.
- [25] Dehra H. A two dimensional thermal network model for a photovoltaic solar wall. *Sol Energy* 2009;83:1933–42.
- [26] Muresan C, Ménézo C, Bennacer R, Vaillon R. Numerical Simulation of a Vertical Solar Collector Integrated in a Building Frame: Radiation and Turbulent Natural Convection Coupling. *Heat Transf Eng* 2006;27:29–42.
- [27] Kim J-H, Kim J-T. A Simulation Study of Air-Type Building-Integrated Photovoltaic-Thermal System. *Energy Procedia* 2012;30:1016–24.
- [28] Lin Y, Chiang C, Lai C. Energy Efficiency and Ventilation Performance of Ventilated BIPV Walls. *Eng Appl Comput Fluid Mech* 2011;5:479–86.
- [29] Ho CJ, Tanuwijava AO, Lai C-M. Thermal and electrical performance of a BIPV integrated with a microencapsulated phase change material layer. *Energy Build* 2012;50:331–8.
- [30] Gonçalves H, Cabrita C. Solar XXI - Towards zero energy - So. LNEG - Laboratório Nacional de Enrgia E Geologia: LNEG; 2010.
- [31] Athienitis AK, Bambara J, O'Neill B, Faille J. A prototype photovoltaic/thermal system integrated with transpired collector. *Sol Energy* 2011;85:139–53.
- [32] Shukla A, Nkwetta DN, Cho YJ, Stevenson V, Jones P. A state of art review on the performance of transpired solar collector. *Renew Sustain Energy Rev* 2012;16:3975–85.
- [33] Athienitis AK, Zhang J. A Study of Double Facades with Phase-Change Storage and Photovoltaics. *Int. Conf. "Passive Low Cool. Built Environ., Department of Buildind, Civil and Environmental Engineering of Concordia University: 2005, p. 855–9.*
- [34] Aelenei L, Pereira R. Innovative solutions for net zero-energy building: BIPV-PCM system - Modeling, design and thermal performance. 2013 4th Int. Youth Conf. Energy, IEEE; 2013, p. 1–6.
- [35] Aelenei L, Pereira R, Gonçalves H, Silva AR e. Energy saving potential of a hybrid BIPV-T system integrated with heat storage material. In: McCormack SJ, Severino I, Browne M,

- editors. 2nd Int. Energy Storage Conf. 2013, Dublin: 2013, p. 12–6.
- [36] Aelenei L, Pereira R, Gonçalves H. BIPV-T versus BIPV-PCM: A numerical investigation of advanced system integrated into SolarXXI building façade. In: McCormack SJ, Severino I, Browne M, editors. 2nd Int. Energy Storage Conf. 2013, Dublin: 2013, p. 7–11.
- [37] Aelenei L, Pereira R, Gonçalves H, Athienitis A. Thermal Performance of a Hybrid BIPV-PCM: Modeling, Design and Experimental Investigation. *Energy Procedia* 2014;48:474–83.
- [38] Wang Y, Tian W, Ren J, Zhu L, Wang Q. Influence of a building's integrated-photovoltaics on heating and cooling loads. *Appl Energy* 2006;83:989–1003.
- [39] Anderson TN, Duke M, Morrison GL, Carson JK. Performance of a building integrated photovoltaic/thermal (BIPVT) solar collector. *Sol Energy* 2009;83:445–55.
- [40] Agrawal B, Tiwari GN. Optimizing the energy and exergy of building integrated photovoltaic thermal (BIPVT) systems under cold climatic conditions. *Appl Energy* 2009;87:417–26.
- [41] Agrawal B, Tiwari GN. Life cycle cost assessment of building integrated photovoltaic thermal (BIPVT) systems. *Energy Build* 2010;42:1472–81.
- [42] Corbin CD, Zhai ZJ. Experimental and numerical investigation on thermal and electrical performance of a building integrated photovoltaic–thermal collector system. *Energy Build* 2010;42:76–82.
- [43] Chen Y, Galal K, Athienitis AK. Modeling, design and thermal performance of a BIPV/T system thermally coupled with a ventilated concrete slab in a low energy solar house: Part 2, ventilated concrete slab. *Sol Energy* 2010;84:1908–19.
- [44] Pantic S, Candanedo L, Athienitis AK. Modeling of energy performance of a house with three configurations of building-integrated photovoltaic/thermal systems. *Energy Build* 2010;42:1779–89.
- [45] Shahsavar A, Salmanzadeh M, Ameri M, Talebizadeh P. Energy saving in buildings by using the exhaust and ventilation air for cooling of photovoltaic panels. *Energy Build* 2011;43:2219–26.
- [46] Wang J, Conejo AJ, Wang C, Yan J, Vats K, Tiwari GN. Energy and exergy analysis of a building integrated semitransparent photovoltaic thermal (BISPVT) system. *Appl Energy* 2012;96:409–16.
- [47] Vats K, Tomar V, Tiwari GN. Effect of packing factor on the performance of a building integrated semitransparent photovoltaic thermal (BISPVT) system with air duct. *Energy*

- Build 2012;53:159–65.
- [48] Vats K, Tiwari GN. Performance evaluation of a building integrated semitransparent photovoltaic thermal system for roof and façade. *Energy Build* 2012;45:211–8.
- [49] Yin HM, Yang DJ, Kelly G, Garant J. Design and performance of a novel building integrated PV/thermal system for energy efficiency of buildings. *Sol Energy* 2013;87:184–95.
- [50] Bosanac M, Sørensen B, Katic I, Sørensen H, Nielsen B, Badran J. *Photovoltaic/Thermal Solar Collectors and Their Potential in Denmark*. 2003.
- [51] Kalogirou SA. Use of TRNSYS for modelling and simulation of a hybrid pv–thermal solar system for Cyprus. *Renew Energy* 2001;23:247–60.
- [52] Thevenard D. Review and recommendations for improving the modelling of building integrated photovoltaic systems. Ninth Int. IBPSA Conf., Montréal: 2005, p. 1221–8.
- [53] Aelenei L. *Thermal Performance of Naturally Ventilated Cavity Walls*. Universidade Técnica de Lisboa - Instituto Superior Técnico, 2005.
- [54] Özisik MN. *HEAT TRANSFER - A Basic Approach*. McGraw-Hill; 1985.
- [55] Incropera FP, DeWitt DP. *Fundamentals of Heat and Mass Transfer*. 5th ed. John Wiley & Sons; 2002.
- [56] Duffie JA, Beckman WA. *Solar Engineering of Thermal Processes*. 4th ed. John Wiley & Sons, Inc; 2013.
- [57] Gomes M. *Comportamento Térmico De Fachadas De Dupla Pele*. IST, 2010.
- [58] Sharma A, Tyagi VV, Chen CR, Buddhi D. Review on thermal energy storage with phase change materials and applications. *Renew Sustain Energy Rev* 2009;13:318–45.
- [59] Trombe F, Sesolis B, Robert JF, Cabanot M. Concrete walls to collect and hold heat. *Sol Age* 1977;2.
- [60] Utzinger DM. *Analysis of Building Components Related to Direct Solar Heating of Buildings*. 1979.
- [61] Nkwetta DN, Haghghat F. Thermal energy storage with phase change material—A state-of-the art review. *Sustain Cities Soc* 2013.
- [62] AL-Saadi SN, Zhai Z (John). Modeling phase change materials embedded in building enclosure: A review. *Renew Sustain Energy Rev* 2013;21:659–73.
- [63] Athienitis AK, Liu C, Hawes D, Banu D, Feldman D. Investigation of the thermal performance of a passive solar test-room with wall latent heat storage. *Build Environ* 1997;32:405–10.

- [64] Özişik MN, Uzzell JC. Exact Solution for Freezing in Cylindrical Symmetry with Extended Freezing Temperature Range. *J Heat Transfer* 1979;101:331.
- [65] Candanedo LM, Athienitis AK, Candanedo J, O'Brien W, Chen YX. A Simplified Model For Open Loop Air_Based BIPVT/T Systems 2009:1–12.
- [66] Test FL, Lessmann RC, Johary A. Heat Transfer During Wind Flow over Rectangular Bodies in the Natural Environment. *J Heat Transfer* 1981;103:262.
- [67] Kalogirou SA. *Solar Energy Engineering - Processes and Systems*. 1st ed. London: Elsevier; 2009.
- [68] Shewen E, Hollands KGT, Raithby GD. Heat Transfer by Natural Convection Across a Vertical Air Cavity of Large Aspect Ratio. *J Heat Transfer* 1996;118:993.
- [69] Hollands KGT, Unny TE, Raithby GD, Konicek L. Free Convective Heat Transfer Across Inclined Air Layers. *J Heat Transfer* 1976;98:189.
- [70] Candanedo LM, Athienitis A. Convective Heat Transfer Coefficients in a Building-Integrated Photovoltaic/Thermal System. *J Sol Energy Eng* 2011;133:1–15.
- [71] Santos CAP dos, Matias LMC. *Coeficientes de Transmissão Térmica De Elementos da Envolvente do Edifícios*. 1st ed. Lisboa: LNEC; 2006.
- [72] Sahoo NC, Elamvazuthi I, Nor NM, Sebastian P, Ping LB. PV Panel Modelling using Simscape 2011:1–4.
- [73] Pereira RJ, Melício R, Mendes VMF, Joyce A. PV System with Maximum Power Point Tracking : Modeling , Simulation and Experimental Results. *Procedia Technol* 2014;00.
- [74] Mathworks. *Simulink User's Guide R2014a* 2014:89.
- [75] Mathworks. *Simscape User's Guide R2013b* 2013:245.
- [76] Technologies A. *Agilent 34970A Data Acquisition / Switch Unit Family* 2012:28.
- [77] Holland JH. *Adaptation in Natural and Artificial Systems*. 1st ed. Ann Arbor, MI, USA: University of Michigan Press; 1975.
- [78] Goldberg DE. *Genetic Algorithms in Search , Optimization , and Machine Learning*. 1st ed. Boston: Addison-Wesley Publishing Company, Inc.; 1989.
- [79] Ávila S. *Algoritmos Genéticos Aplicados na Otimização de Antenas Refletores*. Universidade Federal de Santa Catarina, 2002.
- [80] Haupt RL, Haupt SE. Optimum population size and mutation rate for a simple real genetic algorithm that optimizes array factors. *IEEE Antennas Propag. Soc. Int. Symp.*, vol. 2, IEEE; 2000, p. 1034–7 vol.2.
- [81] Mathworks. *Optimization Toolbox™ User's Guide R2014a* 2014:849.

APPENDICES

APPENDIX A

MATLAB model – Objective Function

```
% Objective Function
function obj = objective_fun(vecx)

Vch=vecx(1)           % Channel air speed, range: [0.035, 10]
aircavity_thickness=vecx(2) % Air gap thickness, range: [2,10]
pcm_thickness=vecx(3) % PCM thickness, range: [0.025, 0.05]
Latentheat=vecx(4)   % PCM latent heat, range: [12000,50000]

%-----
% Run FRAME_MODEL (define all variables and constants, weather file, time step, material %
properties):

FRAME_MODEL

% End FRAME_MODEL
%-----

%-----
% Simulink Variable entry's (Numerical approach computation):

Set_Parameters_model

% END Simulink Variable entrys:
%-----

% Run thermal model of Frame system
simOut = sim('FRAME_Simscape_MODEL','SaveOutput','on','OutputSaveName','Eff');
% Extract efficiency results
Array = get(simOut,'Eff');
% Extract efficiency results in a array
Efficiency = Array(:,1);
% Set an onjective to the function
System_Efficiency = min(Efficiency(:,1))
obj = System_Efficiency;

end
```

APPENDIX B

MATLAB model – Restriction Function

```
% Restriction Function
function [c,ceq] = restrition_fun(vecx)

Vch=vecx(1)           % Channel air speed, range: [0.035, 10]
aircavity_thickness=vecx(2) % Air gap thickness, range: [2,10]
pcm_thickness=vecx(3) % PCM thickness, range: [0.025, 0.05]
Latentheat=vecx(4)   % PCM latent heat, range: [12000,50000]

%-----
% Run FRAME_MODEL (again)

FRAME_MODEL

% End FRAME_MODEL
%-----

%-----
%Simulink Variable entry's (Numerical approach computation)(again):
```

```

Set_Parameters_model

% END Simulink Variable entries:
%-----

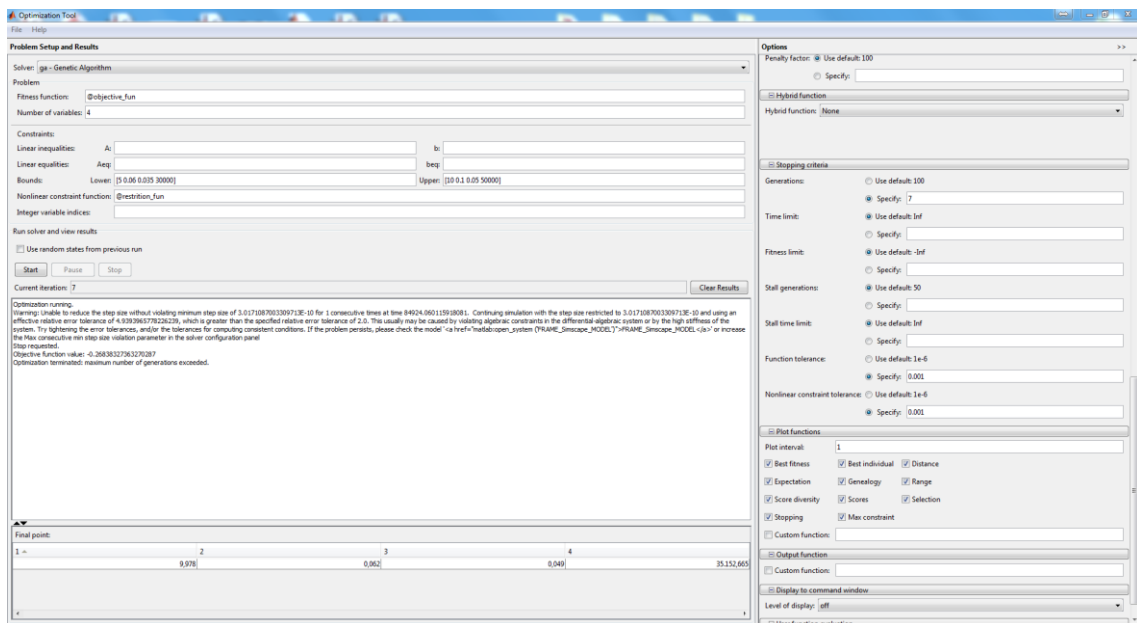
% Set maximum efficiency announced by manufacturer
Max_Eff_Manufact=12.5;

% Run thermal model of Frame system
simOut = sim('FRAME_Simscape_MODEL','SaveOutput','on','OutputSaveName','Eff_Elect');
% Extract efficiency results
Array_elect = get(simOut,'Eff_Elect');
% Extract efficiency results in a array
Eff_PV = Array_elect(:,2);
% Find maximum efficiency
Max_Eff_PV = max(Eff_PV(:,1))
% Set an objective to the function. Ceq must be equal to zero.
c=[];
ceq = Max_Eff_Manufact-Max_Eff_PV

end
    
```

APPENDIX C

Matlab optimization toolbox interface:



APPENDIX D



Hukseflux Thermal Sensors B.V.
 URL: www.hukseflux.com
 E-mail: info@hukseflux.com
 The Netherlands

Certificate of calibration

Type: HFP01-05
 Serial number: 7770

Calibration date: 06-11-2012
 Cable length: 05 m
 Sensitivity: 62.71 $\mu\text{V}/(\text{Wm}^{-2})$
 Remarks:
 Performed by: F. Warffemius

Connections:

Cable	Wire	
1	White	Signal [+]
1	Green	Signal [-]
1	Black	Shield

Traceability of calibration is to the "guarded hot plate" of National Physical Laboratory (NPL) of the UK. Applicable standards are ISO 8302 (EN 12664:2001) and ASTM C177.



Hukseflux Thermal Sensors B.V.
URL: www.hukseflux.com
E-mail: info@hukseflux.com
The Netherlands

Certificate of calibration

Type: HFP01-05
Serial number: 7768

Calibration date: 06-11-2012
Cable length: 05 m
Sensitivity: 62.18 $\mu\text{V}/(\text{Wm}^{-2})$
Remarks:
Performed by: F. Warffemius

Connections:

Cable	Wire	
1	White	Signal [+]
1	Green	Signal [-]
1	Black	Shield

Traceability of calibration is to the "guarded hot plate" of National Physical Laboratory (NPL) of the UK. Applicable standards are ISO 8302 (EN 12664:2001) and ASTM C177.



Hukseflux Thermal Sensors B.V.
 URL: www.hukseflux.com
 E-mail: info@hukseflux.com
 The Netherlands

Certificate of calibration

Type: HFP01-05
 Serial number: 7769

Calibration date: 06-11-2012
 Cable length: 05 m
 Sensitivity: 62.5 $\mu\text{V}/(\text{Wm}^{-2})$
 Remarks:
 Performed by: F. Warffemius

Connections:

Cable	Wire	
1	White	Signal [+]
1	Green	Signal [-]
1	Black	Shield

Traceability of calibration is to the "guarded hot plate" of National Physical Laboratory (NPL) of the UK. Applicable standards are ISO 8302 (EN 12664:2001) and ASTM C177.